DE TTK

1949

# Experimental Investigations of High Energy Particle Collisions at LEP and LHC

PhD thesis
Egyetemi doktori (PhD) értekezés

**Balázs Ujvári**

Supervisor / Témavezető:
Dr. Zoltán Trócsányi

University of Debrecen
PhD School in Physics

Debreceni Egyetem
Természettudományi Doktori Tanács
Fizika Tudományok Doktori Iskolája
Debrecen, 2012.

Ezen értekezést a Debreceni Egyetem Természettudományi Doktori Tanács Fizika Tudományok Doktori Iskolája Részecskefizika programja keretében készítettem a Debreceni Egyetem Természettudományi doktori (PhD) fokozatának elnyerése céljából.
Debrecen, 2012.

Ujvári Balázs

Tanúsítom, hogy Ujvári Balázs doktorjelölt 2000-2010 között a fent nevezett doktori iskola Részecskefizika programja keretében irányításommal végezte a munkáját. Az értekezésben foglalt eredményekhez a jelölt önálló alkotó tevékenységével meghatározóan hozzájárult.
Az értekezés elfogadását javaslom.
Debrecen, 2012.

Dr. Trócsányi Zoltán
témavezető

# Experimental Investigations of High Energy Particle Collisions at LEP and LHC

Értekezés a doktori (Ph.D.) fokozat megszerzése érdekében a fizika tudományágban

Írta: Ujvári Balázs okleveles fizikus

Készült a Debreceni Egyetem Fizika Tudományok Doktori Iskolája
Rśzecskefizika programja keretében

Témavezető: Dr. Trócsányi Zoltán

A doktori szigorlati bizottság:
elnök: Dr. .................................. ....................................
tagok: Dr. .................................. ....................................
Dr. .................................. ....................................

A doktori szigorlat időpontja: 20 . ............... ...

Az értekezés bírálói:
Dr. .................................. ....................................
Dr. .................................. ....................................

A bírálóbizottság:
elnök: Dr. .................................. ....................................
tagok: Dr. .................................. ....................................
Dr. .................................. ....................................
Dr. .................................. ....................................
Dr. .................................. ....................................

Az értekezés védésének időpontja: 20 . .............. ...

# Contents

# Chapter 1

# Introduction

## 1.1 The Standard Model

From the four fundamental forces: electromagnetism, weak, strong and gravity forces, the first three are combined in the frame of gauge theory. The Standard Model (SM) [1] is based on the gauge group $G = SU(3)_c \times SU(2)_L \times U(1)_Y$ [1] . The $SU(3)_c$ has gauge coupling $g_s$ and 8 gauge bosons (gluons) $G^i$, $i = 1 \ldots 8$. It is a non-chiral, and acts on the color indices of the L and R-chiral quarks $q_{r\alpha}$, where $\alpha = 1, 2, 3$ refers to color and $r$ to flavor. QCD itself is not spontaneously broken, gluons remain massless. The electroweak $SU(2)_L \times U(1)_Y$ factor is chiral. The $SU(2)_L$ group has gauge coupling $g$, gauge bosons they act only on flavor indices of the L-chiral fermions, $W^{\pm}$ lead to the charged current interaction and $W^0$ is a neutral boson. The abelian $U(1)$ factor has gauge coupling $g'$ and gauge bososn $B$. It is also chiral, acting on both L and R fermions but with different charges. After spontaneous sysmmetry breaking $SU(2)_L \times U(1)_Y$ is broken to a single unbroken $U(1)_Q$, incorporating QED with the massless photon, linear combination of $W^0$ and $B$. The orthogonal combination $Z$, as well as the $W^{\pm}$, acquire masses.

The fermion part of the Standar Model involves $F = 3$ families of quarks and leptons (Fig. 1.1). Each family consist of

$$\begin{aligned} \mathrm{L-doublets:} \quad & q^0_{mL} = \begin{pmatrix} u^0_m \\ d^0_m \end{pmatrix}_L, l^0_{mL} = \begin{pmatrix} \nu^0_m \\ e^{-0}_m \end{pmatrix}_L \\ \mathrm{R-singlets:} \quad & u^0_{mR}, d^0_{mR}, e^{-0}_{mR}, \nu^0_{mR}, \end{aligned} \tag{1.1}$$

---

[1] c refers to color, L to left-chiral nature and Y to the weak hypercharge quantum number

in which the L-chiral fields are $SU(2)_L$ doublets and the R fields are singlets. The superscript $^0$ refer to the fact that these fieleds are weak eigentstates. After spontaneous sysmmetry breaking these will become mixtures of mass eigenstates fields.

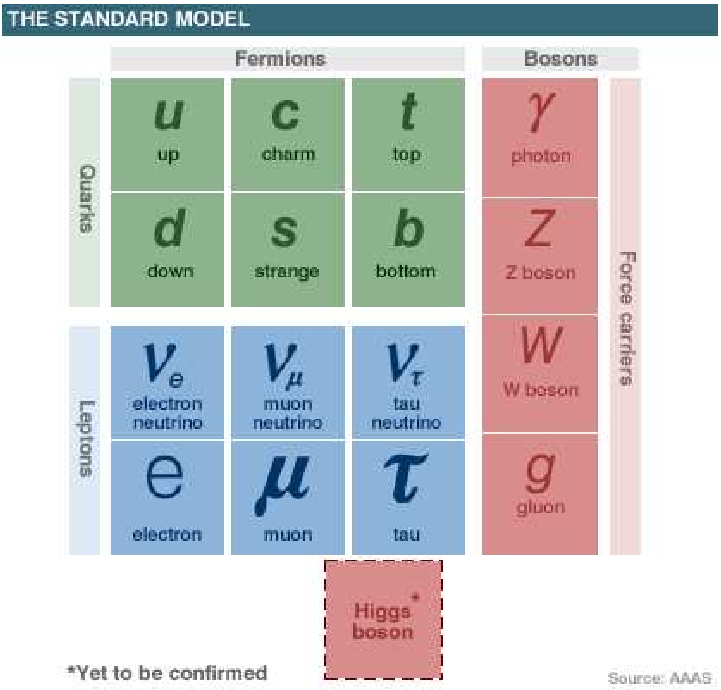

**Figure 1.1.** The fermions and bosons in the Standard Model

Anomalies may occur when the divergencies in a theory cannot be regularized in a way that is consistent with the original symmetries. The SM is anomaly free for the assumed fermion content, but not realistic, because bare mass terms are not allowed for the electroweak gauge bosons or for the fremions. However effective mass may be generated by spontaneous sysmmetry breaking, the Higgs doublet $\Phi$ was introduced for this purpose.

### 1.1.1 The Higgs Mechanism

The Higgs boson in a Hermetian basis:

$$\Phi = \begin{pmatrix} \Phi^+ \\ \Phi^0 \end{pmatrix} = \begin{pmatrix} \frac{1}{\sqrt{2}}(\Phi_1 + i\Phi_2) \\ \frac{1}{\sqrt{2}}(\Phi_3 + i\Phi_4) \end{pmatrix}, \tag{1.2}$$

the Higgs potential:

$$V(\Phi) = \frac{1}{2}\mu^2 \left( \sum_{i=1}^{4} \Phi_i^2 \right) + \frac{1}{4}\lambda \left( \sum_{i=1}^{4} \Phi_i^2 \right)^2 \tag{1.3}$$

consistent with the $SU(2)_L \times U(1)_Y$ gauge invariance. Without loss of generality we can choose the axis in this four-dimensional space, so that $\langle 0|\Phi_i|0\rangle = 0$ for $i = 1, 2, 4$ and $\langle 0|\Phi_3|0\rangle = 0$, we can quantize around the classical vacuum:

$$\Phi \to \Phi' = \frac{1}{2}\begin{pmatrix} 0 \\ v + H \end{pmatrix}, \tag{1.4}$$

where $H$ is a Hermitian scalar field, the Higgs boson, and the Higgs potential:

$$V(\Phi) \to V(v) = \frac{1}{2}\mu^2 v^2 + \frac{1}{4}\lambda v^4, \tag{1.5}$$

which must be minimized with respect to $v$. For $\mu^2 > 0$ the minimum occurs at $v = 0$ and $SU(2) \times U(1)$ is unbroken at the minimum. For $\mu^2 < 0$ the $v = 0$ symmetric point is unstable and the minimum occurs for $v \neq 0$ breaking the $SU(2)_L \times U(1)_Y$ symmetry to $U(1)_Q$, therefore photon (and the eight gluons) remain massless, while $W^\pm$ and $Z$ become massiv. In the $SU(2)_L \times U(1)_Y$ the fermion mass term was excluded by gauge invariance, the fermion term of the Lagrangian density consists entirely of gauge-covariant kinetic energy terms. There is a Yukawa coupling between the Higgs doublet and the fermions, which are needed to generate fermion masses by the spontaneous breaking of the chiral gauge symmetries. This is the most arbitrary aspect of the SM, the quark masses that appeared as bare masses in the QCD, in this model they are really spontaneous generated. The Higgs doublet has exactly the required $SU(2) \times SU(1)$ quantum numbers to couple to the fermion. The coupling is also arbitrary, the actual mass of the fermion is not predicted.

## 1.2 The Quantum Chromodynamics

The theory of the strong interactions is quantum chromodynamics (QCD), part of the Standard Model, governs the strong nuclear interactions. The basic ingredient is that each of the six flavours of quarks ($u, d, s, c, b$ and $t$) has an additional quantum number: *color*, which takes the value red (R), blue (B) and green (G), analogue to the primary colors. There is an unbroken non-chiral $SU(3)$ symmetry acting on these color index. There are 8 massless gauge bosons (*gluon*) and a strong gauge coupling $g_s$ and strong fine structure constant $\alpha_s = g_s^2/4\pi$.

## 1.3 Standard Model Test

Various aspects of the Standard Model including electroweak interaction, QCD, heavy flavour physics, the CKM matrix and CP violation were tested. This theory has been the focus of intense scrutiny by experimental physicists, most notably at high energy particle colliders (SLC, LEP, Tevatron, LHC), over the last three decades [2].

In the SM, the W and Z bosons mediate the weak force and acquire mass through the Higgs mechanism. The discovery of these gauge bosons at CERN represents a dramatic validation of Glashow-Salam-Weinberg [3] (GSW) theory which predicted the existence of neutral currents mediated by a new gauge boson, the Z boson, and predicted the W bosons to describe nuclear $\beta$-decay. Detailed measurement of the W and Z properties at the colliders is not only important to further test GSW theory and the electroweak symmetry breaking (EWSB) mechanism in the SM but also to search for new physics beyond the SM.

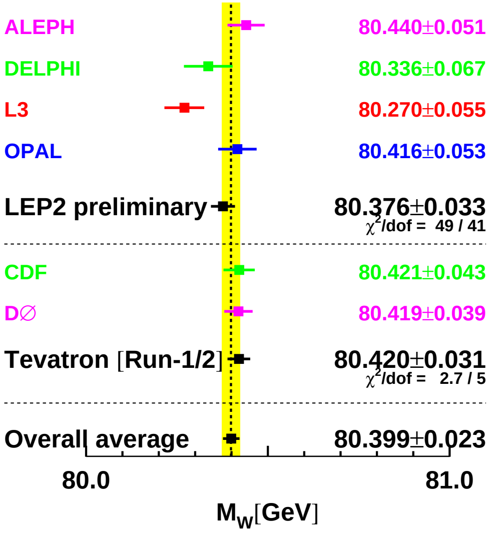

**Figure 1.2.** W-boson mass measurement at Tevatron and LEP [4].

One of the most important results from LEP is the measurement of the number of light neutrinos [5]:

$$N_\nu = 2.9841 \pm 0.0083, \tag{1.6}$$

about 1.9 standard deviations less than 3, the SM prediction.

After $\tau$-lepton was discovered the SM predicted that other members of the third family of quarks and leptons (b and t quarks and the third type of neutrino $\nu_\tau$ ) must exist. All predictions of the SM were perfectly confirmed by experiments [6]. Only one prediction of the SM, existence of the scalar neutral Higgs boson, is still waiting for its confirmation. The search for the Higgs boson will be one of the primary goal of the LHC collider at CERN.

At the CMS detector [7] at $\sqrt{s}$=7 and 8 TeV in proton-proton collisions standard model Higgs boson was searched. The excess of events is observed above the expected background, with a local significance of 5.0 standard deviations, at a mass near 125 GeV, signalling the production of a new particle. The expected significance for a standard model Higgs boson of that mass is 5.8 standard deviations.

Despite the success of the SM, there are many reasons to believe that the SM is an effective theory which is only valid up to 1 TeV.

# Chapter 2

# CMS and the Muons

A gold-plated signal of the Higgs Boson is the decay into $ZZ$ which in turn decays into four charged leptons (Fig. 2.1).

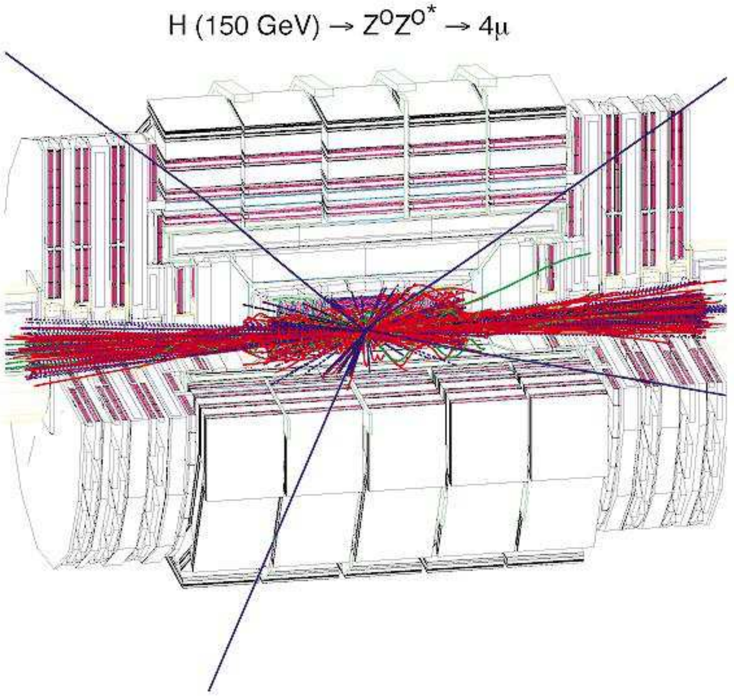

**Figure 2.1.** A Higgs event decaying into four muons in the CMS detector [8].

If the leptons are muons, the best 4-particle mass resolution can be achieved, and muons are less affected than electrons by radiative losses in the tracker material.

The $H \longrightarrow W^+W^- \longrightarrow l^+l^-\nu\nu$ is also important, needs a very accurate missing $E_T$ measurement. Independent NNLO calculation of these relevant decay modes ($H \longrightarrow \gamma\gamma$, $H \longrightarrow W^+W^- \longrightarrow l^+l^-\nu\nu$ and $H \longrightarrow ZZ \longrightarrow 4$ leptons) has been known for some time [9], precise measurements are needed for the comparison.

Therefore two important detector requirements are the:

1. Good electromagnetic energy resolution, good diphoton and dielectron mass resolution (1% at 100 GeV),

2. Good muon identification and momentum resolution over a wide range of momenta in the region $|\eta| < 2.5$, good dimuon mass resolution (1% at 100 GeV).

The principal part of my work with CMS is the alignment of muon chambers, the detailed desciption of the detector is in [10], I focus on the muon part.

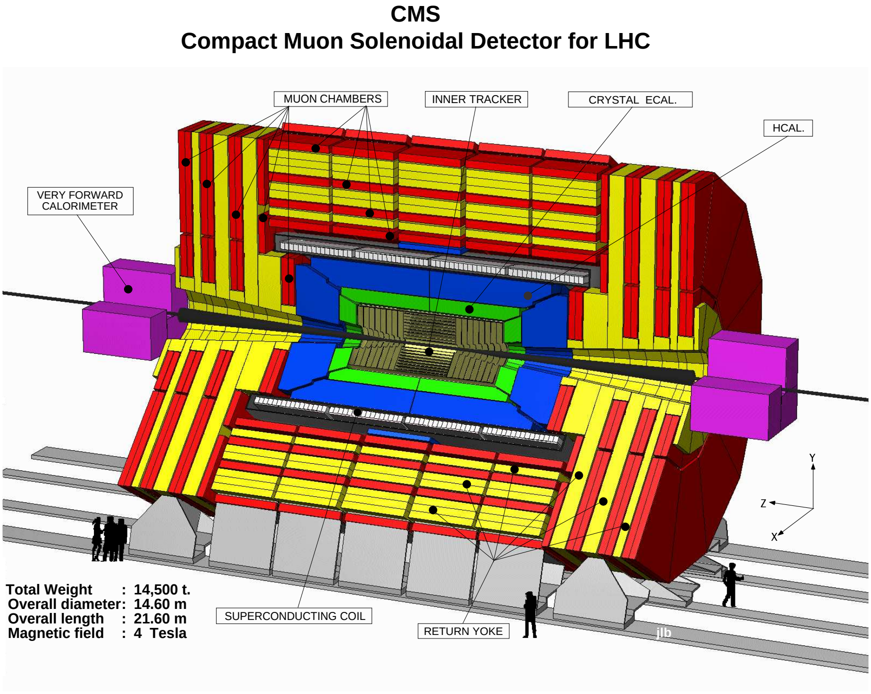

**Figure 2.2.** CMS Detector

## 2.1 Muon System

The overall layout of CMS is shown in Fig. 2.2 At the heart of CMS sits a 13m long, 5.9 m inner diameter, 4 T superconducting solenoid. In order to achieve good momentum resolution within a compact spectrometer without making stringent demands on muon-chamber resolution and alignment, a high magnetic field was chosen. The return field is large enough to saturate 1.5 m of iron, allowing 4 muon stations to be integrated to ensure robustness and full geometric coverage. Each muon station consists of several layers of aluminium drift tubes (DT) in the barrel region and cathode strip chambers (CSCs) in the endcap region, complemented by resistive plate chambers (RPCs).

The muon system has three purposes [8]: muon identification, muon trigger, and muon (signed) momentum measurement. A robust 4 T solenoid-based system is the key to the CMS design. Comprehensive simulation studies have indicated that the physics goals can be achieved if the muon detector has the following functionality and performance:

1. Muon identification: at least 16 $\lambda$ of material is present up to $|\eta|$=2.4 with no acceptance losses[1].

2. Muon trigger: the combination of precise muon chambers and fast dedicated trigger detectors provide unambiguous beam crossing identification and trigger on single and multimuon events with well defined $p_T$ thresholds from a few GeV to 100 GeV up to $|\eta|$=2.1.

3. Standalone momentum resolution: from 8 to 15% $\delta p_T / p_T$ at 10 GeV and 20 to 40% at 1 TeV.

4. Global momentum resolution: after matching with the Central Tracker: from 1.0 to 1.5% at 10 GeV, and from 6 to 17% at 1 TeV. Momentum-dependent spatial position matching at 1 TeV less than 1 mm in the bending plane and less than 10 mm in the non-bending plane.

5. Charge assignment: correct to 99% confidence up to the kinematic limit of 7 TeV.

6. Capability of withstanding: the high radiation and interaction background expected at the LHC.

The initial rate of 40 MHz has to be reduced by the First Level Trigger down to 30 kHz by looking for objects like muons, electrons/photons, jets, missing transverse

---

[1] $\lambda$ is the nuclear interaction length, $\eta$ is the pseudorapidity, defined as $\eta = -\ln\tan(\theta/2)$

energy and total transverse energy. One can roughly assume an equal sharing of this bandwidth between muon and calorimeter triggers.

### 2.1.1 Muon Detectors

#### Barrel Region

The barrel muon system [8] of the CMS detector consists of four stations integrated in the return yoke of the magnet. The basic sensitive element of the chambers is a drift cell (Fig. 2.3) of approximately 400 ns maximum drift time.

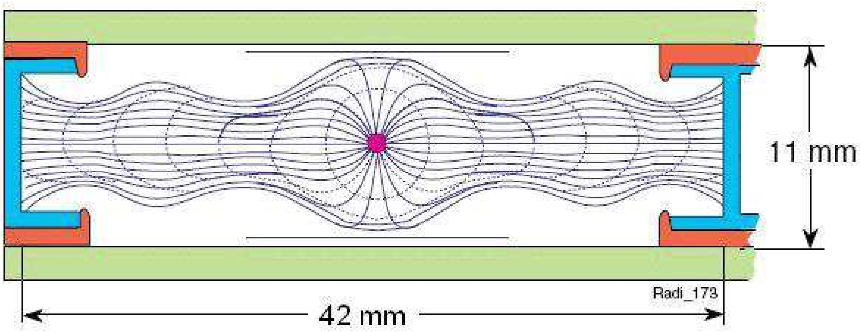

**Figure 2.3.** Drift cell

At the center is the anode wire (+3600 V), made out of 50 micron diameter stainless steel. There are four electrodes to shape an effective drift field: two on the side walls of the tube (-1800 V), and two above and below the wires on the ground planes between the layers (+1800 V). With this arrangement the requirement of 250 micron resolution per layer (which guarantees 100 microns per chamber) can be obtained while operating the tubes at atmospheric pressure with a binary $Ar/CO_2$ gas mixture.

The twelve planes of drift tubes present in every chamber (Fig. 2.4) are organized in three independent subunits called Super Layers (SL) made up of four planes with parallel wires. Two SLs measure the coordinate in the bending plane ($\Phi$), the third measures the track coordinate along the beam ($z$). The two $\Phi$ SLs have a separation of about 23 cm, in order to obtain the best angular resolution. This is the maximum allowed by the space available. Between them are the $z$ SL and a thick honeycomb plate used as a spacer.

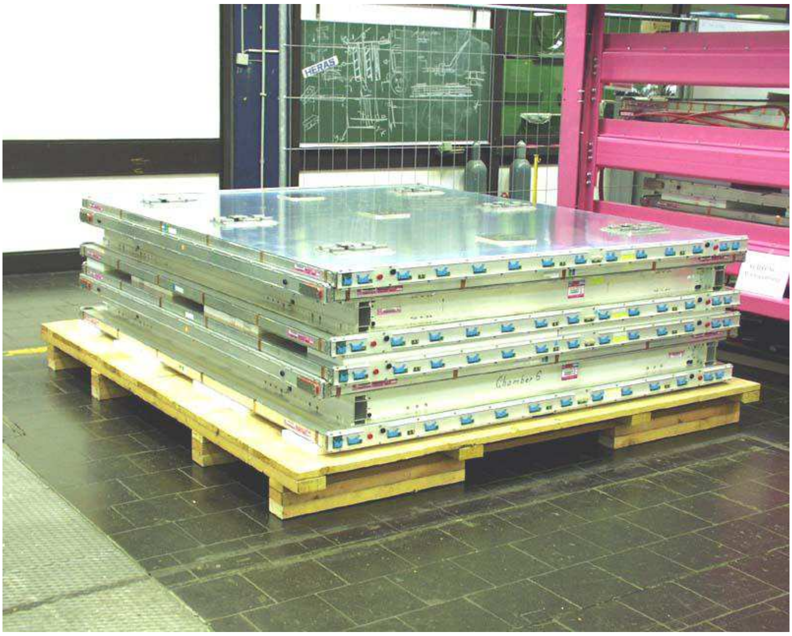

**Figure 2.4.** Two DT chambers wait for calibration [11]

Within a SL, the four layers are staggered by half a cell, making it possible to use the correlation of the drift times in the different planes to compute the coordinate and the angle of the crossing tracks without any external time tag. The mean timer is fast enough to be used in the first-level trigger.

The obvious redundancy of the system, four stations of twelve planes each, makes it possible to cope with inefficiencies due to the dead zones which are caused by the supporting iron ribs, by the longitudinal space allowed for services, and by the non-negligible probability for a high energy muon to produce electromagnetic showers when exiting the iron slab.

### Endcap Region

Each endcap region of CMS has four muon stations of Cathode Strip Chambers (CSCs). These chambers have trapezoidal shape and are arranged in a series of concentric rings centered on the beam line. This cathode strip chamber has been chosen for the endcaps since it is capable of providing precise space and time information in the presence of a high and highly non-uniform magnetic field and high particle rate. CSC is a multiwire proportional chamber consist of positively-charged anode wires crossed with negatively-charged copper cathode strips within a gas volume.

Each CSC has six layers of wires sandwiched between cathode panels therefore, each chamber provides six measurements of the $\Phi$-coordinate (strips) and six measurements of the $r$-coordinate (wires).

### RPCs

CMS has added planes of resistive plate chambers (RPCs) in both the barrel and endcaps to provide an additional, complementary trigger.

RPCs are gaseous parallel-plate chambers that combine a reasonable level of spatial resolution with excellent time resolution, comparable to that of scintillators. In the muon system, these chambers cover roughly the same area as the DTs and CSCs but provide a faster timing signal and have a different sensitivity to background. Trigger signals coming from the drift tubes, cathode strip chambers, and the RPCs proceed in parallel until reaching the level of the global trigger logic. This provide redundancy for evaluating efficiencies, and result in a higher efficiency and greater rate capability.

## 2.1.2 Momentum Measurement

There are many factors that limit the ability of the muon system to measure accurately the momentum of a traversing muon [8]:

1. Multiple scattering in the calorimeters and in the thick steel plates separating the muon stations;
2. The intrinsic resolution of the detectors;
3. Energy loss, especially when it is catastrophic;
4. Extra detector hits generated by muon radiation, X-rays, and other backgrounds;
5. Chamber misalignment;
6. Uncertainty of the B field.

The contributions of many of these effects to the muon momentum resolution measurement have been studied using CMSIM, based on GEANT code.

In CMS most of the muons bend through the full 4T magnetic field and reach the maximum curvature near the first muon station (Fig. 2.5). This station gives the main contribution to the momentum measurement precision and leads to the most stringent requirements on chamber resolution and position accuracy.

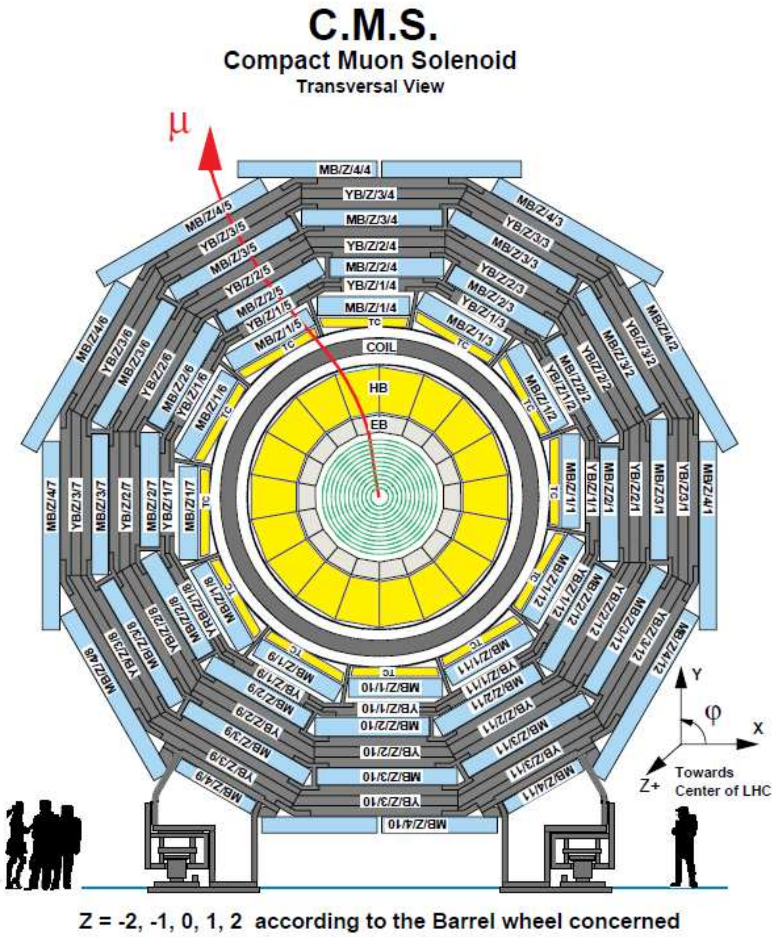

**Figure 2.5.** Transversal view of the CMS detector

To set bounds on the required accuracy, the influence of the chamber misalignment on the momentum resolution has been studied [12] for both barrel and endcap detectors. The required accuracy, in $r - \Phi$, for the barrel detector is in the range of 150-350 $\mu$m (for MB1-MB4 respectively), while for the endcap system it is 75-200 $\mu$m (for ME1- ME4). In both cases, looser requirements are set for muon identification and triggering.

# Chapter 3

# CMS Alignment

Stability of the muon chambers at the 100 $\mu$m level is not guaranteed during detector operation, due to the varying magnetic field, thermal motions and structural fatigue. The expected movements and deflections of the muon spectrometer exceed the requirements. To cope with movements, the detector is instrumented with an optical alignment system, which allow continual measurement of the chambers position. The alignment information is used for off-line correction in track reconstruction.

The system must provide accurate alignment of the barrel and endcap muon detectors among themselves as well as alignment between them and the inner tracker detector. To fulfill these tasks the CMS alignment system is organized in three blocks:

1. Internal alignment of the inner tracker to measure positions of the different tracker detector modules and monitor internal deformations. It will allow us to consider the tracker as a rigid body.

2. Local alignment of Barrel and Endcap muon detectors to monitor the relative position of the muon chambers in the detector.

3. A Link system to relate the muon (barrel and endcap) and tracker alignment systems, and allow a simultaneous monitoring of the detectors.

The full system is segmented in six $\Phi$-planes (active alignment planes) to which the three tracking detectors are connected. During detector operation, these systems must track the large changes from survey positions.

## 3.1 Endcap Alignment

There is a need for instrumented position monitoring in the CMS endcap systems because each return yoke iron plate, to which the muon cathode strip chambers (CSCs) were directly attached, change its shape under the extremely high magnetic field forces from the solenoid. Also there are some thermal motion of the chambers. For these reasons, the muon chambers shift in position and orientation relative to detector open, field free survey positions. In order to trigger on and define the correct position of passing particles (after software alignment correction), mechanical chamber positions and orientations need to be known with a reasonable tolerance, especially the $r$ coordinates and angle rotations. The typical total error is in $r - \Phi$ plane is around 200 $\mu$m but is smaller at the first plate: 75 $\mu$m. In the radial direction is required to monitor chambers with 400 $\mu$m accuracy and it can be 1 mm along the $z$ direction.

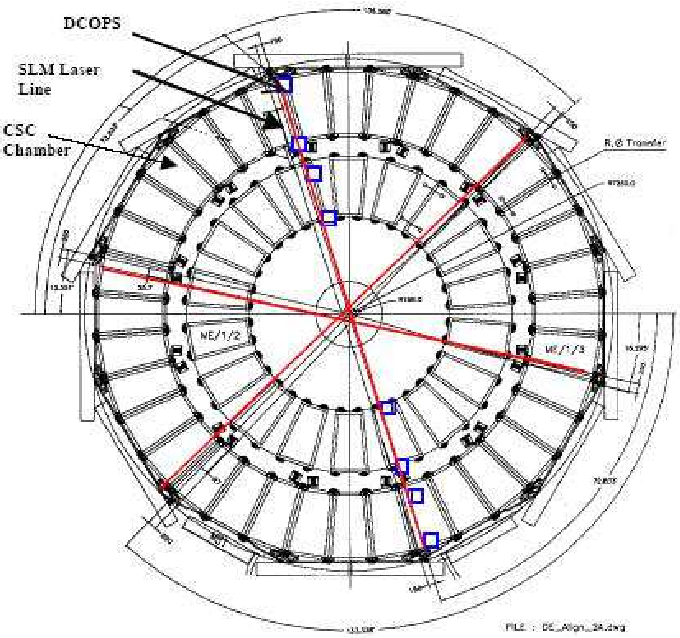

Figure 3.1. Straight Line Monitors of the Endcap Alignment System

Twelve interleaved endcap Rasnik Straight Line Monitors (SLMs) [13] are on each plate of the two endcaps (Fig. 3.1). Each SLM consists of laser beams detected by two Digital CCD Optical Position Sensors (DCOPS) in each of the four crossed chambers.

Approximately one sixth of the CSCs are directly monitored by these sensors, the rest are aligned with respect to these monitored chambers by detecting tracks that pass through their overlapping regions.

The system uses six transverse laser lines provide an optical connection between the forward and backward muon endcaps, across the barrel wheels. By connecting to the Link-Barrel system, the positions of the Endcap system can be defined relative to the tracker and barrel muon systems.

## 3.2 Link System

The Link system is designed to relate the position monitoring systems of the inner tracker and muon detectors. The light paths define planes in $\Phi$, every $60^0$. This segmentation, although redundant, allows a direct reference of each barrel muon sector with the tracker detector and provides direct tracker references to the endcap monitoring system.

To minimize the interference with other subdetectors the light path follows the inner detector boundaries and reaches the muon region through radial light channels in the endcap iron disks. Four primary points on the MAB (Module for Alignment of Barrel) structures are used to reference the barrel and endcap alignment systems in this plane. The measurement of the MAB positions with respect to the tracker alignment wheels uses a total of eight linking points along each light path: four placed at the tracker ends and four at the MAB structures. The $\Phi$ orientation MAB-Tracker cannot be directly obtained with this geometry, so it is measured independently by laser levels (laser tilt sensors) placed on the MAB and tracker alignment wheels.

## 3.3 Barrel Alignment

The monitoring system for the barrel part is designed to measure the positions of the barrel chambers with respect to each other (internal monitoring). The position of the whole barrel muon system is related to that of the Central Tracker and the Endcap muon system via the Link system [8].

The scheme based on the monitoring of the muon chamber positions with respect to a network of 36 rigid mechanical reference structures called MABs. These are fixed to the barrel yoke forming 12 $r - z$ planes parallel to the beam and distributed in $\Phi$ (Fig. 3.2). Six of them (called active planes) are connected to the Link system. The other six planes (called passive planes) are connected to the active ones via diagonal connections.

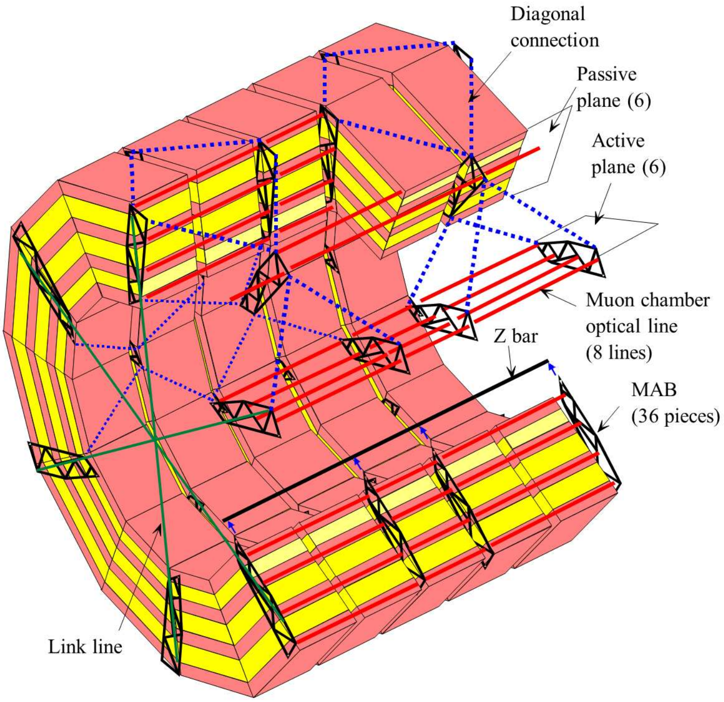

**Figure 3.2.** The structure of the Barrel Muon Alignment System.

The position of the anode wires cannot be monitored directly, the positions of light sources rigidly fixed to the barrel muon chambers are monitored. The frames with the light sources are mounted to the rigid honeycomb structures to the alignment passages (two on each side, 0.5 m from the corner). Each of the 36 MABs contains 8 camera boxes which observe light sources mounted on the muon chambers. The position of a light source is determined by the calculation of the centroid of the light intensity distribution falling on the sensor of the camera.

The MABs also contain 4 bunch of light sources (on the active planes) or 4 camera boxes (on the passive planes) providing the diagonal connections (see the blue lines on the Fig. 3.2). In addition, all 24 MABs of the 6 active planes are also equipped with cameras measuring the $z$ positions by observing carbon-fiber bars called Z-bars installed on the vacuum tank of the CMS magnet. All the 12 MABs that are connected to the link system (the outer MABs of the active planes) contain also elements belonging to the link and endcap systems.

The $r$ and $\Phi$ positions are measured directly by the camera-box by measuring the corresponding light sources' positions (There are 40 light sources per muon chamber, 20-20 on both sides/passages). The $z$ (only for the chamber corners close to camera-boxes) are measured by triangulation, measuring the relative positions of two light sources mounted on the same frame.

### 3.3.1 MAB

The MABs are rigid structures made of carbon-fiber tubes and carbon-reinforced-carbon composite plates glued together.

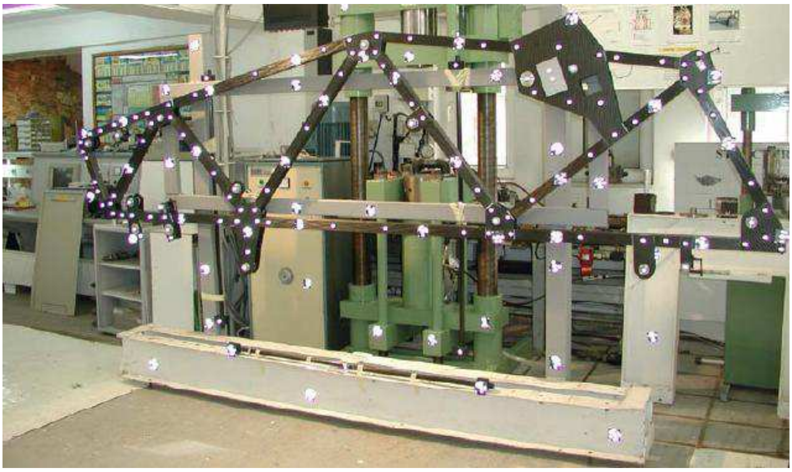

**Figure 3.3.** MAB on the calibration bench [11].

Each MAB is fixed to the barrel yoke at three points in an isostatic way, allowing it to move without deformation. The rigidity is achieved by the construction, the choice of the material, and the assembly technology.

Due to lack of rotational symmetry of the barrel muon system, the MABs have to be different. There is also a difference between the outer MABs connected to the Link and the inner ones.

#### Camera-Box

A camera-box consists of a CMOS video-sensor, optical elements (lens, holes) and a mechanical box made of carbon-fiber material to minimize the deformation due to temperature effects and to reduce the weight. The analog videosensor with 384×287 pixels, and 12×12 mm$^2$ pixel size [14] is suitable for the given application.

The total number of camera boxes is 360, the number of sensors is 600 due to the double camera boxes on the inner MABs.

### Diagonal LED

There are 288 LED light sources on the MABs for the diagonal connections. These LEDs are on the MAB of the active planes, 4 diagonal LED holder per MAB.

### Thermometer and Humidity Meter

To measure the thermal effect on the chambers, there are 144 thermometer and humuidity meter (Fig. 3.4) on the MABs.

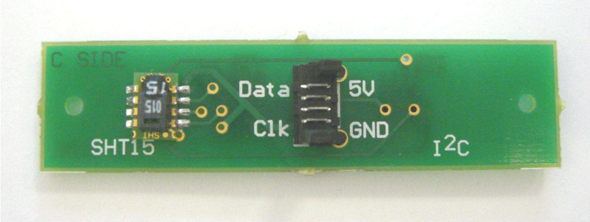

**Figure 3.4.** Thermometer and humidity meter [11].

## 3.3.2 Z-bar

The z position of a MAB of an active plane with respect to the other MABs of the same plane is measured by a light sources - camera box pair. The light sources are installed in a holder on the carbon fiber bars (Z-bars) fixed on the vacuum tank of the magnet parallel to the beam. The camera-boxes are fixed to the MABs. There are 6 Z-bars on the active planes (see Fig. 3.2) and there are 24 Z LEDs in 4 Z-holders on a Z-bar.

## 3.3.3 Light Source

The muon barrel position monitoring system contains more than 10000 light sources. These light sources have to fulfill the following requirements:

1. Good visibility (including their intensity) in the full longitudinal and transversal range of the measurements.
2. Stable position of the centroid of the light intensity distribution.
3. Long lifetime.
4. Low price.

To fulfill all these requirements, LEDs have been chosen as light sources to be used in the barrel monitoring system. 10 LEDs are located in the LED holder (Fig. 3.5), in the fork.

**Figure 3.5.** The LED holder, the fork. In the fork 10 LEDs are located [11].

6 LEDs are on the side, that faces outside and 4 on the other side. 1000 forks were put in operation on the 250 chambers.

As it was mentioned, the position of the anode wires cannot be monitored directly, during the production of the chambers, before closing the Super Layer, some machined aluminum pieces, corner blocks were glued to the gas-tight box, and that were positioned at known coordinates with respect to the wires.

### 3.3.4 Board Computer and Minicrate

The full system is controlled by a SCADA (Supervisory Control and Data Acquisition) workstation located in the control room [15]. The electronic components located on the muon chambers are controlled by the intelligent Minicrate. The Minicrate communicates with the Detector Control System (DCS) and the commands from the supervisory level are distributed to the specific modules through I2C bus. This protocol allows connecting up to 127 individual devices with different addresses on the same bus with 1 kHz clock frequency. The power of the LED holder modules is supplied also by the Minicrate.

For local control, collection of the data from the video cameras and the sensors as well as the calculations of the centroids is performed by local computers installed at the MABs. These computers are built up as a stack of PC/104 [16] cards and called as board computers (BC) see Fig. 3.6, there are 36 of them.

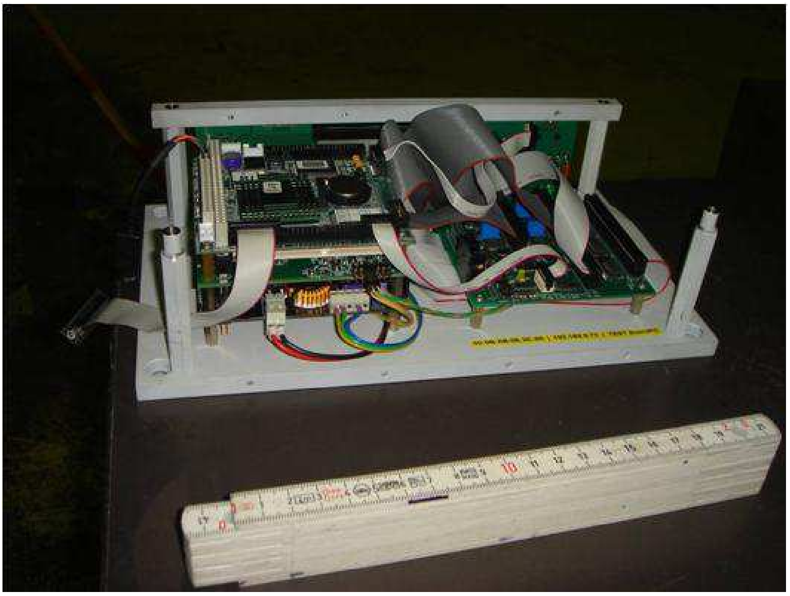

**Figure 3.6.** There are frame locker (left-up), processor (left-middle), power supply (left-down) and custom board (right) on the board computer [11].

The board computers have a 96-Mbyte DiskOnChip, where the operating system and the application program and data can be placed. The operating system is chosen to be a Linux system, where most of the required tasks have their supporting tools. These are the device drivers of the frame locker, the ethernet interface and the DiskOnChip itself. The last one is very crucial, because without having the proper format on the DiskOnChip, the system cannot boot, the MAB with its all element cannot be used.

DIM is a communication system for distributed, mixed environments, it provides a network transparent inter-process communication layer. It is used in different CERN experiments where several servers are making data acquisition and measurement control, and clients in several places want to have online data and control information. In our case the board computers will be the DIM servers.

The application program should perform the tasks below:

1. Read and save the pictures of the connected cameras through the FrameLocker, and to calculate the centroids of the images of the LEDs in the pictures.
2. Switch on/off the z-bar LEDs and the diagonal LEDs mounted on the MAB

3. Publish services and available commands for the DIM name server.

The SCADA system supervises part of the LEDs mounted on the muon chambers through direct control and controls the rest of the system by sending commands to the BCs and receiving results from them through the Ethernet network, using the DIM protocol. The user interface is provided and the database is supervised by the specialized process supervising and visualization software, PVSS II.

### 3.3.5 Calibration

Only the LEDs on the forks are monitored by the barrel alignment system, a calibration procedure was needed to relate the wires to the LEDs. This calibration is made in three steps:

1. Measurement of the wire positions with respect to the corner blocks during the chamber production.

2. Measurement of the LED position to the reference points of the fork before the DT calibration.

3. Measurement of the fork position with respect to the corner blocks during the DT calibration.

The last two steps, the calibration the visible objects to the corner block, could be done in one step, but in the case of a fork replacement, a new DT calibration would be needed, which is a very long procedure. There are reference points and planes on the forks and on the DTs also, all the calibration results are stored in databeases, at a fork replacement we only need to change one record in the database.

#### LED holder Calibration

The LED is not a point-like light source, all the LEDs were calibrated to the reference points of the fork [11], the precision of the calibration was less than $15\mu$m in the plane of the fork (in $r - \Phi$) and $200\mu$m in $z$. The LED holder, the fork is mounted on the calibration tool (Fig. 3.7) sitting on a precision x-y micrometer table driven by stepper motors [15]. The LED sources are observed by video cameras on both sides of the calibration tool. During the calibration procedure the light spot of the LEDs were sequentially moved to the same position on the picture of the video camera. The relative coordinates of the LEDs can be derived from the x and y positions.

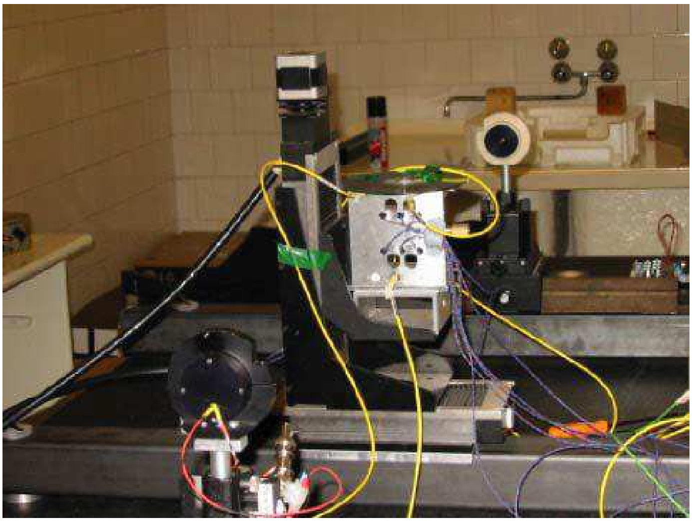

**Figure 3.7.** The LED holder calibration bench at the Debrecen University [15].

### Muon Chamber Calibration

The $4\times5$ m$^2$ chamber calibration bench installed at CERN is shown in Fig. 3.8. The bench is designed to calibrate all the chamber types of different widths in the range of 2-4 m.

**Figure 3.8.** The chamber calibration bench at CERN [15].

The positions of the LED holders on the chambers are measured by fixed video cameras. The position of the chamber body in the laboratory coordinate system is measured by photogrammetry. Combining the two measurements the position of the LED holders can be determined with 60-70 $\mu$m precision with respect to the corner block. The chamber database contains the full geometry of each chamber including the characteristics of the LED holders mounted on it and its location in CMS.

### 3.3.6 Measurement

During the operation of the system the centroid of the LEDs' light are detected by the video cameras and the centroid calculated by the BC. At the initialization of the run the workstation in the control room connect to the online CMS database to query the optical objects to be measured. An array of threads is created, each thread contains the optical object (LED), the optical connection (which camera can detect that LED) and all the hardver IDs that needs to swich on the light of the LED and take pictures by the camera. If there is a thread that has all the needed resources, the system starts it, reserve the resources, switches on the LED and send command to the corresponding BC to take the pictures and calculate the centroids. After taking 20 pictures an average centroid is calculated, a result array is created with the comment, that this result is ready to send to the online CMS database. At the end of a thread execution the resources became free again. There are additional threads for the CMS DCS communication, thread for creating statistics (running threads, expected end of the measurement...) and threads for the temperature and humidity measurement. In general there is a continuous run, after finishing the measurement of all the available LEDs, new run is started. One run takes about 2 hours, several thousands of run were done.

## 3.4 Geometrical Reconstruction

### 3.4.1 COCOA

CMS Object-oriented Code for Optical Alignment (COCOA) is a C++ software that is able to reconstruct the positions, angular orientations, and internal optical parameters of any optical system described by a combination of many different types of optical objects. The software is currently in use by the different optical alignment systems of CMS and is integrated in the CMS framework in the CMSSW.

Due to the unknown movement of the objects, the sensors of the optical alignment systems will not provide the expected measurement values. The aim of the software is to analyze the change in the measurement values and to be able to determine which are the changes in position or rotations.

There is no need to know the explicit form of the equations of the system, only the derivatives of each measurement value with respect to each object parameter. COCOA uses a geometrical approximation of the propagation of light to calculate numerically these derivatives and then solves the system of equation through a non-linear least squares method [17]. Due to the big number of parameters, big sparse matrices are needed.

We have to only describe our system in an input ASCII file with a clearly documented format, select which parameters are known and which unknown and give measurements of the system. COCOA will then reconstruct the positions, rotations angles and internal parameters of the objects that build the system and will also propagate the errors of the measurements and the calibrations.

### 3.4.2 Use of COCOA

In ths CMS software framework (CMSSW) the COCOA is a part of the Alignment package, can be installed as CocoaApplication[1]. Once the software is installed is to type 'cocoa' at the command line, then the software looks for a System Description File (SDK). SDK has a well defined structure: Global Options, System Tree Data, System Tree Description and Measurement. In the Global Options there are the parameters for the system and the operation. In the System Tree Description is listed the components of the system. In the Measurement are listed the position of the light sources detected by the sensors. From the available components (laser, x-hair laser, (incoherent) source, pinhole, lens, mirror, plate splitter, cube splitter, rhomboid prism, optical square, sensor1D, sensor2D, COPS, distance-meter, distance target, tiltmeter) we use the source, pinhole and the sensor2D.

#### Global Options

By default, the coordinates and their erros are given in millimeters and the rotation angles and their errors are given in radians, but in our case the errors are given in micrometer and millirad. These setups, with additional paremeter for the iteration (maximum number of loops, fit quality...) are given in the Global Options.

#### System Tree Description

The system is given in a hierarchical structure. In our case the system has MABs and DTs. There are three kind of MABs, the internal and the passive with 16 camera

---

[1] There are instructions at http://kismalac.phys.klte.hu/ ujvarib/GoodToKnow/

boxes, these are 8 double camera boxes, but during the calibration they were separated to 16 individual camera boxes. The external has 8 single camera boxes, since these MABs are at the end of the barrel. The camera box has pinhole and sensor2D. The DT has two passages, each has two forks, the forks has 10 LEDs.

```
SYSTEM_TREE_DESCRIPTION
object system Barrel
object Barrel 12 extMAB 12 passMAB 12 intMAB 180 DT
object extMAB 8 cambox
object intMAB 16 cambox
object passMAB 16 cambox
object cambox pinhole sensor2D
object DT 2 passage
object passage 2 fork
object fork 10 source
```

Every system made of objects and contain another objects. The convention is set, that an object called ’system’ is always built and the tree objects are basic objects (source and sensor2D), COCOA knows how they behave.

### System Tree Data

The name and the default positions of the objects, as the starting points of the iteration, are given in the System Tree Data. Using the name convention in the System Tree Description above, the objects are given in the following structure:

```
system s
Barrel CMSBarrel
 centre
 X 0 0 fix
 Y 0 0 fix
 Z 0 0 fix
 angles
 X 0 0 fix
 Y 0 0 fix
 Z 0 0 fix
```

The system ’s’ contains the CMSBarrel is on the (0,0,0) and all the angles of the rotation are also 0. The CMS Barrel has three kind of MABs (external, internal and passiv), one MAB consist of camera boxes, it has pinhole and sensor (see the structure in System Tree Description above). The position of the MAB is unknown ’unk’, but the deafult position based on the photogrammerty measurement is a good starting point.

```
extMAB EXTN_1
 centre
 X 4273.200195 5000.000000 unk
 Y 1545.300049 5000.000000 unk
 Z -6691.000000 5000.000000 unk
 angles
 X 90.000000 2.000000 unk
 Y 0.000000 2.000000 unk
 Z -165.570007 2.000000 unk
```

The camera box position is not really fixed ’fix’ by the calibration. In the COCOA there is calibrated ’cal’ type for the object’s position with known uncertainity, but due to the small uncertainity of calibration and the large number of elements, these calibrated values are set to ’fix’. One more reason, why ’cal’ is not used, is the following. Every day there are close to 10 full measurements, all the LED positions are calculated on the sensor. In an ideal case there are COCOA runs for every measurement, using ’cal’ for the position of the camera box means, that it can be changed run by run, which is hard to imagine, the camera box is very stable on the MAB.

```
cambox cam_INT1R //camID: 399
centre
X 249.748795 1000.000000 fix
Y 62.014030 1000.000000 fix
Z 212.848434 1000.000000 fix
angles
X 269.229462 0.050000 fix
Y 13.096660 0.050000 fix
Z 358.401794 0.050000 fix
```

The camera box is defined by the pinhole in the middle, the position of the sensor is given by the calibration.

```
pinhole lens
centre
X 0.000000 0.000000 fix
Y 0.000000 0.000000 fix
Z 0.000000 0.000000 fix
sensor2D vsensor_INT1R
centre
X 0.000000 0.000000 fix
Y 0.000000 0.000000 fix
Z -29.806120 10.000000 fix
```

```
angles
X -0.196670 0.500000 fix
Y -0.908020 0.500000 fix
Z 0.000000 0.000000 fix
```

The System Tree Data for the DTs is very similar, there are nominal positions for the DTs as starting points of the iteration. The DT has two passeges, calibrated by the photogrammetry, each passage has two forks, calibrated by the chamber calibration. The fork has 10 LED sources, calibrated by the LED holder calibration at the Debrecen University. The light sources were used as fix objects in COCOA. It was mentioned that the calibrations' uncertainity were less than 15$\mu$m in the plane of the fork (in $r - \Phi$) (the required accuracy is 150-350$\mu$m in $r - \Phi$) accordingly it could be a 'fix' objects.

All of the calibrated paremeters are set to 'fix', instead of 'cal', the other reason, besides the unphysical movement of the camera box, is the run time. The number of equation are solved by COCOA is proportional to the number of 'unk' and 'cal' parameters. There are more than 1000 unknown parameters (positions and angles of the MABs and DTs), the rest (~30000) should be calibrated. If these calibrated parameters are set to fixed, the run of the COCOA uses ~10GB of memory for about 10 hours. Setting all the calibrated to 'cal', the run would be impossible.

### Measurement

The measurement has three parts:

```
SENSOR2D
s/CMSBarrel/DT_N1_1_1R/DTpass12/Fork_N1_1_1_1/FLED_N1_1_1_1_1
& s/CMSBarrel/PASN_12/cam_INT1R/lens
& s/CMSBarrel/PASN_12/cam_INT1R/vsensor_INT1R
H -1.052280 0.500000
V 1.103880 0.500000
```

With the `SENSOR2D` is described how the measurement was taken, then the path of the light is defined, the name in the System Tree is used to identify the objects in this structure. The path is started from the LED source:
system→CMSBarrel→DT_N1_1_1R chamber →DTpass12 the chamber's passage→ Fork_N1_1_1_1 one of the two forks in the passage → FLED_N1_1_1_1_1 one of the 10 LEDs on a fork.
The light goes through the pinhole:
system→CMSBarrel→PASN_12 MAB→cam_INT1R camera → lens,
and is detected by the sensor:
system→CMSBarrel→PASN_12 MAB→cam_INT1R camera → vsensor_INT1R.

The following lines are the values of the measurement with their errors. In the case of a sensor2D there are two measurements, that are identified by the keywords 'H' for the Horizontal measurement and 'V' for the Vertical one.

Since there are discrepancies in the position for every object signed by 'unk', the COCOA, based on the measurements, makes a fit, changing the unknown parameters to give the best result.

### 3.4.3 Result of COCOA

COCOA finds the best value and error of the unknown ('unk') parameters to the best fit of the measurements. The iteration ends depend on the parameters given in the Global Options. There can be several iterations, in each of them COOCA changes the values of the unknown and calibrated parameters and calculates the fit to the measurements. In the first few iterations the fit quality, the $\chi^2$, decreases drastically:

```
initial Chi2 = 6.69893e+09
Chi2 after iteration 0 = 1.13261e+06
Chi2 after iteration 1 = 1080431.8
Chi2 after iteration 2 = 1080286.3
Chi2 after iteration 3 = 1080286.2
```

In the last few loops the changes are very small, the iteration ends by the global parameters:

```
maxNoFitIterations 50
fitQualityCut 0.0001,
```

if the number of iterations are more than 50, or the decrease of the chi square in a loop is smaller than 0.0001, the changes of the object parameters don't decrease the fit quality significantly.

## 3.5 COCOA Input File Generation

The input file for COCOA has a clear structure, for a few objects it's really easy to make by hand. The Endcap and Link Alignment have hundreds of objects, there was no need to automate this file generation. At the Barrel Alignment one active plane with the station 1,2,3 (∼1000 objects and ∼1000 measurements) was the first complex try for reconstruction. It was done by hand and took several weeks to run without any typos. COCOA is a powerful tool for fitting the measurement to the system, but does not help to find e.g. the permutated numerals, only the drastically increasing $\chi^2$ of the fit shows the large typos, the small ones are very hard to find.

Since all the measurements, calibrations, optical connection (sensor - LED pairs) were in databases (MySQL and Oracle) the Root [18] was used for the automatization, it has an easy to use interface for databases. A Data Quality Management (DQM) is used at every objects. Based on the DQM script's result the file generator uses (e.g. the fork is added to the system if there are enough working LED on it) or does not use (e.g. chamber is not added to the system if there are no valid forks on the passages) the object and it's measurements

At first the system and the CMSBarrel are created. With an sql query all the chambers with their IDs are selected. With the next query the validation of the chamber is probed, if the chamber is not valid, the next chamber from the previous selection is used. The position of the valid chamber is the result of the next query. The forks of the chamber, their validation and their positions are selected from the database in the next step. Finally the LED positions on the fork is read out from the calibrations database. The other major part of the code is the MAB selection. There is no DQM for the MABs, the invalid MABs are removed by hand. In the first query the IDs and the positions of the valid MABs are selected. The IDs and the positions of the camera boxes of this MAB are derived from the configuration database than the positions of the sensor from the calibration database.

The sensor in the camera box, the camera box on the MAB and the fork on the chamber are exchangeable, the date of the change is added with a timestamp to the configuration database. In these cases the timestamp is also included in the query to reconstruct the old and the new runs with the same code.

The measurement part of the COCOA file also uses the DQM scripts, no measurements for the invalid (and in the System Tree not included) objects are allowed.

### 3.5.1 Station 1,2,3 and Station 4

Already in this early phase it was clear, that with the station 4 the reconstruction of the MABs' positions were out of the expected precision. After the first automated COCOA file generator with the databases were ready to use, the first test was the reconstruction of one active plane. The result of the COCOA run contains also the fit quality, the $\chi^2$ of the current iteration, if the $\chi^2$ of the next iteration is smaller than the previous one, the objects were moved in the right way to explain better the masurement. From this reconstruction different stations were removed, the fit quality is shown by the $\chi^2$ in Tab. 3.1.

The barrel reconstruction has two steps. At first the COCOA file, contains the chambers of the first three stations and all of the MABs, is created. In this file the unknown parameters are the positions and angles of the chambers and the MABs. The reason is the MAB calibration. During the MAB calibration, the MABs' camera boxes of the first three stations were homogeneous in position on the bench. The targets, were used for their calibration, were fixed, the uncertainity of the calibra-

| used stations | $\chi^2$ of the COCOA run |
|---|---|
| 1,2,3,4 | 315881.61 |
| 1,2,4 | 223899.92 |
| 1,3,4 | 247772.19 |
| 1,2,3 | 125865.01 |

**Table 3.1.** $\chi^2$ of the reconstruction

tion was small. Since all these calibrations had very small uncertainities, the starting points are very close to the real positions on the MAB structure , the iteration has only few steps (see example in 3.4.3).

For the cameras of the station 4, the calibration method was different, the targers were to move for every MAB, the uncertainity were larger. Furthermore, there are double chambers at the sector 4 and 10 (see Fig. 2.5) where only one passages is measured, large uncertainity in their rotation is added to the reconstruction. Since there are larger uncertainity, there are more iterations, the runs are longer. To speed the iteration up and decrease the error of the reconstruction, the position of the MABs were set to 'fix', their values were taken from the same run of the first three station. In this case only the parameters of the chambers at the station 4 are unknown.

Our final, full barrel model's reconstuctions were validated by track alignment and used in the cosmic ray run and in 2010 and 2011 in every analysis which used the muon positions, see in [19] and [20].

## 3.6 Missing MABs

Light sources of one chamber are detected by four cameras [2]. Since $z$ position of the chambers is measured by triangulation using the closest light source measurement to the MAB, missing MABs can complicate at first the $z$ measurement, more missing MABs in a plane are expected to have effect on the $r - \Phi$ precision, but the impact on the full reconstructon is a very complex question.

The following MABs were lost in 2010 and 2011:

1. MAB (Wheel/Sector): +1/9
   Reason of loss: Custom Board firmware problem.
   First bad measurement during the run on 29.05.2010.

---

[2] detailed description was created by Zoltan Szillasi, see on http://kismalac.phys.klte.hu/cgi-bin/Insertion/Insertion_unrolled.pl

2. MAB: -2/10
   Reason of loss: Unknown.
   First bad measurement during the run on 18.08.2011.
3. MAB: +1/7
   Reason of loss: Unknown.
   First bad measurement during the run on 18.08.2011.
4. MAB: -3/7
   Reason of loss: Unknown.
   First bad measurement during the run on 18.08.2011.

The system was off due to power cut before 18.11.2011. that can be the reason of the failure of the lastthree MABs. However, they can be investigated only after opening the CMS detector in early 2013.

To study the recostruction with and without all of the MABs an validated run (taken on 07.03. 2010., when all the 36 MABs were still operational.) was choosen. With my automated COCOA file generator several configurations were created to compare the results. In every reconstruction the DT 0/1/1 (wheel/sector/station) was fixed to the photogrammetric measurement. The reconstructed positions of the MABs installed on the central wheel obtained from the 1,2,3 and 4 missing MABs model were then fit on those of the non-missing MABs reconstruction. As a result of this fit both reconstructions are expressed in the same coordinate system, and the differences show only the local displacements and rotations.

### 3.6.1 Differences of the reconstructions

It's assumed that if there was a physical movement of a chamber, due to e.g. a termal effect or the huge magnetic field, after reconstruct the run before and after this effect, calculated the difference, this difference is close to the physical one. Similar methods are used in this case, where the same runs are reconstructed with different number of MABs. The physical motions are excluded only the impact of the 4 missing MABs in reconstruction appears in the differences (Fig. 3.9) There are two coordinate systems used in the barrel muon system: global and local. The global one is identical to the CMS coordinate system: origin at the interaction point, global X is directed towards the center of sector 1, global Y is oriented towards the center of sector 4, global Z is towards the center of wheel +2. Also, the corresponding cylindrical system (R,Φ, Z) is used as well. In the local system of individual DT chambers the local x′ is oriented along the global $R - \Phi$, the local y′ is along the global Z and the local z′ is along the global R. On this type of plots the displacement and rotation are multiplied by 200, the unit is the chamber size.

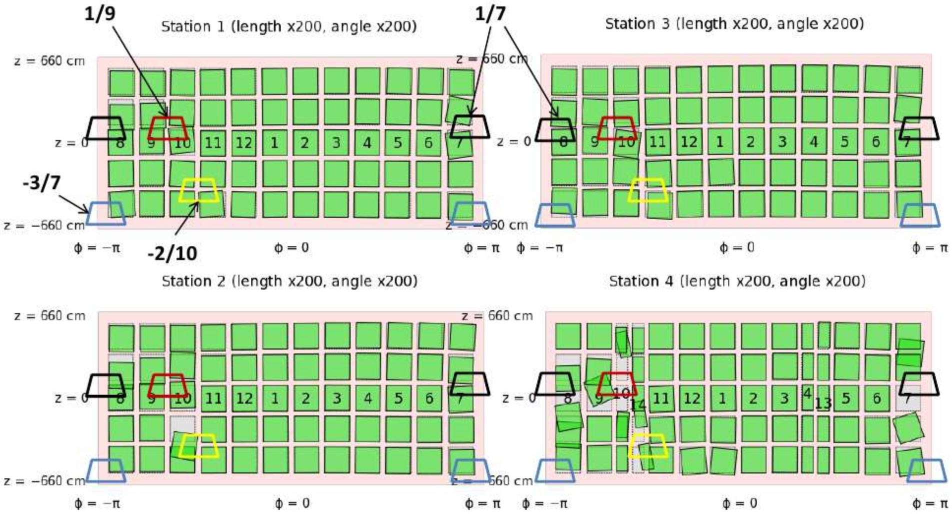

**Figure 3.9.** Unrolled view of the differences between the reconstructions with and without the missing MABs in local x′, y′ and rotation around local z′.

It's obvious that the differences are restricted to the sectors 7, 8, 9 and 10(, 14 at station 4 the chambers in sectors 10 and 14 are double chambers on the top and 4,13 on the bottom). The distributions of local x′, local y′ and rotation around local z′ (rot(z′)) are shown on Figs. 3.6.1 through 3.6.1, two groups were created: DTs in sectors 7,8,9,10(,14) (blue), and DTs in the rest of the sectors (red) and for all the chambers is shown (black). The RMSs are given in Table 3.2- 3.4.

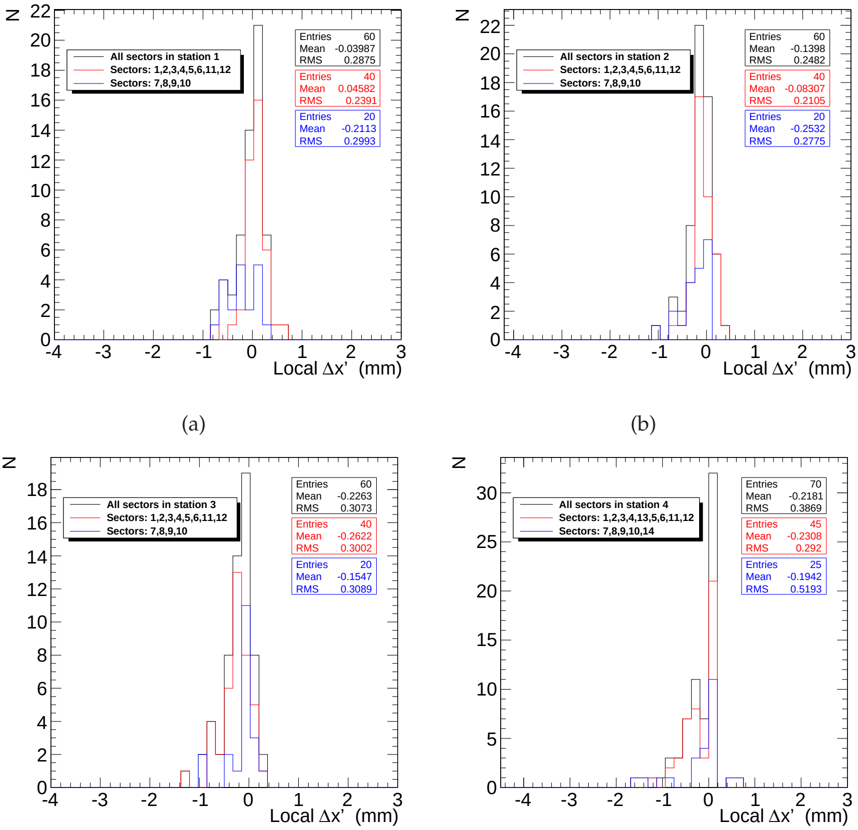

(a) (b)

(c) (d)

**Figure 3.10.** Differences in local x′ for stations 1-4

| RMS of delta local x′ | Sector 7, 8, 9, 10 | Sector 1, 2, 3, 4, 5, 6, 11, 12 |
|---|---|---|
| station 1 | 0.2993 mm | 0.2391 mm |
| station 2 | 0.2775 mm | 0.2105 mm |
| station 3 | 0.3089 mm | 0.3002 mm |
| station 4 | 0.5193 mm | 0.2920 mm |

**Table 3.2.** RMSs of delta local x′ in the two groups of sectors

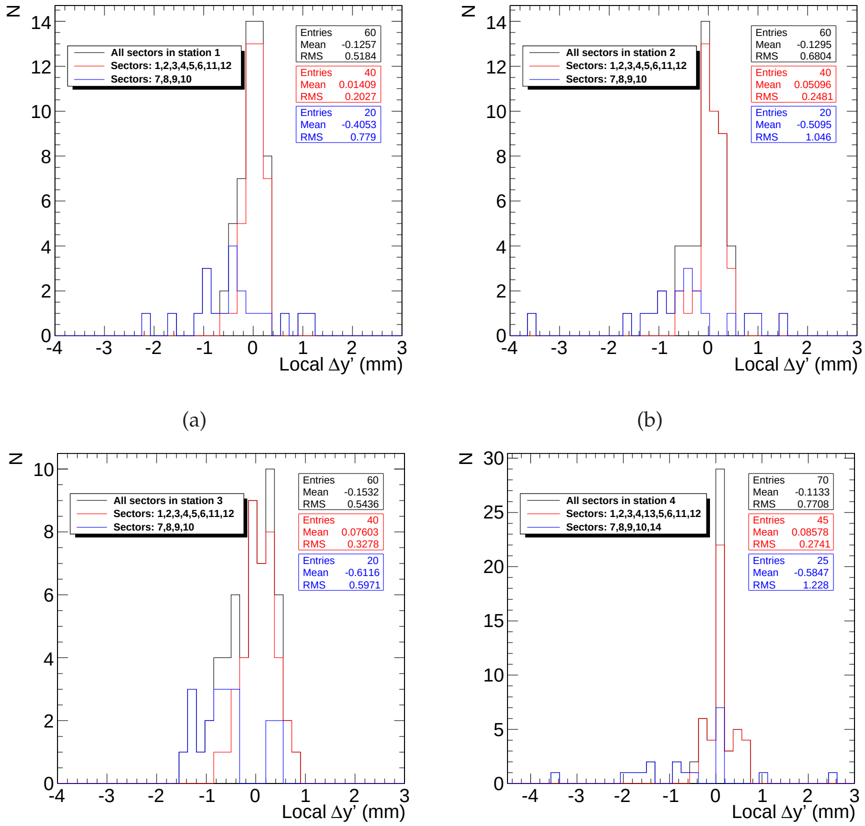

(a) (b)

(c) (d)

**Figure 3.11.** Differences in local y′ for stations 1-4

| RMS of delta local y′ | Sector 7, 8, 9, 10(, 14) | Sector 1, 2, 3, 4(, 13), 5, 6, 11, 12 |
|---|---|---|
| station 1 | 0.7790 mm | 0.2027 mm |
| station 2 | 1.0460 mm | 0.2481 mm |
| station 3 | 0.5971 mm | 0.3278 mm |
| station 4 | 1.2280 mm | 0.2741 mm |

**Table 3.3.** RMSs of delta local y′ in the two groups of sectors

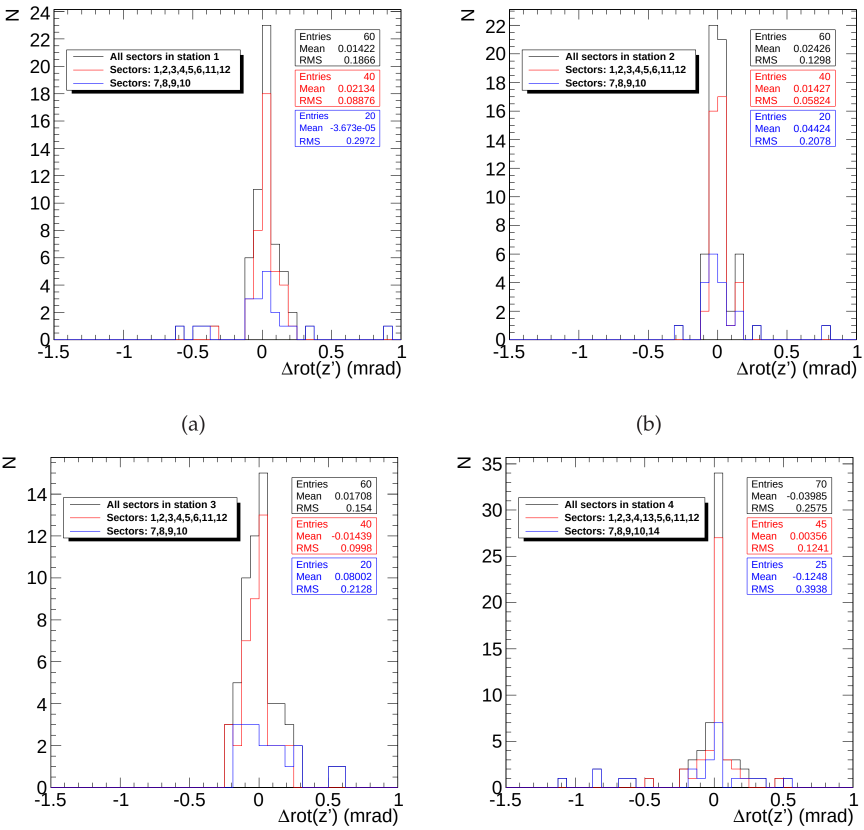

(a) (b)

(c) (d)

**Figure 3.12.** Differences in rot(z′) (explanation in the text) for stations 1-4

| RMS of delta rot(z′) | Sector 7, 8, 9, 10(,14) | Sector 1, 2, 3, 4(,13), 5, 6, 11, 12 |
|---|---|---|
| station 1 | 0.2927 mrad | 0.0888 mrad |
| station 2 | 0.2078 mrad | 0.0582 mrad |
| station 3 | 0.2128 mrad | 0.0998 mrad |
| station 4 | 0.3938 mrad | 0.1241 mrad |

**Table 3.4.** RMS of rotation around local z′ (rot(z′)) in the two groups of sectors

The rotation around local y′ (global Z), local x′ and local z′ can be seen on the transversal view (Fig. 3.13), the displacement and rotation are also multiplied by 200, the unit is the chamber size. The additional rotation in the area of missing MABs is clearly connected to the fact that some chambers are measured only at one side and the measurement of the other side is weak or missing. With the rotation around local y′ it was easy to show the impact of the missing or weak planes in the reconstruction, but it induced only second order effect on the muon momentum measurement.

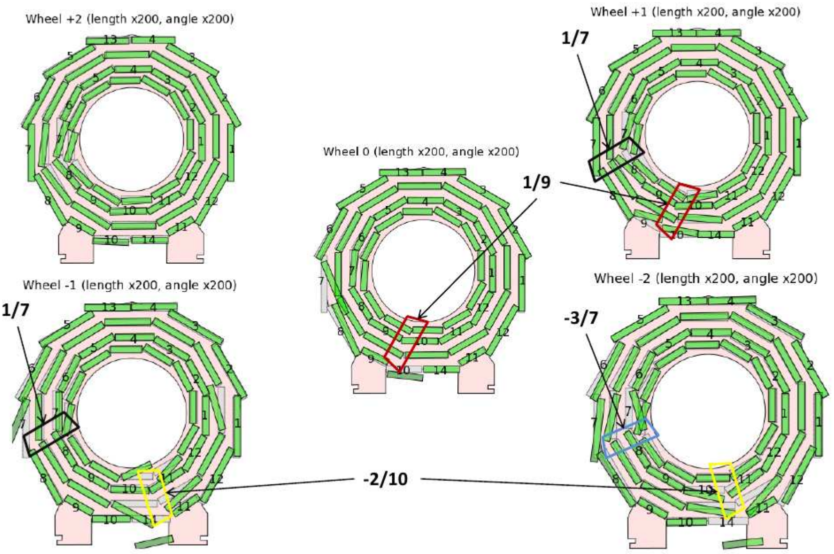

**Figure 3.13.** Transversal view of the differences between the reconstructions with and without the missing MABs in local x′, z′ and rotation around local y′

| RMS of delta rotation local y′ | Sector 7, 8, 9, 10, 14 | Sector 1, 2, 3, 4, 13, 5, 6, 11, 12 |
|---|---|---|
| wheel -2 | 0.7080 mrad | 0.3316 mrad |
| wheel -1 | 1.0110 mrad | 0.4104 mrad |
| wheel 0 | 0.5584 mrad | 0.0833 mrad |
| wheel +1 | 0.8279 mrad | 0.0699 mrad |
| wheel +2 | 0.6983 mrad | 0.0748 mrad |

**Table 3.5.** RMS of delta rotation local y′ in the two groups of sectors

Due to the redundancy and robustness of the measurement and the reconstruction of the chamber positions the RMS of the differences in sectors 1, 2, 3, 4, 13, 5, 6, 11, 12 remain inside the required precision and the RMS of the differences in the sectors 7, 8, 9, 10, 14 (missing MAB sectors) are still at a tolerable level. Even with the missing MABs, the momenta of muons can still be reconstructed with the expected precision using our alignment results.

# Chapter 4

# Theory of photon interactions

All fundamental fermions except the electrically neutral neutrinos can interact via the electromagnetic force. This is mediated by virtual photon ($\gamma$) exchange and described by Quantum Electrodinamics (QED). QED and its unification with the weak interaction is a gauge field theory.

The strong force is mediated between quarks by exchange of eight coloured bosons called gluons ($g$). The strong force binds the quarks together. It is described by Quantum Chromo Dynamics (QCD). QCD is a non-abelian gauge field theory.

The photon has no self-coupling and therefore a process of the kind $\gamma\gamma \to \gamma\gamma$ can happen only via a charged particle loop to which the photons couple [22]. For very low energy photons, with energies much smaller than the lightest known charged particle the cross-section is extremely tiny. Photons at high energy, on the other hand, can fluctuate into a two-fermion pair or even a bound state, i.e. a vector meson with $J^{PC}$ quantum numbers as for the photon: $J^{PC} = 1^{--}$. The usefulness of attributing a corresponding hadronic structure to the photon is in its universal character: the structure measured in a particular interaction (e.g. two photon interactions at LEP) can be transported to a different kind of photon interaction (e.g. photon-proton scattering at HERA).

## 4.1 Direct and resolved photon

**Figure 4.1.** Direct photon

**Figure 4.2.** Hadron-like photon

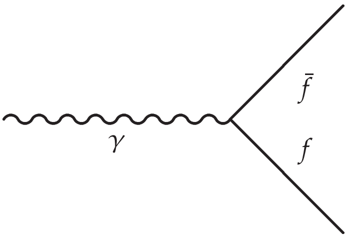

**Figure 4.3.** Point-like photon

The reactions of the photon are usually classified depending on the object which takes part in the interaction. In the following we call the photon *direct* (Fig. 4.1) if it interacts with another object as a whole quantity and *resolved* if it interacts through one of the fermion produced in the quantum fluctuation [23]. If a photon fluctuates into a pair of leptons, the process can be completely calculated within QED, if it fluctuates into a pair of quarks, then the situation is much more complicated, because of QCD interactions. Interactions of such photons are well described by the Vector Meson Dominance (VMD) model - the photon turns first into a hadronic system with quantum numbers of vector mesons and the hard interaction takes place between partons of the vector meson and a probing object. This contribution to the photon structure usually cannot be calculated perturbatively and has to be parametrized in terms of the parton distribution function in the photon. Due to the similarity to the structure of hadrons the contribution is called $hadron - like$ (Fig. 4.2). Only when the quark pair has a sufficient relative transverse momentum, $p_T > k_0$ (of order 0.5 GeV), the process is perturbatively calculable in QCD, this contribution to the photon structure is called $point - like$ (Fig. 4.3)

The six main event classes are characterized by the transverse momentum scale $p_T$ of the $q\bar{q}$ fluctuation divides the phase space into perturbative and non-perturbative regions, are the following:

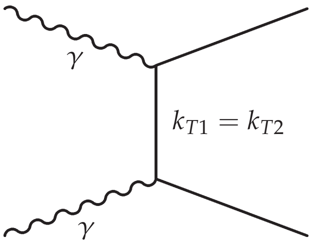

**Figure 4.4.** Direct×direct

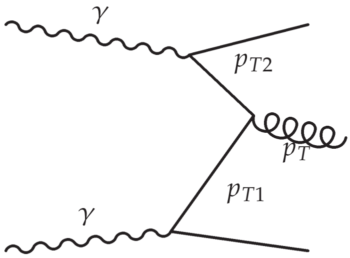

**Figure 4.5.** Direct×point-like

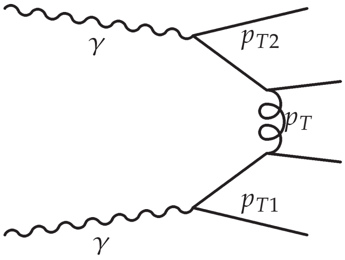

**Figure 4.6.** Point-like×point-like

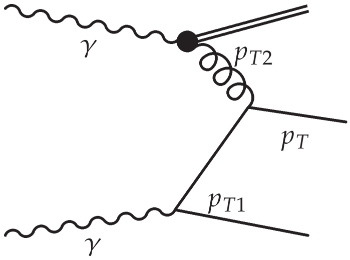

**Figure 4.7.** Direct×VMD

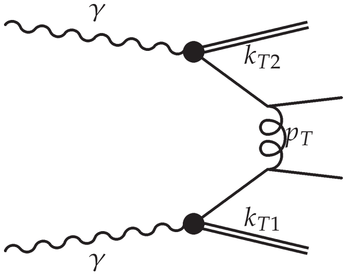

**Figure 4.8.** VMD×VMD

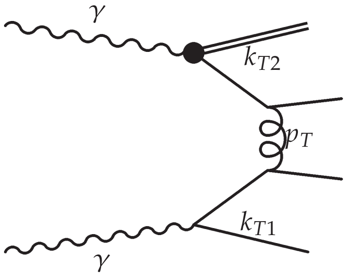

**Figure 4.9.** Point-like×VMD

- direct×direct - the photons directly produce a quark pair
- direct×point-like - one photon splits into a $q\bar{q}$ pair and one of them interacts directly with the other photon
- point-like×point-like - both photons split into $q\bar{q}$ pair, one parton from each photons takes part in the hard interaction
- direct×VMD - a direct photon interacts with a parton of VMD photon
- VMD×VMD - both photons turn into hadrons and then interact like hadrons
- point-like×VMD - one photon splits into a $q\bar{q}$ pair and one of these interacts with a parton of VMD photon

## 4.2 Kinematics

In this section I introduce the kinematical variables used to describe the leading-order fermion pair production,

$$e_1(p_1)e_2(p_2) \rightarrow e_1(p_1')e_2(p_2')\gamma^{(*)}(q)\gamma^{(*)}(p) \rightarrow e_1(p_1')e_2(p_2')f(p_{f_1})f(p_{f_2}) \qquad (4.1)$$

The terms in parentheses denote the four vectors, the symbol $(*)$ indicates that the photon can be either quasi-real ($q^2 \approx 0$) or virtual ($q^2 < 0$) . The four vectors, energies and polar scattering angles of the outgoing particles can be seen on Fig. 4.10.

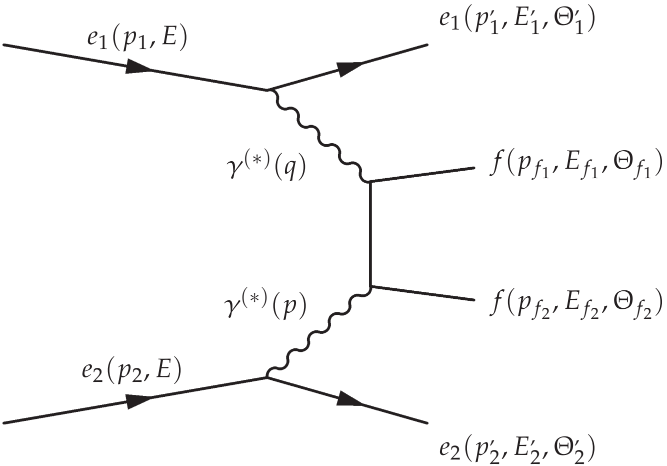

**Figure 4.10.** Leading order interaction [24]

The list of commonly used variables is given (we neglect the lepton masses):

$$Q^2 = -q^2 = 2EE_1^{'}(1 - \cos\Theta_1^{'}) \geq 0 \qquad (4.2)$$

$$P^2 = -p^2 = 2EE_2^{'}(1 - \cos\Theta_2^{'}) \geq 0 \qquad (4.3)$$

$$s_{ee} \equiv (p_1 + p_2)^2 = 2p_1 \cdot p_2 = 4E^2 \qquad (4.4)$$

$$s_{e\gamma} \equiv (p_1 + p)^2 \qquad (4.5)$$

$$s_{\gamma\gamma} \equiv W_{\mathrm{gen}}^2 \equiv (q + p)^2 = Q^2\frac{1-x}{x} - P^2 \qquad (4.6)$$

$$x \equiv \frac{Q^2}{2p \cdot q} = \frac{Q^2}{W^2 + Q^2 + P^2} \qquad (4.7)$$

$$W_{\mathrm{vis}}^2 = (\sum_{\mathrm{h}} E_{\mathrm{h}})^2 - (\sum_{\mathrm{h}} \overrightarrow{p_{\mathrm{h}}}/c)^2 \qquad (4.8)$$

## 4.3 Cross-section

In the framework of the QCD-improved parton model, the cross-section of inclusive single hadron production is described as a convolution of hard scattering, parton density functions (PDF's) and fragmentation functions (FF's). The photon, probed at short distance, reveals parton properties, this structure is quantified in terms of PDF. Perturbatively calculable part is the short distance cross-section of dirtect photon interaction (photons interact without inner hadronic struction), parton-photon interaction (partonic content of photon interacts with the photon) and parton-parton interaction. The FF characterize the transition of the partons come out of the hard scattering to the hadron that finally hit the detectors. The factorization theorem [25] ensures that the last two part of the convolution are universal and only first changes when different processes are considered. While the partonic cross-sections may be perturbatively calculated from the QCD Lagragian, this is not yet possible for the PDF's and FF's of hadrons and one has to determine them by fitting experimental data. The PDF's of photons, which are needed to describe the $\gamma\gamma$ reactions, are already highly constrained by measurements of deep-inelastic $e\gamma$ processes. We consider the reaction

$$e_1(p_1)e_2(p_2) \rightarrow e_1(p_1')e_2(p_2')h(p_h)X, \tag{4.9}$$

where h is the observed hadron and X includes all unobserved hadrons.

### 4.3.1 The Equivalent Photon Approximation

The high energy electron[1] beam radiates a photon, and thus produces a beam of high energy photons. The energy spectrum for the produced photon is well described by the equivalent photon approximation (EPA). The idea of the EPA belongs to Fermi [26], who paid attention to the fact that the field of a fast charged particle is similar to an electromagnetic radiation.

When we speak of $\gamma\gamma$ collision with almost real photons, we have in mind the $e^+e^-$ collision process where the electrons act as sources of nearly massless, collinear photons, which collide with each other to produce hadrons in the final state. In the EPA, the inclusive cross-section of the process in Eq. 4.9 is related to that of the corresponding $\gamma\gamma$ reaction,

$$\gamma_1(p_1)\gamma_2(p_2) \rightarrow h(p_h)X \tag{4.10}$$

---

[1] Positrons are also referred to as electrons.

through

$$\begin{aligned} E_h \frac{d^3\sigma(e_1e_2 \to e_1e_2hX)}{d^3p_h} &= \int_{x_1^{min}}^{1} dx_1 \int_{x_2^{min}}^{1} dx_2 F_{\gamma_1/e_1}(x_1) F_{\gamma_2/e_2}(x_2) \\ &\times E_h \frac{d^3\sigma(\gamma_1\gamma_2 \to hX)}{d^3p_h}, \end{aligned} \tag{4.11}$$

where $x_i = E_i^{\gamma}/E_i$ and $F_{\gamma_i/e_i}(x_1)$ $(i = 1, 2)$ are the photon-spectrum functions. The lower bounds of integration, $x_i^{min}$, are fixed by kinematics. The quasireal-photon spectrum in the EPA is [27]

$$\begin{aligned} F_{\gamma/e}(x) = &\frac{\alpha}{2\pi} \frac{1 + (1-x)^2}{x} \ln \frac{E^2\Theta_{max}^2(1-x)^2 + m_e^2x^2}{m_e^2x^2} \\ &+ 2(1-x)\left( \frac{m_e^2x}{E^2\Theta_{max}^2\,(1-x)^2 + m_e^2x^2} - \frac{1}{2} \right), \end{aligned} \tag{4.12}$$

where $x = E_\gamma/E_e$ was varied in [27] over the full range allowed by kinematics and the antitagging angle was choosen as $\Theta_{max} = 30$ mrad. The photon beam will consists of many low energy photons, that are not important in the recent collision kinematics, and little high energy ones.

### 4.3.2 Parton Distribution and Fragmentation Functions

QCD, the theory of the strong interaction is required in the description of processes involving hadrons [28]. The best tool for solving QCD to perform such descriptions is perturbation theory, however perturbative QCD (pQCD) can only describe the high energy components of the cross-section, while a process will contain low energy components if a hadron in the inital or final state. Fortunately the low and high energy scale components of such processes can be separated. The low energy components can not be calculated from QCD, must be extracted from experimental data. However, the low energy components are universal, can be used to make predictions.

The last factor in Eq. 4.11 in the parton model is expressed as follow:

$$\begin{aligned}
E_h\frac{d^3\sigma(\gamma_1\gamma_2\to hX)}{d^3p_h} &= \int\frac{dx_h}{x_h^2}\sum_c D_{h/c}(x_h,M_h^2)\left(p_c^0\frac{d^3\sigma(\gamma_1\gamma_2\to cX)}{d^3p_c}\right.\\
&+\sum_a\int dx_a F_{a/\gamma_2}(x_a,M_{\gamma_2}^2)\frac{d^3\sigma(a\gamma_2\to cX)}{d^3p_c}\\
&+\sum_b\int dx_b F_{b/\gamma_1}(x_b,M_{\gamma_1}^2)\frac{d^3\sigma(\gamma_1 b\to cX)}{d^3p_c}\\
&+\sum_{ab}\int dx_a F_{a/\gamma_2}(x_a,M_{\gamma_2}^2)\int dx_b F_{b/\gamma_1}(x_b,M_{\gamma_1}^2)\\
&\left.\times p_c^0\frac{d^3\sigma(ab\to cX)}{d^3p_c}\right).
\end{aligned}\tag{4.13}$$

Here, the parton indices $a, b, c$ run over the gluon and the flavours[2] of quarks and antiquarks, $k_a = x_a p_2^\gamma$, $k_b = x_b p_1^\gamma$ and $k_c = p_h/x_h$ are the parton momenta, $F_{a/\gamma}(x_a, M_\gamma^2)$ is the PDF of parton $a$ inside the photon and $D_{h/c}(x_h, M_h^2)$ is the FF of parton $c$ into hadron $h$. The factorization scales, $M_\gamma$ and $M_h$ will be specified in 4.4. The first term of the Eq. 4.13 is the direct-photon contribution (DD), the second and the third ones are the once-resolved contribution (DR) and the fourth one is the twice-resolved contribution (RR). In LO (Leading Order) the DD contribution is of $O(\alpha^2)$, where $\alpha$ is the electromagnetic coupling constant. The LO hard-scattering cross-sections in the DR and RR components are of $O(\alpha\alpha_s)$ and $O(\alpha_s^2)$ respectively. There exist several parton distribution functions for real, and also for virtual photons at leading and next-to-leading order accuracy [24].

## 4.4 Inclusive diffraction

The cross-sections are calculated at NLO for direct, single- and double-resolved processes. For the PDF the AFG-HO parametrisation of the parton densities of the photon [29] is used in the $\overline{\text{MS}}$ renormalization and factorisation scheme with $N_F = 5$ active quark flavours and $\Lambda^5_{\overline{MS}} = 221$ MeV. The $\mu = M_\gamma = M_h$ are set equal to $\xi p_T$, where $\xi$ is a dimensionless scale factor will be used for the determination of uncertainty of the calculation and $p_T$ is the transverse momentum of the hadron. They took the NLO FF's for charged pions, charged kaons and the (anti)protons [28] and sum over them. The differental inclusive charged hadron production cross-section, $\mathrm{d}\sigma/\mathrm{d}p_\mathrm{T}$ for $|\eta|^3$<1.5 and $\mathrm{d}\sigma/\mathrm{d}|\eta|$ for $p_\mathrm{T}$ >3.5 GeV were measured and calculated.

---

[2] the number of flavours depend on the energy, for the recent calculation added in 4.4

[3] In the OPAL coordinate system the $x$ axis points towards the centre of the LEP ring, the $y$ axis points upwards and the $z$ axis points in the direction of the electron beam. The polar angle $\theta$, the azimuthal

The condition $p_{\mathrm{T}} > 3.5$ GeV was determined by the uncertainty of the NLO calculation where it is comparable with the uncertainty of the measurement. In Fig. 4.11/b shows measurement subtracted from the NLO calculation, with different scale parameter, divided with the total uncertainty of the measurement. At 3.5 GeV the uncertainty from the scale variation exceeds significantly the uncertainty of the measurement. The distance between the dashed (or dotted) lines in the low-$p_{\mathrm{T}}$ region is larger than 1 (100%) that means the uncertainty of the scale variation dominates. In the lower-$p_{\mathrm{T}}$ region the NLO calculation even with the default $\xi = 1$ scale parameter not able to describe the cross-section (the solid line goes up to 10), as it expected in the perturbation QCD.

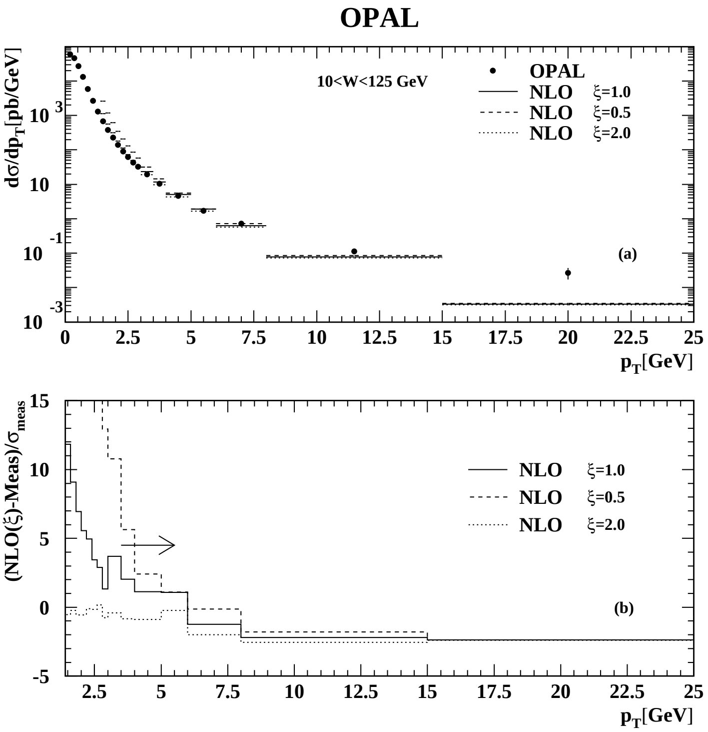

**Figure 4.11.** Uncertainty of the NLO calculation by varying the scale factor [27].

---

angle $\phi$ and the radius $r$ denote the usual spherical coordinates. The pseudorapidity $\eta$ is defined as $\eta = -\ln\tan(\theta/2)$.

# Chapter 5

# OPAL detector and LEP

## 5.1 OPAL at LEP

The Large Electron Positron (LEP) collider at CERN was a storage ring that had a circumference of 27 km designed to produce $Z^0$ and W particles via the annihilation of electrons and positrons.

Accelerated charged particles emit synchroton radiation and thus lose energy given by $\Delta E \propto E^4/(m^4 R)$, where the $E$ is the electron energy, $m$ the mass and $R$ is the radius of the orbit. The loss is counteracted by the use of radio frequency (RF) cavities which use electromagnetic waves to accelerate the bunches. LEP had the following elements in each standard cell of the lattice: a defocusing quadrupole, a vertical orbit corrector, a group of six bending dipoles, a sextupole, a focusing quadrupole, a horizontal orbit corrector, a second group of six bending dipoles and another sextupole.

OPAL (Omni Purpose Apparatus for LEP), Fig. 5.1, was a multipurpose apparatus designed to reconstruct efficiently and identify all types of events. The OPAL experiment took data from 1989 until 2000, and the detector was dismantled in 2001. Full details of the OPAL detector can be found in Ref. [31], and only a brief introduction is given here.

### 5.1.1 The Central Detector

The central detector (CD) consisted of a silicon microvertex detector and three drift chamber devices [32], the vertex detector, jet chamber (CJ) and surrounding Z-chambers situated inside a pressure vessel holding a pressure of 4 bar. The central detector was inside a solenoid which supplied a uniform axial magnetic field of 0.435 T.

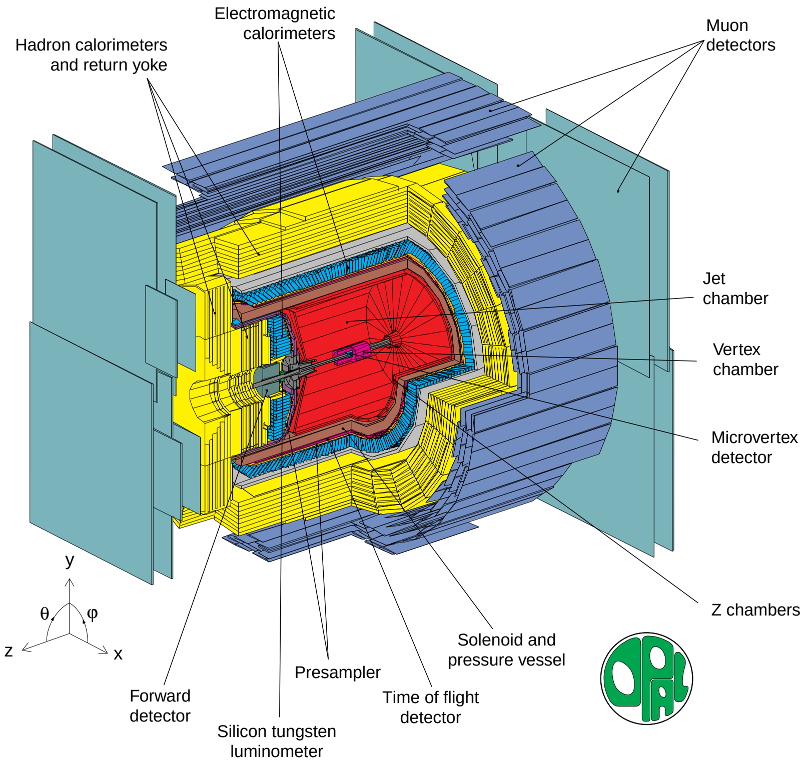

**Figure 5.1.** The OPAL detector

The central jet (CJ) chamber, surrounded the CV, was a large volume gaseous detector, starting at a radius of 0.245 m and extending to a radius of 1.85 m, and was approximately 4 m long. The chamber has 24 sectors, each of which contained a plane of 159 anode sense wires parallel to the z axis. These wires were spaced at 10 mm intervals, lied parallel to the beam direction. In between these sense wires were the potential wires, cathode wire planes separated sectors. With at least 20 points measured for 98% of the $4\pi$ solid angle. The jet chamber allowed the measurement of charged particle momenta by recording the bending of particle paths caused by the 0.435 T solenoidal magnetic field in the central part of OPAL. In addition, particle species identification was provided by measuring the rate of energy loss of particles traversing the chamber. The average resolution in $r - \phi$ plane was 135 $\mu m$ and the average z resolution was 6 cm. The momentum ($p_T$ in GeV) in the $r - \phi$ plane was measured with a resolution given by:

$$\sigma(p_T)/p_T = \sqrt{0.02^2 + (0.0015 \cdot \mathrm{p_t})^2} \tag{5.1}$$

### 5.1.2 Magnet

The magnet consisted of a water cooled solenoid and an iron yoke to provide the flux return. The solenoid was wound in one complete unit to prevent discontinuities causing non-uniformities in the magnetic field. The iron yoke also provided at least four interaction lengths for the sampling hadron calorimeter. The magnetic field as was mentioned in the central tracking region was 0.435 T paralell to the $z$-axis and was uniform within $\pm 5\%$.

### 5.1.3 Electromagnetic Calorimeter

The electromagnetic calorimeter (ECAL) system measured the energies and positions of electrons, positrons and photons, ranging from tens of MeV up to beam energy. It was a total absorption calorimeter for electromagnetic showers and was mounted between the coil and the return yoke of the magnet. It consisted of three large assemblies of leadglass blocks, the barrel and two endcaps. These covered 98% of the solid angle. Leadglass was chosen for its excellent intrinsic energy resolution ($\sigma_E/E \sim 5\%/\sqrt{\mathrm{E}}$ where E is the electromagnetic energy in GeV). The angular resolution of electromagnetic clusters was $\sim$4 mrad both in $\theta$ and $\phi$ for energies above 10 GeV.

### 5.1.4 Hadron Calorimeter

The hadron calorimeter (HCAL) measured the energy of hadrons that emerged from the electromagnetic calorimeter and assisted in muon identification. The iron of the return yoke provided at least 4 interaction lengths of absorber over 97% of the $4\pi$ solid angle. The yoke wss segmented into layers, with planes of wire chambers between each layer, and formed a cylindrical sampling calorimeter about 1 m thick. To achieve the high solid angle coverage, the hadron calorimeter was constructed in three sections: the barrel, the endcap and the poletip. The main difference between these sections was in the number of layers of detectors in iron. Most hadronic interactions were initiated in the 2.2 interaction lengths of material before the hadron calorimeter (especially in the lead-glass calorimeter), so the total hadronic energy was determined by combining signals from both the electromagnetic and hadron calorimeters. The energy resolution was $\sigma_E/E \simeq 120\%/\sqrt{\mathrm{E}}$ for all the calorimeter.

### 5.1.5 Muon Detector

The muon detector was a system of large-area drift chambers constructed as a barrel and two endcaps. It covered the iron yoke almost completely. 93% of the $4\pi$

solid angle was covered by at least one layer of detector. The amount of material that a particle had to traverse before reaching the muon detector exceeded the equivalent of 1.4 m of iron (over 7 interaction lengths for pions). This reduced the probability of a pion not interacting, thus faking a muon, to less than 0.001. The efficiency for detecting isolated muons above 3 GeV was essentially 100%.

### 5.1.6 The OPAL Forward Detectors

These detectors were essential to the present analysis. They were originally used to measure the luminosity of LEP by detecting small-angle Bhabha scattering events, but also to measure after corrections the energy of hadrons from photon–photon interactions. The forward region consisted of the forward detector system and, from 1993 onwards, the silicon-tungsten calorimeter. The outer physical edge of the forward calorimeter was 165 mrad before 1993 and 154 mrad from 1993 onwards.

#### The Forward Detector

Before the SW detector was installed in 1993, there was a clean acceptance for particles from the intersection region between 47 and 120 mrad from the beam line with the only obstructions being the beam pipe and 2 mm of aluminium from the central detector pressure vessel. The forward detector (FD) consisted of an array of devices, listed below, whose primary objective was to detect low angle Bhabha scattering events as a way of determining the LEP luminosity for the normalization of measured reaction rates from decays. FD calorimeter represented for electro-magnetic showers 23 radiation lengths and are well measured, but only just over one interaction length for hadronic showers, for e.g. a pion of 4 GeV the shower maximum lied at the back edge of the detector. The only way to distinguish a $\pi$ from a $\gamma$ was to use the energy fraction deposited in the presampler. In hadronic showers only very little or no energy was contained in the presampler, as the showers tended to develop later. After the separation a parametrised correction was applied to the FD cluster energies [34].

To distinguish between pions and gammas from $\pi^0$s a cut was made on the ratio of the Presampler to Total cluster energy. $\mathrm{E}_{Pre}/\mathrm{E}_{FD} < 0.15$ selects 60% of $\pi$ and only 10% of $\gamma$, while 90% of $\gamma$ and 40% of $\pi$ lie above $\mathrm{E}_{Pre}/\mathrm{E}_{FD} > 0.15$. A parametrised correction could be applied to the FD cluster energies

$$E_\gamma = \frac{E_{FD}}{0.9 + 0.01 * E_{FD}} \quad ; \quad E_{FD} < 10\ GeV\ .and.\ E_{Pre}/E_{FD} > 0.15$$

with $\sigma(E_\gamma)/E = 50\%/\sqrt{E}$ and

$$E_\pi = \frac{E_{FD}}{0.5 + 0.016 * E_{FD}} \quad ; \quad E_{FD} < 30\ GeV\ .and.\ E_{Pre}/E_{FD} < 0.15$$

with $\sigma(E_\pi)/E = 90\%/\sqrt{E}$.

### The Silicon Tungsten Detector

The silicon-tungsten (SW) detector consisted of two cylindrical smallangle calorimeters encircling the beampipe at ±2389 mm in z from the interaction point. They had an angular acceptance of 25 mrad to 59 mrad. Each calorimeter was built up from 19 layers of silicon sampling wafers and 18 layers of tungsten, corresponding to a total of 22 radiation lengths. The radial position resolution on electron showers was approximately 10 $\mu$m and the energy resolution $\sigma_E/\mathrm{E} \simeq 28\%/\sqrt{\mathrm{E}}$.

The SW detector had no presampler, the variable called 'cluster type' which was an identification based on the energy of the cluster, was used for a global correction of the total measured SW energy [33].

The cluster type was an identification based on the energy of the cluster. It was equal to 1 for about 100% of the photons, of the electromagnetic cluster, whereas $\approx$ 50% of the clusters from pions had type 1 and the rest had type 4, which stands for unidentified blob. The cluster type value 2 meaned track, The value 3 corresponded to a hadronic cluster.

The total measured SW energy $E_{\mathrm{SW}}$ was split into two terms: the total energy $E_{\mathrm{SW},1}$ coming from clusters of type 1 and the total energy $E_{\mathrm{SW},4}$ from unidentified blobs (type 4)

$$E_{\mathrm{SW}} = \sum_{clustertype=1} E(cluster) + \sum_{clustertype=4} E(cluster) \quad = E_{\mathrm{SW},1} + E_{\mathrm{SW},4} \tag{5.2}$$

The idea was to attribute one part of $E_{\mathrm{SW},1}$ to the photons. This part was not corrected. The other part as well as $E_{\mathrm{SW},4}$ was considered as pion energy and was therefore corrected. According to the PYTHIA Monte Carlo generator the average number of photons and pions per event in the SW angular region was 1.4 and 1.24 respectively. Assuming all photon clusters but only half of the pion clusters were type one, the resulting part of $E_{SW,1}$ coming from the photons was on the average $\approx$ 69.3%.

To obtain the corrected SW energy $E_{\mathrm{SW,c}}$ the following three cases had to be distinguished, depending on whether $E_{\mathrm{SW},1}$ and $E_{\mathrm{SW},4}$ were greater or less then 1 GeV (this lower cut was necessary to suppress detector noise):

1. $E_{\mathrm{SW},1}$ >1 GeV and $E_{\mathrm{SW},4}$ <1 GeV

$$E_{\mathrm{SW,c}} = 0.693 E_{\mathrm{SW},1} + 5\ln(1.238 E_{\mathrm{SW},1} + 2) \tag{5.3}$$

2. $E_{\mathrm{SW},1} > 1$ GeV and $E_{\mathrm{SW},4} > 1$ GeV

$$E_{\mathrm{SW,c}} = 0.693 E_{\mathrm{SW},1} + 5\ln(1.238 E_{\mathrm{SW},1} + 2) + 5\ln(1.238 E_{\mathrm{SW},4} + 2) \tag{5.4}$$

3. $E_{\mathrm{SW},1} < 1$ GeV and $E_{\mathrm{SW},4} > 1$ GeV

$$E_{\mathrm{SW,c}} = 1.5 E_{\mathrm{SW},4} + 10 \tag{5.5}$$

### 5.1.7 Detector Simulation

The OPAL detector was simulated using a Monte Carlo program GOPAL [36] which used the CERN GEANT3 simulation package in the OPAL environment. The GEANT package provided the framework to define the geometrical parameters of the OPAL detector and to simulate interactions by tracking particles through the detector, including the necessary physics processes like scattering and decays. The GEANT package relied on standard physics simulation techniques and was developed and tested by many experiments.

When a particle traversed the sensitive region of a detector, the raw signals of the detector were generated. The tracking is completed by storing the position and momentum of each particle at tracking time. The interaction of each particle wss simulated step-by-step along its path. Such interactions with the material include energy loss, multiple scattering, bremsstrahlung, decay in flight and nuclear interactions.

# Chapter 6

# Event Selection

The aim of the event selection is to obtain a sample of untagged two-photon events that has little contamination of other type of events. This chapter will describe how the collection of $e^+e^- \rightarrow \gamma\gamma$ events for this analysis were obtained from the huge amount of raw data. The selection was done in two stages: at first every working group created their own set of files using general preselection; then the final selections were applied. In my case the final cuts were calculated by using the signal and background MC samples with the priority of keeping the total uncertainty in the highest-$p_T$ bin as low as possible, despite the high correction factor from the signal MC and the large statistical uncertainty. The quality cuts of the final selection were determined by comparison of the sum of all relevant MC and data.

I studied the production of charged hadrons using data taken at centre-of-mass energies from 183 to 209 GeV in $e^+e^-$ collisions, amounting to a total integrated luminosity of 612.831 $pb^{-1}$. The luminosity weighted average centre-of-mass energy was 195.8 GeV.

## 6.1 Signal and Background

All the data and MC files were transformed to PAW [38] ntuples [1] and moved and stored in CASTOR [39]. The Two-Photon Working Group created a list [40] that contained all the MCs and their structure, the group can use for any kind of analysis. I used them for the transverse momentum measurement. I needed to create new MC files only in some very special cases.

---

[1] ntuple is a set of events can be viewed as a table with each row corresponding to one event and each column corresponding to given variable

### 6.1.1 Structure of the ntuples

A detailed description helps us to understand the variables, the structure of the MC and the data files. There are event, trigger, subdetector, track and generator [2] level variables.

In the event block we identify the event with experiment-, run- and event number, and collect the event level variables like beam energy, energy in electromagnetic and hadron calorimeters, number of tracks, vertex position and trigger status.

In the SW block almost all the variables are available about the Silicon Tungsten Detector (see in Sect. 5.1.6. This was one of the most important detectors to measure the two-photon events boosted in the forward region. Since the SW detector was built to measure Bhabha events [33], the reconstructed hadronic energies was not expected to be very precise, thus, a correction of the hadronic SW energy was needed. The variable called 'cluster type' was used for a global correction of the total measured SW energy.

For the correction of the Forward Detector (see in Sect. 5.1.6) hadronic energy and the FD presampler was used to separate clusters produced by photons or pions. Two different corrections were applied [34]. The number of FD cluster and the preshower energy compose the FD block.

In the CT block the relevant parameters of the charged tracks extracted from the Central Detector (see in Sect. 5.1.1) are added. The CT processor [41] had two tasks in the reconstruction. The first was the pattern recognition, in which track segments from each component of the central detector were compared and associated to form a set of CT tracks. The second task was track fitting. Both tasks were done in $\mathrm{r} - \phi$ and in z. After they were completed, the track bank was filled (it's size depends on the number of fitted tracks). The CT block containe the weights (probabilities) that the track was an electron, muon, pion, kaon or proton; the track distance from the mean vertex position and a detailed parameter list about the hits.

The matching [42] (MT) is a package of codes, which provides the momentum of each particle observed by the Central Tracker, by the ECAL, by the HCAL and by the forward calorimeters. MT removed the double-counting of energy by using a matching algorithm. In the MT block the charge, momentum, energy of the neutral and charged particles are collected. ű

To measure the detector acceptance and resolution I used the event- and particle-level parameters of the MC block. The event-level parameters are the number of MC particles, the invariant mass of the hadronic final state, total energy and the $\mathrm{Q}^2$ of the electrons. The momentum, mass, charge, particle ID of the particles constitute

---

[2] In the MC simulations we know the particles themselves, not just their interaction with the detector, what we only have in the data files

the particle-level parameters. Even though this information is stored for all particles in the decay tree (not only the final state particles), I used only the final state ones.

### 6.1.2 MC generators

The MC generators PYTHIA 5.722 [43] and PHOJET 1.10 [44] was used to simulate photon-photon interactions. PYTHIA used the SaS-1D parametrisation [45] for the photon parton densities and PHOJET used the GRV parametrisation [46].

The MC generators PHOJET and PYTHIA were found to underestimate the cross-section (see in the previous publications [35], and Fig. 6.12) they showed a shape different from that in the data of the $p_{\mathrm{T}}$-distribution of charged hadrons. Thus the MC events were reweighted by a suitable $p_{\mathrm{T,max}}$-dependent[3] function to resemble the data. Both the original and the reweighted MC distributions were used in the analysis and any differences seen are included in the systematic uncertainty.

All relevant background processes were studied using MC generators. Multihadronic events ($\mathrm{e^+e^-} \rightarrow \mathrm{q\overline{q}}(\gamma)$) were simulated with PYTHIA 6.125. KORALZ 4.02 [47] was used to generate the process $\mathrm{e^+e^-} \rightarrow \tau^+\tau^-(\gamma)$ and VERMASEREN [48] to generate $\mathrm{e^+e^-} \rightarrow \mathrm{e^+e^-}\tau^+\tau^-$. Deep-inelastic $\mathrm{e}\gamma$ events were simulated with HERWIG 5.9 [49].

All signal and background MC samples were generated with full simulation of the OPAL detector [36]. They are analysed using the same reconstruction algorithms as the data. The number of generated MC events corresponds to ten times the data luminosity, with the exception of $\mathrm{e^+e^-} \rightarrow \mathrm{e^+e^-}\tau^+\tau^-$, for which three times the data luminosity was available.

## 6.2 Preselection

The main purpose of the preselection is to sort out the irrelevant background and therefore the resulting data set contains the relevant background and signal. For the Two-Photon Working Group the good status of the forward detectors, the identification of the scattered electrons, a minimum number of hits in the tracker and minimal energy deposit in the calorimeters were required. The most important criterias for two-photon events are the following: FF, SW, FD, EE are ready to use for electron finding; the minimum fraction of the beam energy for each electron canditate is 0.2; the minimum number of charged tracks is 2; the number of hits in CD is more than 20 or half of possible maximum; the minimal transverse momentum of the track is 0.1 Gev.

---

[3] $p_{\mathrm{T,max}}$ is the maximum transverse momentum of any track in the event

These selection cuts were very loose on the signal and the relevant background and were standard in the group, thus I didn't see a reason to change them. All the MC files we used were stored after the preselection, I used only in some cases the generators to create new sets without any preselections.

## 6.3 Data preparation

The selection cuts were not directly applied on the preselected ntuples, further preparation were needed. I used additonal corrections and calculation on the ntuples variable. The FORTRAN programming language was used for data analysis.

In a steering file I added the usual parameters for a run, like input files, output files, conditions and cuts I wanted to change only in this interface file and not in the code.

In the first step I collected all the important parameters I wanted to work with from an event. Two arrays were created, one for the detector-level parameters, the other for the generator-level parameters.

The array with the detector-level parameters mainly came from the input ntuples, but some were calculated locally from them. Here I calculated the new SW energy based on the calibration of the detector, which was built to measure Bhabha events and therefore a correction for the hadronic energy was needed [33]. Correction was made also for FD hadronic energy based on its preshower energy. No correction was available for hadron energy measured with FF, these tracks were excluded.

Not only event-level parameters, like corrected total energy, corrected total invariant mass, total energy measured with SW, FD, ECAL, HCAL, missing transverse energy, number of charged particles from MT, pseudorapidity, were added to the detector-level array, but, in an included array, the parameters of the final state tracks. In this array the momentum, energy, charge, origin of the tracks, distance from the mean vertex position and number of hits in CT were stored.

The second array contained the generator-level parameters in the case of MC files. Here I looped over MC tree particles, found the final state particle to calculate the momentum, energy, missing transverse energy, invariant mass. No correction was needed for the particles.

## 6.4 Selection of the untagged Two-Photon Events

In the selection subroutine only event-level parameters from the measurement and from the (fully reconstructed) MCs were used. A selection variable, whose each bit represented one selection, was used. The value of the bits was 1 if the selection failed and 0 otherwise. If any bit of the variable was 1, the event was unselected. In this way I not only selected the events, but was able to study the effect of different cuts. On Figs. 6.1 to **??** the number of events were given without applying the corresponding selection cut.

Two-photon events were selected with the following set of cuts:

- At least six tracks were required in the tracking chambers (Fig. 6.1). Cutting on the number of tracks removed background from $e^+e^- \to Z^0 \to \tau^+\tau^-$ and $e^+e^- \to \gamma\gamma \to \tau^+\tau^-$ events having typicaly less than 6 tracks.

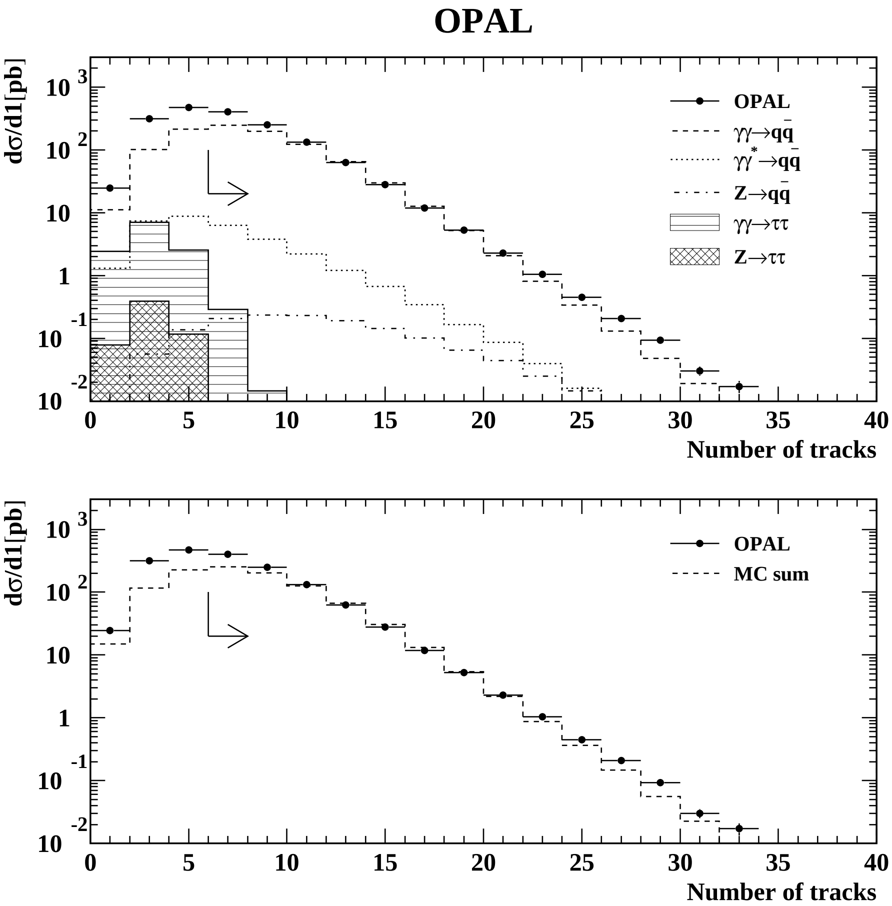

**Figure 6.1.** Number of tracks of the events using all the selection cuts listed below except the cut on the charged tracks

- The sum of all energy deposits in the ECAL and the HCAL was required to be less than 50 GeV (Fig. 6.2) to remove background from hadronic Z decays in events with a radiative return to the $Z^0$ peak.

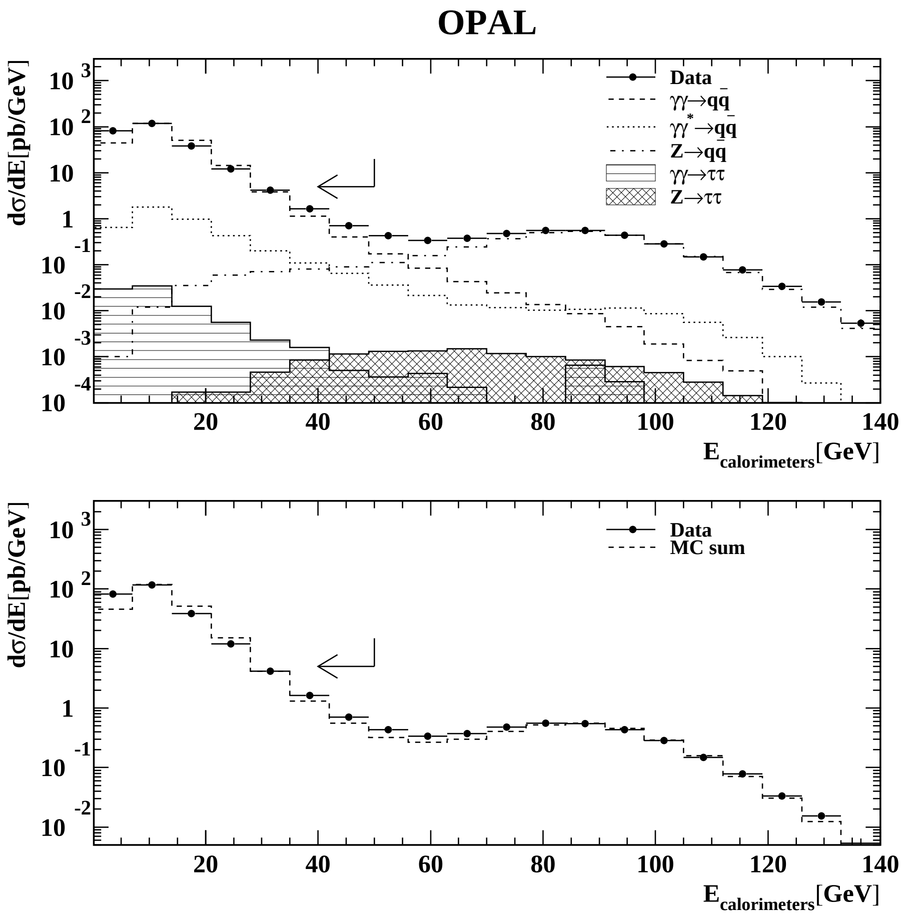

**Figure 6.2.** Energy deposit in the ECAL and HCAL calorimeters using all the selection cuts except the cut on the calorimeters energy

In the Fig. 6.2 I used all the selection cuts except the cut on energy deposit in the ECAL and the HCAL, e.g. the cut on number of tracks that removes almost all of the $e^+e^- \rightarrow Z^0 \rightarrow \tau^+\tau^-$ and $e^+e^- \rightarrow \gamma\gamma \rightarrow \tau^+\tau^-$ backgrounds. The two main backgrounds are the hadronic Z decays and the single-tag two-photon events, where one beam electron was identified by the detectors in the forward region.

As mentioned above, the selection cuts were calculated by using the signal and background MC samples considering the highest bin in transverse momentum to keep there the total uncertainty as low as possible. The uncertainty increases if the correction factor is too high, if I cut out too many events with high transverse momentum tracks. The energy deposit increased if the event contains track(s) with high transverse momentum ($p_T$>8 GeV), but this cut was still valid for these events also (Fig. 6.3).

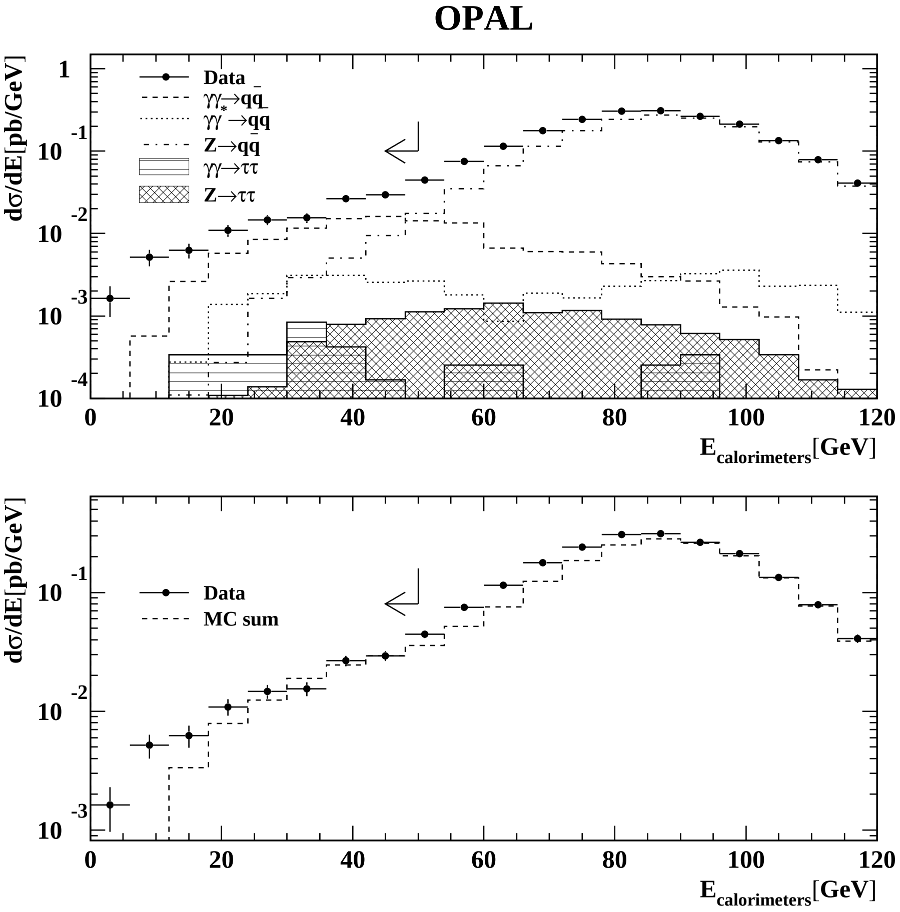

**Figure 6.3.** Energy deposit in the ECAL and HCAL calorimeters by the events with at least one high transverse momentum track ($p_T$>8 GeV)

- To reject events with tagged electrons in the FD or SW, the total energy sum measured in the FD and SW had to be less than 60 GeV (Fig. 6.4).

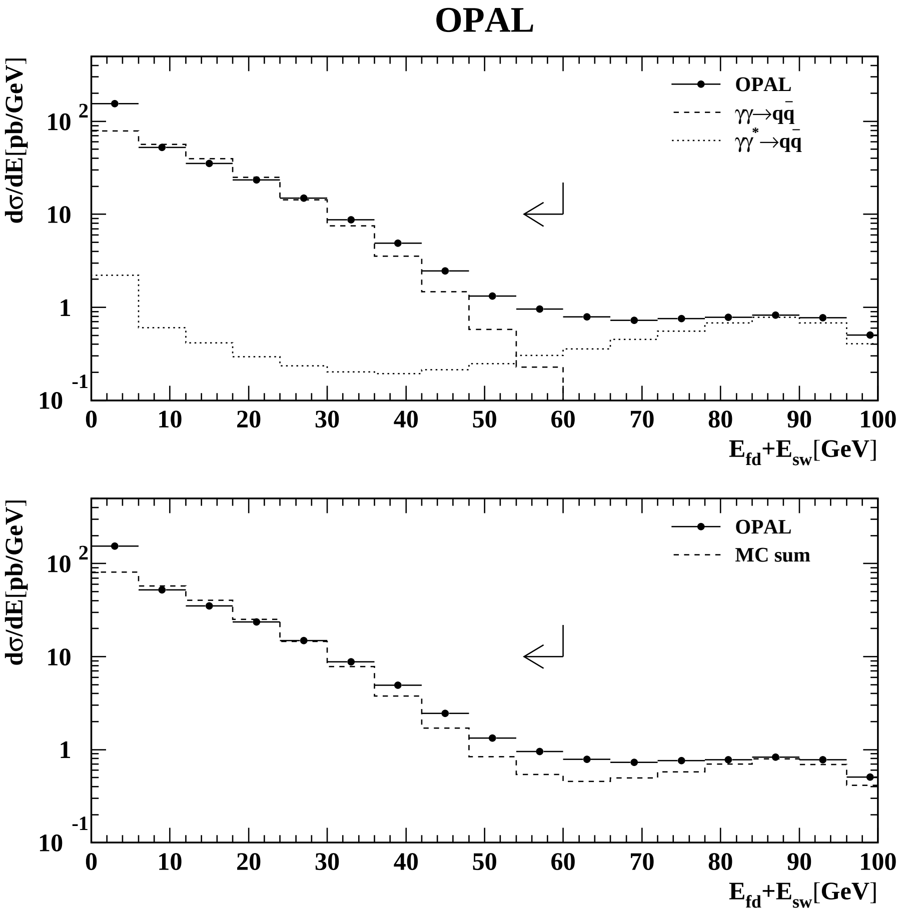

**Figure 6.4.** FD and SW energy deposit using all the selection cuts except the cut on the energy deposit in the forward region

- The background due to beam-gas or beam-wall interactions is reduced by requiring the radial distance of the primary vertex from the beam axis to be less than 2 cm.

- and the distance from the nominal vertex position along the $z$ direction had to be less than 3 cm.

- The visible invariant hadronic mass calculated from the position and the energy of the clusters measured in the ECAL had to be greater than 3 GeV.
- The missing transverse momentum of the event measured in the ECAL and the FD had to be less than 8 GeV.
- Any track was required to have a minimum transverse momentum of 120 MeV with respect to the $z$ axis and at least 40 hits in the central jet chamber. The number of measured hits in the jet chamber had to be more than half of the number of geometrical possible hits given the track direction. The radial distance of nearest approach of the track to the primary vertex had to be less than 0.15 cm, see in Sect. 6.4.1.

### 6.4.1 Impact parameter cut

The impact parameter $d_0$ of a track is defined as the distance of closest approach of the track to the interaction vertex (determined by the event reconstruction). The two projections of the track, in the transverse plane and along the beam direction, are usually considered separately, here I took the absolute value of the impact parameter into consideration.

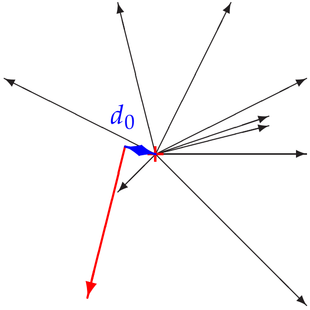

Using all selection cuts, except this one (this had not been used for untagged two-photon analysis before) I plotted the energy deposit in HCAL and ECAL for the events where there is at least one track with transverse momentum between 8 and 15 GeV (Fig. 6.5). The cut on calorimeter energy was not used for this plot (see in Sect. 6.4).

I realized that there was a peak in the $5 < E_{\text{calorimeters}} < 20$ GeV energy region for data and signal MC also. If there is at least one track with such a high transverse momentum it was also expected to have larger contribution in the calorimeters or at least not a peak at low energy but a slowly increasing distribution from low to high energy. The calorimeters were the most reliable part of the detector, it showed us, that these events, around 10 GeV, had no high transverse momentum (between 8 and 15 GeV) track(s).

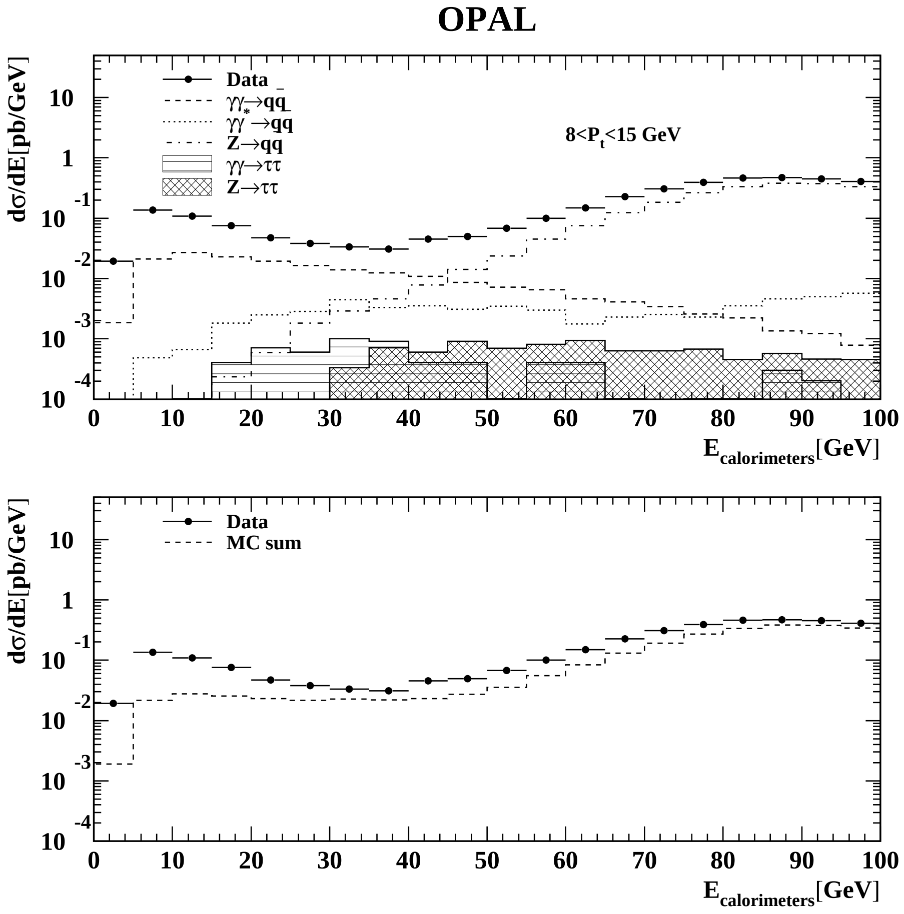

**Figure 6.5.** Energy deposit in the ECAL and HCAL calorimeters. using all the selection cuts except the cut on the calorimeter energy and the cut on the impact parameter. Only the events with at least one track with transverse momentum between 8 and 15 GeV.

The same plot (Fig. 6.6) was created for the events where there is at least one track with transverse momentum between 15 and 25 GeV. It was known that the signal MC underestimated the cross-section at low energy, since it was tuned with the previous results, but this peak-like behavior at low calorimeter energy needed to study.

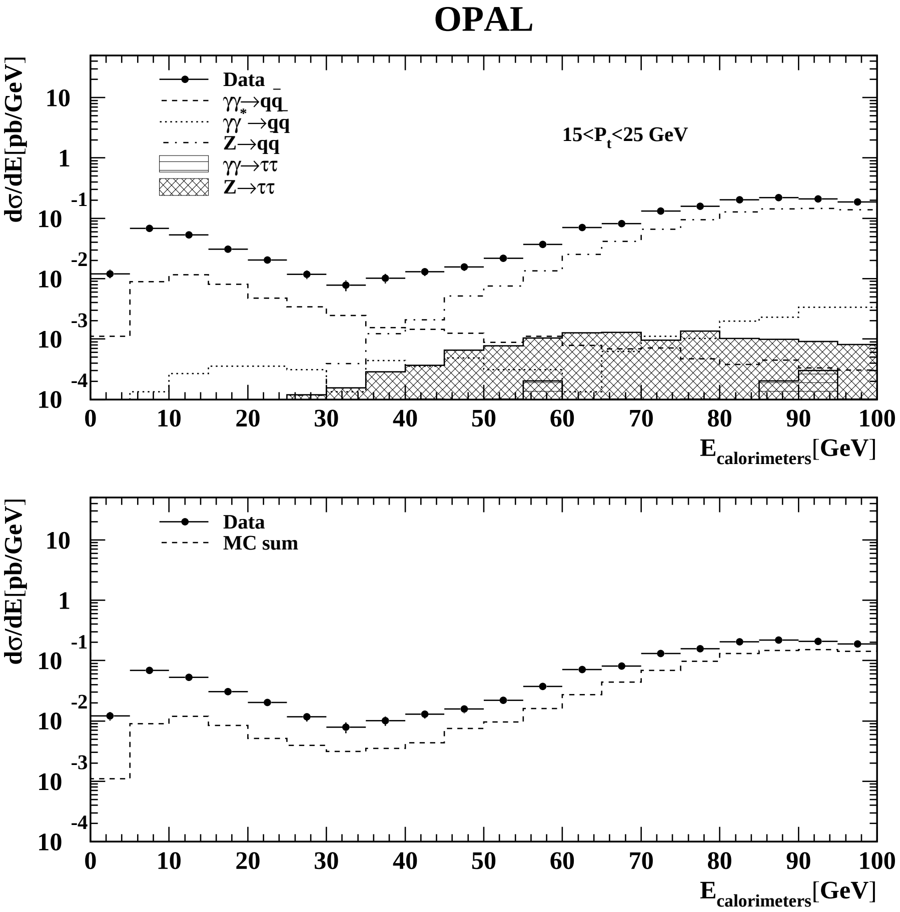

**Figure 6.6.** Energy deposit in the ECAL and HCAL calorimeters using all the selection cuts except the cut on the calorimeter energy and the cut on the impact parameter. Only the events with at least one track with transverse momentum between 15 and 25 GeV

These (on (Fig. 6.6)) were events with a very high $p_T$ track, so the peak on the calorimeter energy around 10 GeV had to be a track reconstruction issue. After I regenerated some signal MC samples and data, and all the possible track information added to the ntuple, in these new ntuples the momentum and also the uncertainty of the momentum reconstruction was known from the tracking algorithm. Concentrating on the events that contain at least one high transverse momentum track, I checked whether the particle at the hadron-level appears with the same kinematics as at the detector-level in the signal MC. I paired all the tracks and particle at the detector- and hadron-level by the direction of the momentum (within a small cone). The relative uncertainty on the momentum reconstruction $|\Delta p/p|$ is shown in Fig. 6.7(b) for the tracks (detector-level 8 GeV<$p_T$<15 GeV) where the transverse momentum in detector level is at least with 50% more than the $p_T$ in hadron level. The relative uncertainty is very large for these tracks. In Fig. 6.7(a) is shown the $|\Delta p/p|$ of the tracks where the differences between the $p_T$ in hadron and detector level smaller than 50%. This distribution is the expected resolution of the jet chamber (eq. 5.1).

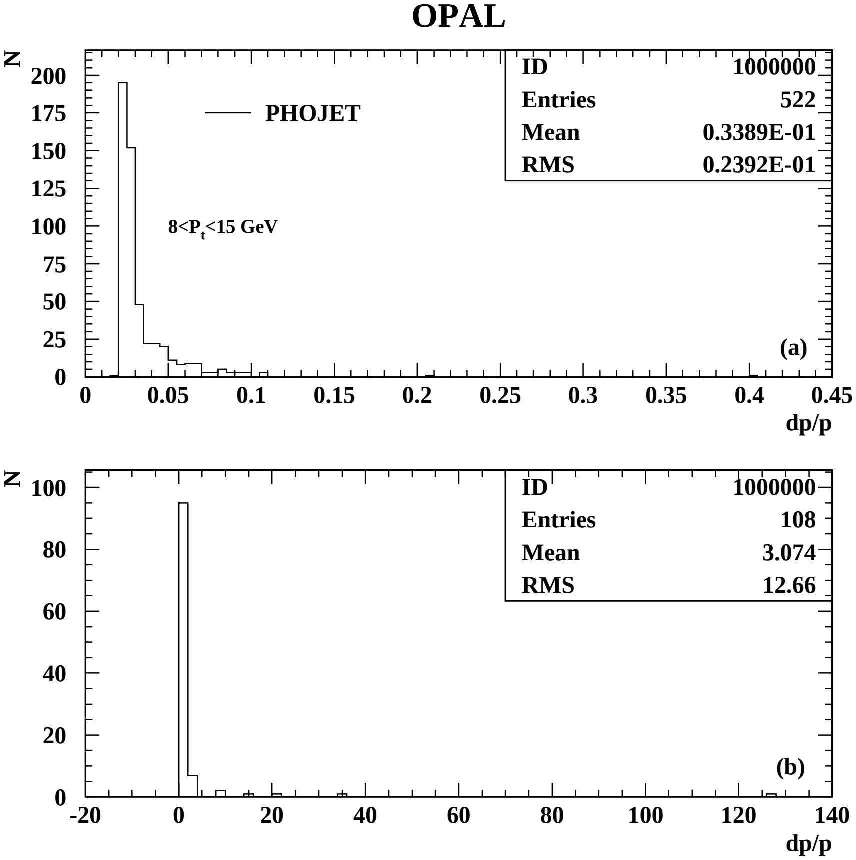

**Figure 6.7.** Relative uncertainty on momentum reconstruction for the tracks with transverse momentum between 8 GeV and 15 GeV, where track-$p_T$ is smaller than 1.5 times of the hadron-$p_T$(a), and where it's larger (b)

I could get rid of about 80% of the tracks with large uncertainty on momentum reconstruction by cutting at 15% relative error see the entries in Fig. 6.7(b) and Fig. 6.8(b), 108 → 23.

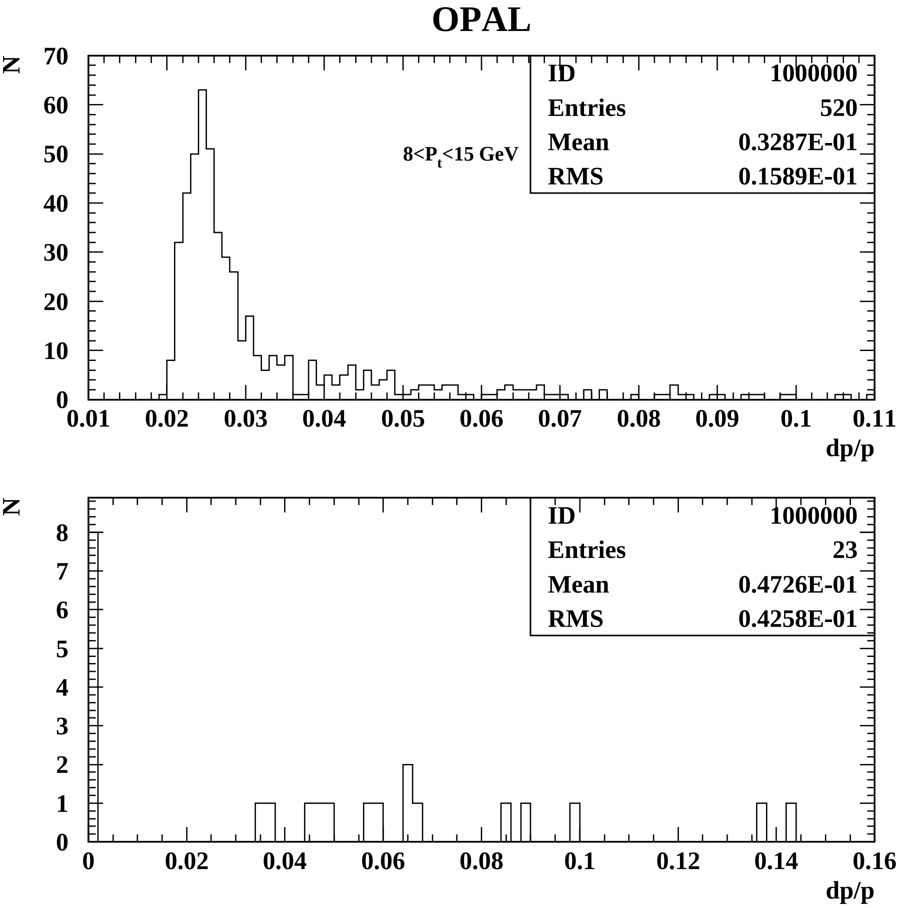

**Figure 6.8.** Relative uncertainty on momentum reconstruction for the tracks with transverse momentum between 8 GeV and 15 GeV where the relative error on reconstruction is small, $|\Delta p/p|$<0.15

The relative uncertainty on the momentum reconstruction $|\Delta p/p|$ was used to identified the high transverse momentum hadrons without tracks (at all, or with similar transverse momentum). It was found with $|\Delta p/p| < 0.15$ criteria 80%-90% of the misreconstructed tracks were excluded.

Instead of the cut on the relative uncertainty on momentum reconstruction the cut on impact parameter was used by many other OPAL groups (and it was available in every data and MC sample) which correlates well with the uncertainty on momentum reconstruction for MC (Fig. 6.9) and data (Fig. 6.10).

If the $|\Delta p/p|$<15%(Fig. 6.9(a) and Fig. 6.10(a)), the impact parameter is close to the 0 and for $|\Delta p/p|$>15% (Fig. 6.9(b) and Fig. 6.10(b)) we got a flat distribution in a much wider range around 0.

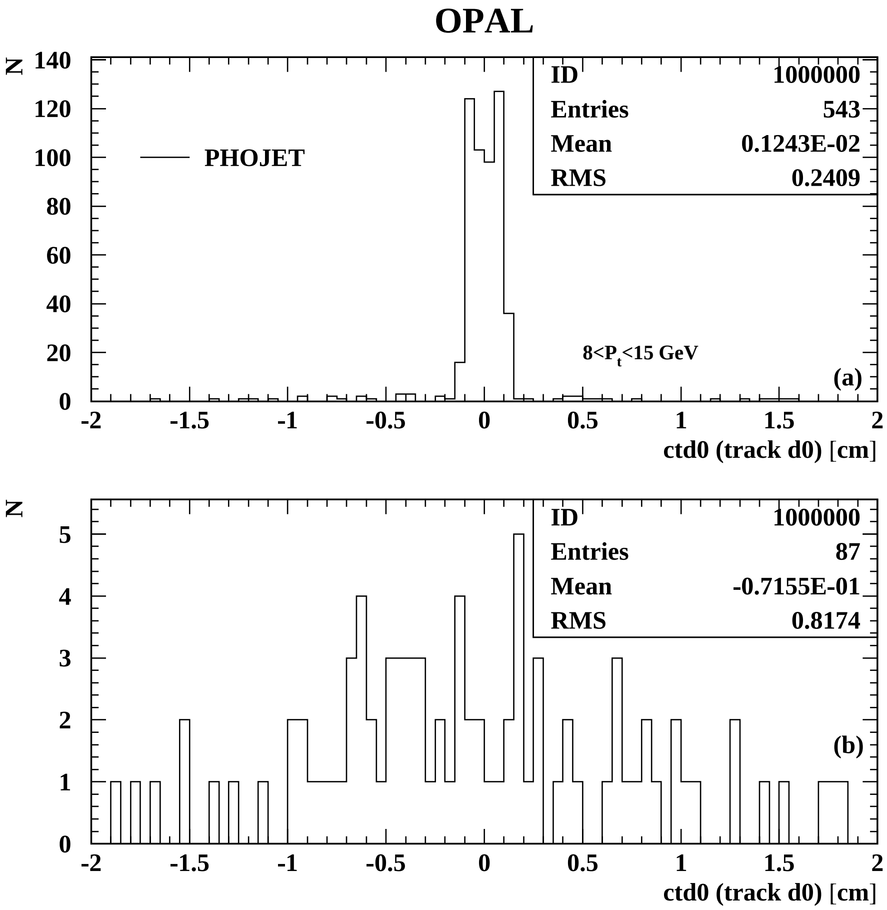

**Figure 6.9.** The impact parameter of the tracks depends on the quality of reconstruction (MC) if $|\Delta p/p|$<15% (a) and $|\Delta p/p|$>15% (b)

Using a cut $|d0|$<0.15 cm in the MC I saved almost all of the tracks where $|\Delta p/p|$<15%, which means these tracks are well reconstructed. With this selection

I lost large fraction from the tracks where $|\Delta p/p|$>15%, which identified the misreconstructed ones.

In the data I couldn't compare detector and hadron level, here I used only the detector level information, the $|\Delta p/p|$ to see the impact parameter distribution. The $d0$ is close to the 0 for $|\Delta p/p|$<15% and has a wider distribution for $|\Delta p/p|$>15%.

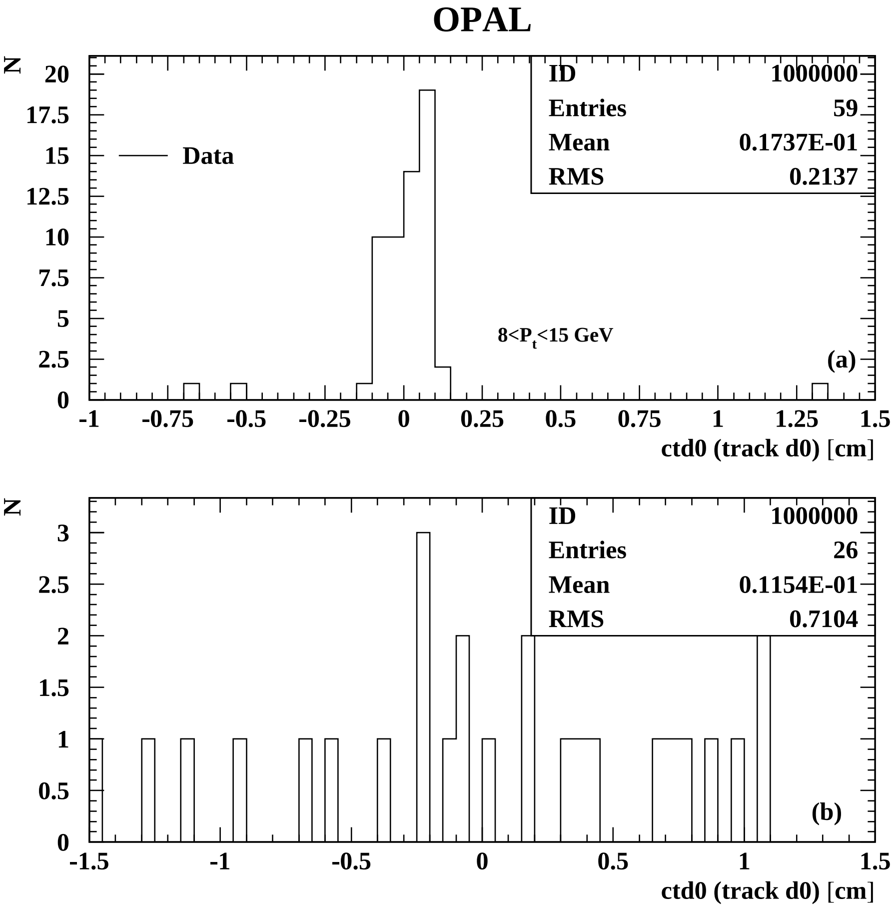

**Figure 6.10.** The impact parameter of the tracks depends on the quality of reconstruction (data) if $|\Delta p/p|$<15% (a) and $|\Delta p/p|$>15% (b)

I used the cut $|d0|$<0.15 cm for the analysis. The 25<$p_T$<45 GeV bin was the highest possible bin in my analysis, but I had to ignore because of this impact parameter study. After using this cut the energy deposit in the calorimeters:

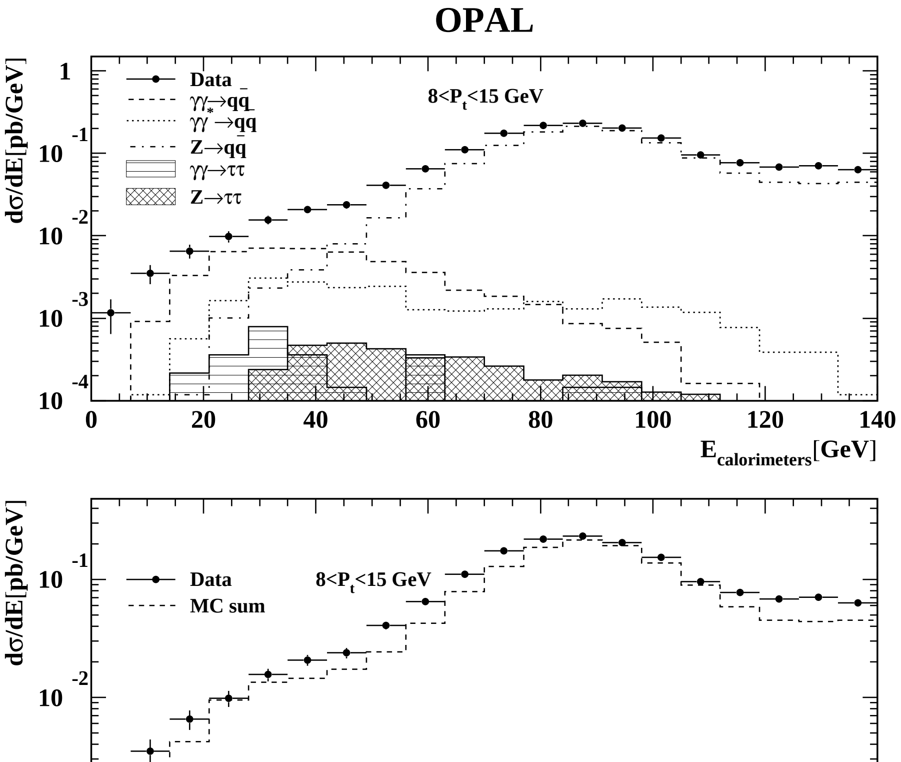

**Figure 6.11.** Energy deposit in the ECAL and HCAL calorimeters using all the selection cuts except the cut on the calorimeter energy. Only the events with at least one track with transverse momentum between 8 and 15 GeV with the $|d_0|$<0.15 cm cut on the tracks.

## 6.5 Comparing Data and Monte Carlo Samples

After all cuts, the data sample contained 1 144 035 events. At every event, with a loop over the MT block, histograms of the transverse momentum and the pseudorapidity of the tracks were filled and normalized with the bin width and luminosity (Fig. 6.12-Fig. 6.14). The main remaining background processes were multihadronic Z decays, $e^+e^- \longrightarrow e^+e^-\tau^+\tau^-$ and deep-inelastic $e\gamma$ scattering. Other background processes were found to be negligible. The distributions $d\sigma/dp_T$ and $d\sigma/d|\eta|$ were measured in four bins: $10<W<30$ GeV, $30<W<50$ GeV, $50<W<125$ GeV and $10<W<125$ GeV, very similar to the bins in the previous publication [35], where $W$ represents the hadronic invariant mass after correcting for detector effects (Fig. 6.12-Fig. 6.14).

As mentioned in Sect. 6.1, PHOJET and PYTHIA underestimated the cross-section at large transverse momentum, which could clearly be seen in the widest hadronic invariant mass bin (Fig. 6.12(d)). The MC events were reweighted by a suitable $p_T$-dependent function to resemble the data. The result of this reweighting compared to the data for every hadronic invariant mass bin is swhown in (Fig. 6.13). This reweighting had only a second order effects on the results, we used as a first hint for the next tune of the signal MC.

From the MC simulations it was estimated that after all cuts the total remaining background was below 2% overall, but increased to up to 50% at very high transverse momenta of the charged particles. Both the original and the reweighted MC distributions were used in the analysis and any differences seen were included in the systematic uncertainty. The differential cross-section was nearly independent of $|\eta|$ in the range measured as seen on (Fig. 6.14).

The data points in the figure indicate the bin centre. PYTHIA and PHOJET describe the shape of the distributions correctly for all regions of the phase space measured.

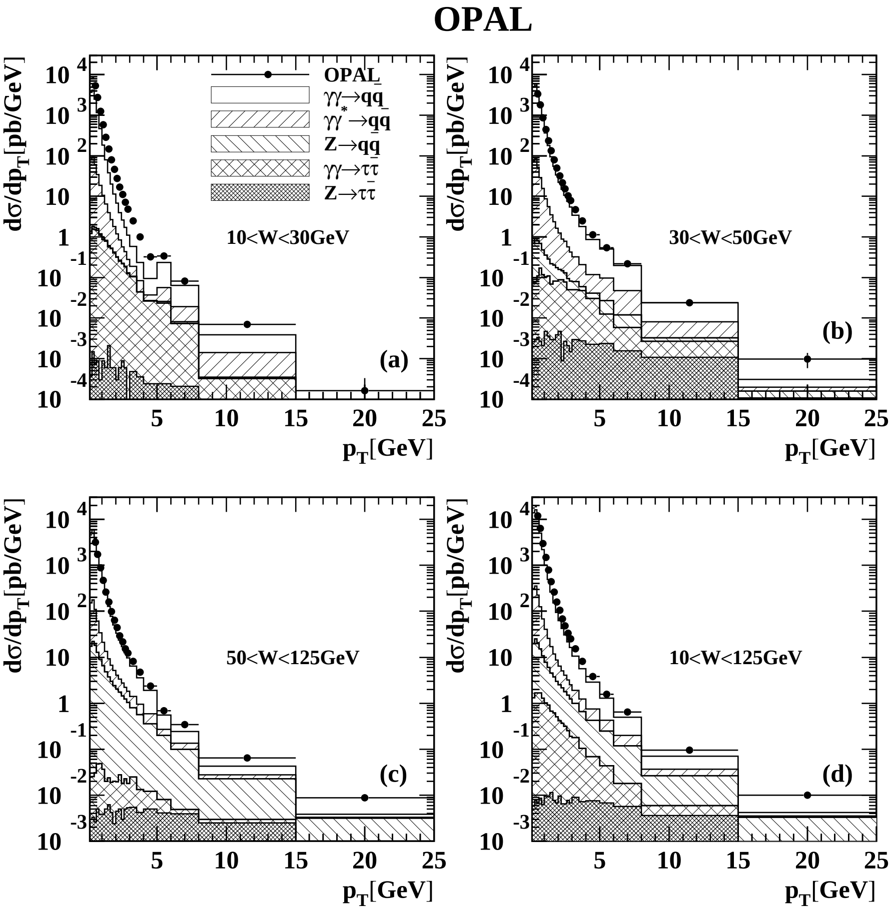

**Figure 6.12.** The $p_\mathrm{T}$ distributions for $|\eta| < 1.5$ in the different $W$ ranges. The error bars show the statistical and systematic uncertainties added in quadrature when larger than the marker, which indicates the bin centre.

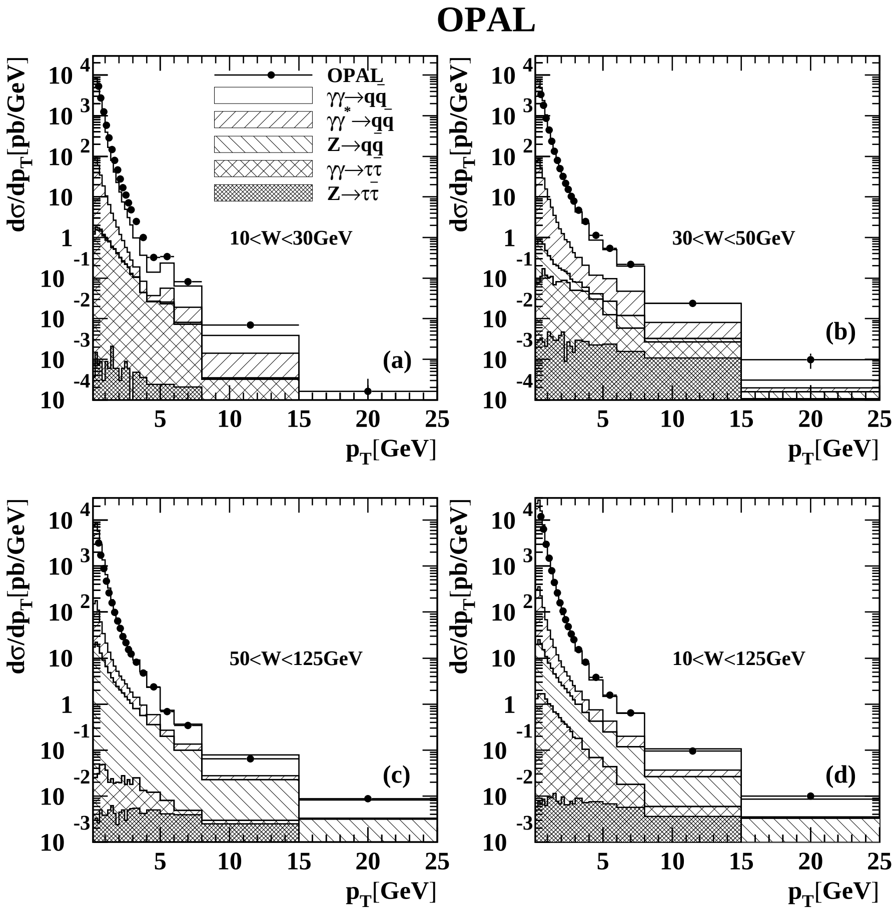

**Figure 6.13.** The $p_{\mathrm{T}}$ distributions with reweighted signal MC's for $|\eta| < 1.5$ in the different $W$ ranges

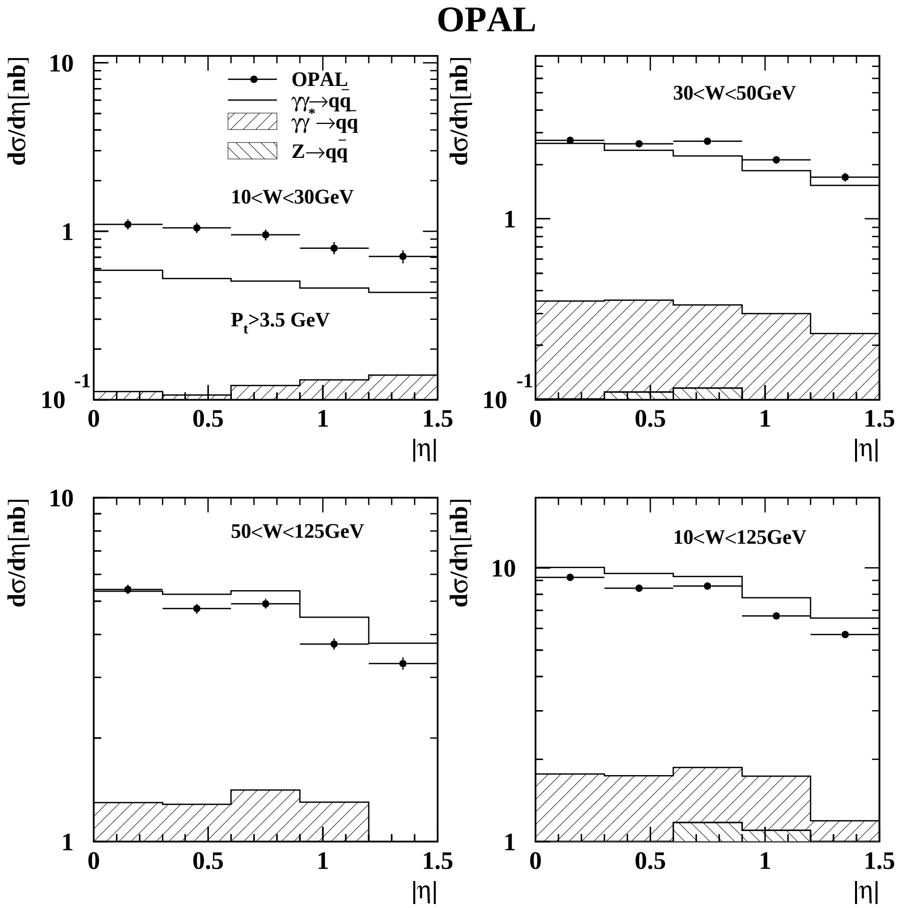

**Figure 6.14.** The $\eta$ distributions with reweighted signal MC's for $p_{\mathrm{T}}$>35 in the different $W$ ranges.

# Chapter 7

# Analysis

## 7.1 Unfolding

The classic problem in experimental physics is how to find the true distributions, knowing the experimental apparatus. With an ideal detector we could just obtain $\mathrm{d}\sigma/\mathrm{d}p_{\mathrm{T}}$ from a well defined histogram of $p_{\mathrm{T}}$, but a with real detecor this is influenced by the following effects:

- Limited acceptance: the probability to observe the event (for invariant mass binning) or a track (for cross-section measurement) is less than 1;

- Backgrounds: in spite of the selection cuts, depending on the kinematic region, some background events are indistinguishable from the signal events;

- Transformation: some of the particles are lost in the forward direction, therefore, $W_{\mathrm{gen}}$ (Eq. 4.6), the generated hadronic invariant mass, differs from the $W_{\mathrm{vis}}$ (Eq. 4.8), visible hadronic invariant mass;

- Resolution: the measured quantities are smeared due to the finite resolution of the detector.

The measured transverse momentum and pseudorapidity distributions of charged hadrons have to be corrected for the losses due to event and track selection cuts, the acceptance and the resolution of the detector. This is done using the MC samples which were processed by the full detector simulation and reconstruction chain. The data were corrected by multiplying the experimental distribution of the transverse momentum $p_{\mathrm{T}}$ or pseudorapidity $\eta$, with correction factors which were calculated as the bin-by-bin ratio of the generated and the reconstructed MC distributions:

$$\left(\frac{\mathrm{d}\sigma}{\mathrm{d}p_\mathrm{T}}\right)_\mathrm{corrected} = \frac{\left(\frac{\mathrm{d}\sigma}{\mathrm{d}p_\mathrm{T}}\right)^\mathrm{MC}_\mathrm{generated}}{\left(\frac{\mathrm{d}\sigma}{\mathrm{d}p_\mathrm{T}}\right)^\mathrm{MC}_\mathrm{reconstructed}} \left(\frac{\mathrm{d}\sigma}{\mathrm{d}p_\mathrm{T}}\right)_\mathrm{measured} . \tag{7.1}$$

$$\left(\frac{\mathrm{d}\sigma}{\mathrm{d}\eta}\right)_\mathrm{corrected} = \frac{\left(\frac{\mathrm{d}\sigma}{\mathrm{d}\eta}\right)^\mathrm{MC}_\mathrm{generated}}{\left(\frac{\mathrm{d}\sigma}{\mathrm{d}\eta}\right)^\mathrm{MC}_\mathrm{reconstructed}} \left(\frac{\mathrm{d}\sigma}{\mathrm{d}\eta}\right)_\mathrm{measured} . \tag{7.2}$$

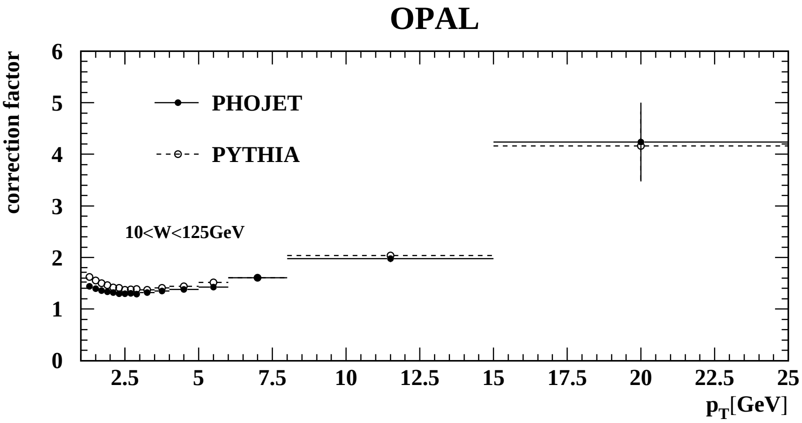

**Figure 7.1.** Correction factors in the widest W-bin for PHOJET and PYTHIA

Two signal MC generators were used in Two-Photon Working Group, PYTHIA and PHOJET (see Sect. 6.1.2), the ratio was calculated using both, and data was corrected with the mean.

The OPAl measurement and the MC samples were identical in structures in detector level. The backgrounds were subtracted bin-by-bin from the distributions before corrections for detector resolution and acceptance were applied

The following bin boundaries were used: 0.12, 0.28, 0.44, 0.6, 0.80, 1.0, 1.2, 1.4, 1.6, 1.8, 2.0, 2.2, 2.4, 2.6, 2.8, 3.0, 3.5, 4.0, 5.0, 6.0, 8.0, 15.0, 25.0 GeV for $p_\mathrm{T}$ and 0.0, 0.3, 0.6, 0.9, 1.2, 1.5 for $|\eta|$ according to the previous publications [35].

This method only yields reliable results if migration effects between bins, due to the finite resolution of the measurement, are small. The bins of the $p_\mathrm{T}$ and $|\eta|$ distributions were therefore chosen to be significantly larger than the resolution expected from the MC simulation.

In the signal MC the measured tracks (reconstructed on detector-level) and hadron-level generated particles were again paired, the $(p_{\mathrm{T,reconstructed}} - p_{\mathrm{T,generated}})/p_{\mathrm{T,generated}}$ are shown in Fig 7.2 for the bins from 1.0-1.2 GeV (upper left) to 8.0-15.0 GeV (lower right). The fractions of the relative bin width $(|p_{\mathrm{upperboundary}} - p_{\mathrm{lowerboundary}}|/p_{\mathrm{mean}}$ and deviation of the $(p_{\mathrm{T,reconstructed}} - p_{\mathrm{T,generated}})/p_{\mathrm{T,generated}}$ (added to the plot) is large at low $pT$ (1.0-1.2 GeV) and for the highest bins, that means the relative bin width is much larger than the relative error on reconstruction, the bin to bin migration was expected to be small. In the middle, between 2 and 3 GeV, where the the bin width is 0.2 GeV, it was smaller, but still acceptable.

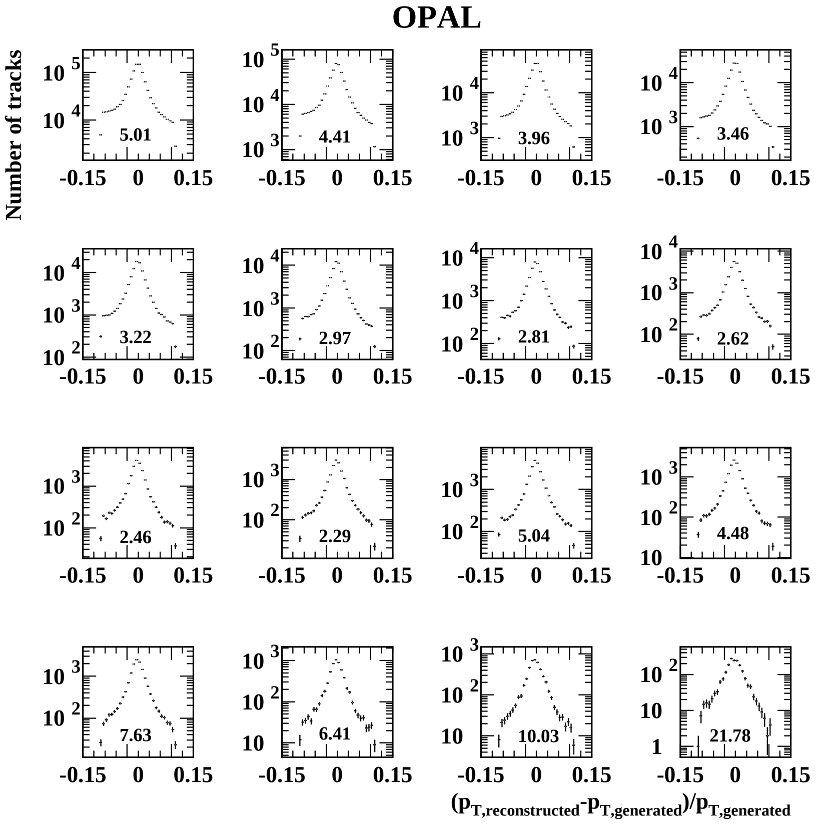

**Figure 7.2.** Relative size of the bins corresponding to the resolution in the bins is given on the plots for the $p_T$-bins from 1.0-1.2 GeV (upper left) to 8.0-15.0 GeV (lower right)

The visible invariant mass, $W_{\mathrm{vis}}$ (see Eq. 4.8), was determined from all tracks and calorimeter clusters, including the forward detectors and the silicon tungsten calorimeters, after applying a matching algorithm to avoid double counting of particle momenta [50].

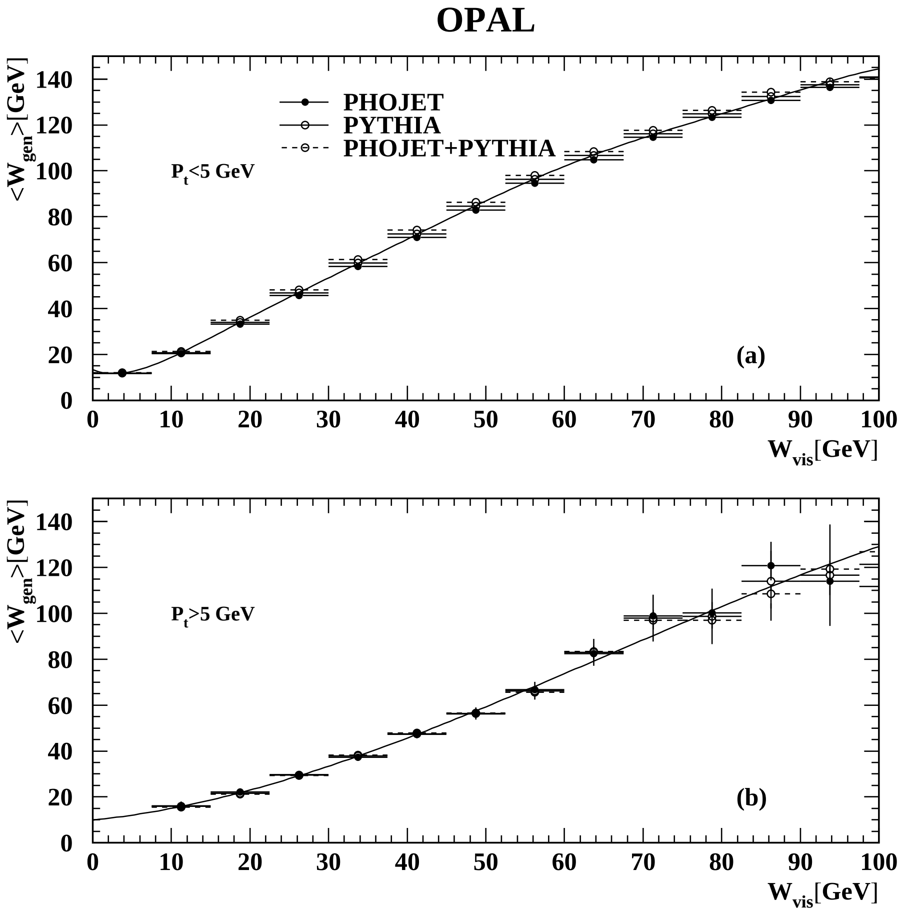

**Figure 7.3.** The correlation between the generated hadronic invariant mass $W_{\mathrm{gen}}$ and the visible hadronic invariant mass $W_{\mathrm{vis}}$ in two regions of $p_{\mathrm{T,max}}$, the maximum transverse momentum of any track in the event, for PHOJET and PYTHIA MC events. The vertical bars show the standard deviation on the mean in where larger than the marker size. The horizontal lines indicate the bin width. The polynomial fit determines the correction function for $W_{\mathrm{vis}}$.

In the signal MC samples the $W_{\mathrm{gen}}$ (see Eq. 4.6) was calculated. The ratio of $W_{\mathrm{gen}}$ and $W_{\mathrm{vis}}$ depended on the event kinematics, and was therefore determined separately in two distinct regions of phase space. The discriminating variable chosen for this purpose was $p_{\mathrm{T,max}}$, the highest transverse momentum of any track in the event. The visible hadronic invariant mass, $W_{\mathrm{vis}}$, and the generated hadronic invariant mass $W_{\mathrm{gen}}$ for events with $p_{\mathrm{T,max}}$ smaller and larger than 5 GeV are shown in Fig. 7.3(a) and (b). The polynomial fits superimpose on this plot are used as a correction function to calculate $W_{\mathrm{rec}} = W_{\mathrm{vis}} \times (W_{\mathrm{gen}}/W_{\mathrm{vis}})_{fitted}$ so that $\langle W_{\mathrm{gen}} \rangle / \langle W_{\mathrm{rec}} \rangle \approx 1$. In this case bin-to-bin migrations were minimised. These parameters was determined by using the average of PYTHIA and PHOJET. To facilitate comparisons to the results in [51], the ranges $W > 30$ GeV and $W > 50$ GeV were also considered.

In order to be able to use Eq. 7.1-7.2 for the detector correction in each bin of $W$, the bins in $W$ had to be larger than the experimental resolution.

## 7.2 Systematic uncertainties

The following sources of systematic uncertainties were investigated:

- Significant amounts of background needed to be subtracted from the data at large $p_T$, where the dominant source of background was multihadronic events ($e^+e^- \rightarrow q\bar{q}(\gamma)$). The amount of this background subtracted from the data was varied by ±10% to estimate the uncertainty associated to this procedure. The amount by which the background had to be varied was estimated from studying the MC description of the data in regions of the phase space where the background dominated. The effect on the measured cross-section was usually 1 % or less for low transverse momenta, increasing to up to 7 % at the high momenta measured.

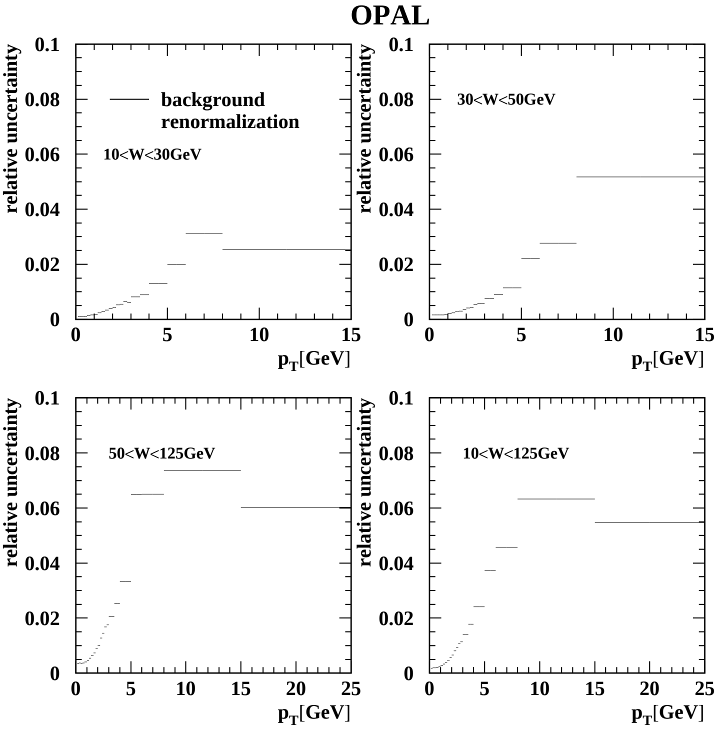

**Figure 7.4.** Relative systematic uncertainities - background reweight

- The selection criteria described in Section 6 were varied simultaneously both to be more restrictive and to allow more events into the analysis to exclude a strong dependence on the event selection. Selection criteria based on energy measurements were varied by 5% in the ECAL and HCAL, and by 10% in the FD and SW calorimeters. The number of tracks required was changed by ±1. The allowed radial distance of the tracks was varied by 5%. The uncertainty on the cross-section derived from all these variations was typically 1-9%.

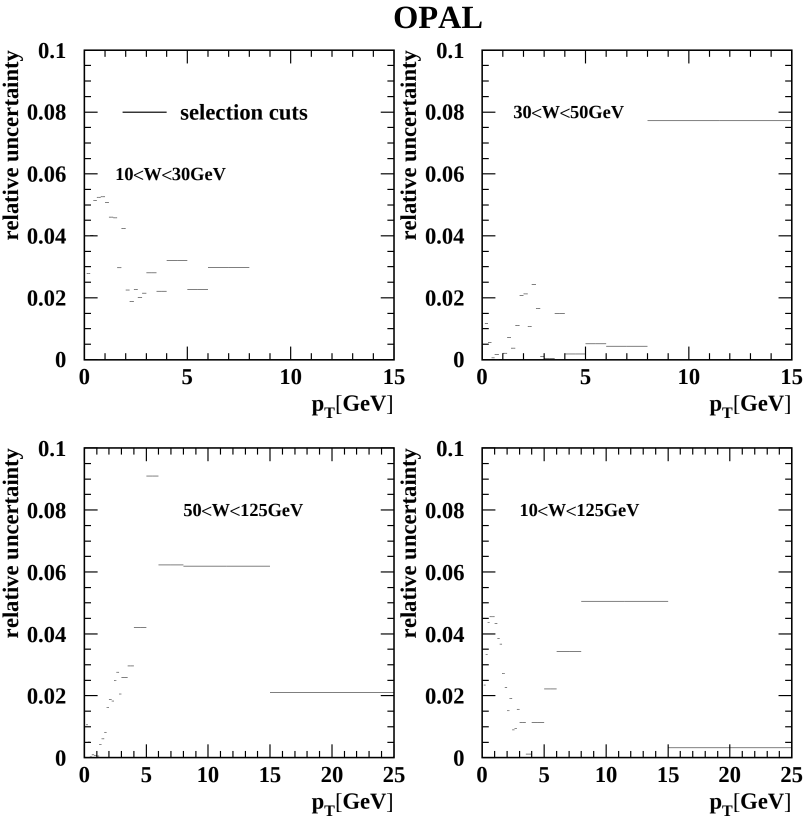

**Figure 7.5.** Relative systematic uncertainities - selection criterias

- Both PHOJET and PYTHIA were used to calculate the correction factors applied to the data. The resulting distributions are averaged and the difference between the two distributions is used to define the systematic uncertainty (see the difference in Fig 7.1. The distributions obtained from both programs were reweighted for a better description of the data. The difference between using the reweighted and the original MC distributions to calculate the correction factors were also included in the systematic uncertainty. The uncertainty derived from this study is below 10%.

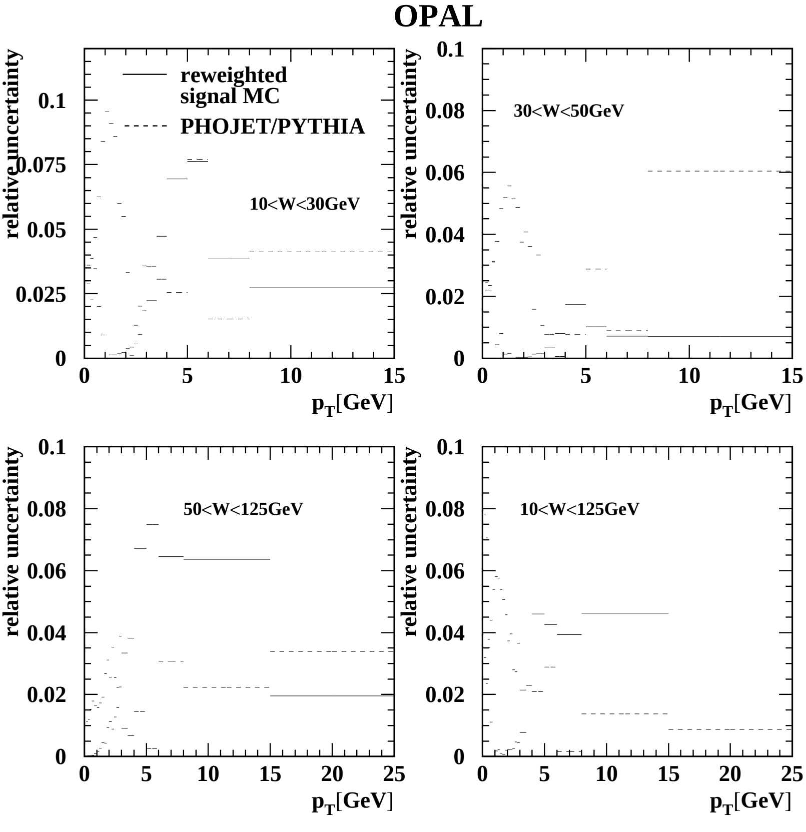

**Figure 7.6.** Relative systematic uncertainities - signal MC reweight and PHOJET-PYTHIA differences

- The systematic uncertainty due to the energy scale of the ECAL for the range of energies in this analysis was estimated by varying the reconstructed ECAL energy in the MC by ±3 % [52]. The cross-sections changed by up to 8% due to this variation.

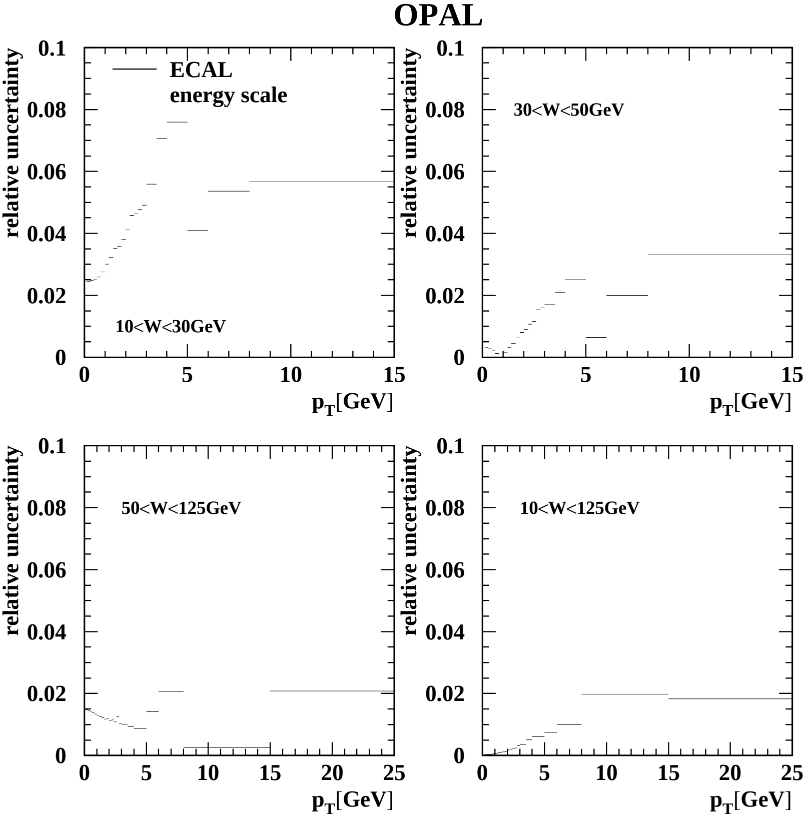

**Figure 7.7.** Relative systematic uncertainities - ECAL uncertainities

- Studying vertex and net charge distributions it was estimated that about 2% of the selected events were due to beam-gas or beam-wall interactions. This remaining background was treated as a systematic uncertainty of 2%.

Systematic uncertainties due to the modelling of the detector resolution for the measurement of tracks [35] and due to the luminosity measurement were found to be negligible. The total systematic uncertainty was obtained by adding all systematic uncertainties in quadrature.

# Chapter 8

# Results

The differential inclusive cross-sections $\mathrm{d}\sigma/\mathrm{d}p_{\mathrm{T}}$ for charged hadrons in four ranges of the hadronic invariant mass $W$ are shown in Fig. 8.1 and are given in Table 8.1, Table 8.2, Table 8.3 and Table 8.4, the details see in [56] and [57]. The cross-sections was calculated with bin-by-bin unfolding see details in Sect. 7.1. The data points in the figure indicate the bin centre. Both data and calculations are presented for quasi-real photons of virtualities $Q^2 < 4.5$ GeV$^2$, as described in Sect. 4.2.

Calculations in NLO QCD [27] are compared to the data. The cross-sections are calculated using the QCD partonic cross-sections in NLO for direct, single- and double-resolved processes. The hadronic cross-section is a convolution of the Weizsäcker-Williams effective photon distribution, the parton distribution functions and the fragmentation functions of [28]. The AFG-HO parametrisation of the parton densities of the photon [55] is used with $\Lambda^5_{\overline{MS}} = 221$ MeV. The renormalisation and factorisation scales in the calculation are set equal to $p_{\mathrm{T}}$. The cross-section calculation was repeated for the kinematic conditions of the present analysis. For the differential cross-section $\mathrm{d}\sigma/\mathrm{d}p_{\mathrm{T}}$ a minimum $p_{\mathrm{T}}$ of 1.5 GeV is required to ensure the validity of the perturbative QCD calculation. Even at $p_{\mathrm{T}} = 1.5$ GeV the cross-sections change by up to 80% when varying the renormalisation and factorisation scales by factors of two (see Sect 4.4 and Fig. 4.11). This uncertainty decreases rapidly to between 10% and 15% for $p_{\mathrm{T}} = 3.5$ GeV and above. The differential cross-section $\mathrm{d}\sigma/\mathrm{d}|\eta|$ is hence restricted to the region $p_{\mathrm{T}} > 3.5$ GeV to allow a meaningful comparison.

In Fig. 8.1 the NLO calculation lies significantly below the data for transverse momenta greater than about 10 GeV, which can be reached in the highest $W$ range only. The predictions of PHOJET and PYTHIA (not shown) at high $p_{\mathrm{T}}$ are similar to the NLO calculation.

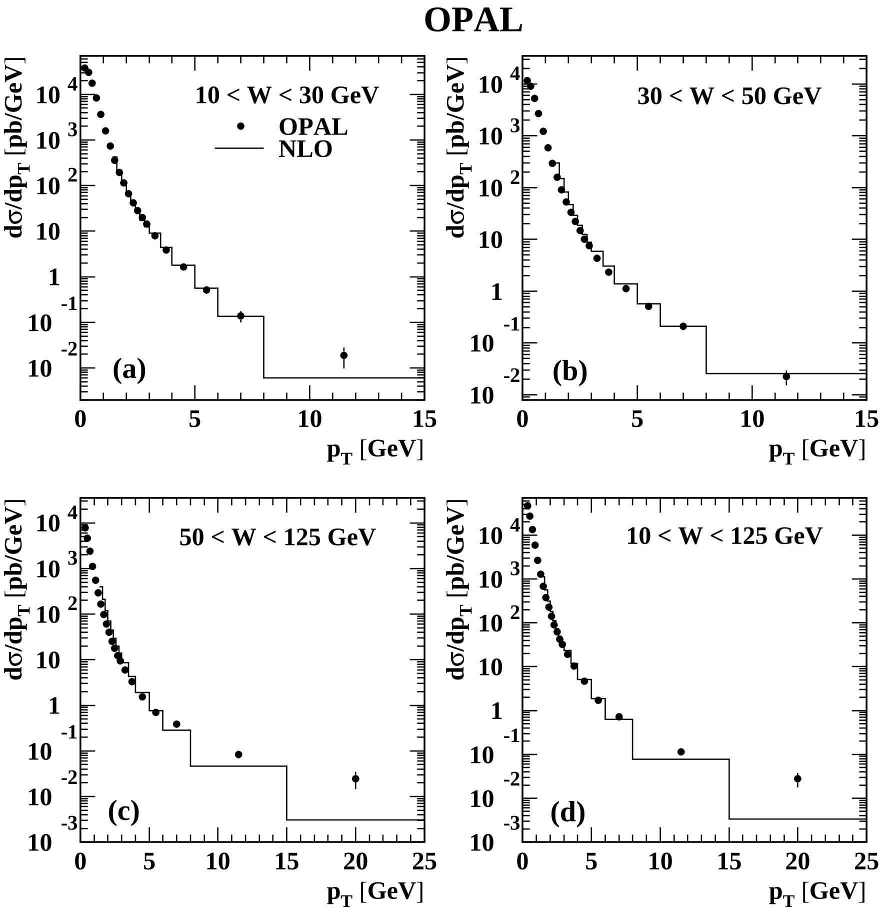

**Figure 8.1.** Differential inclusive charged hadron production cross-sections, $\mathrm{d}\sigma/\mathrm{d}p_{\mathrm{T}}$, for $|\eta| < 1.5$ in the $W$ ranges (a) $10 < W < 30$ GeV; (b) $30 < W < 50$ GeV; (c) $50 < W < 125$ GeV and (d) $10 < W < 125$ GeV. The error bars show the statistical and systematic uncertainties added in quadrature when larger than the marker, which indicates the bin centre. The data are compared to an NLO calculation.

The differential cross-section is nearly independent of $|\eta|$ in the range measured as can be seen in Fig. 8.2. The data points in the figure indicate the bin centre. The cross-section values are given in Table 8.5. The NLO calculation reproduces the data well within the uncertainties of the calculation. PYTHIA and PHOJET describe the shape of the distributions correctly for all regions of the phase space measured, but

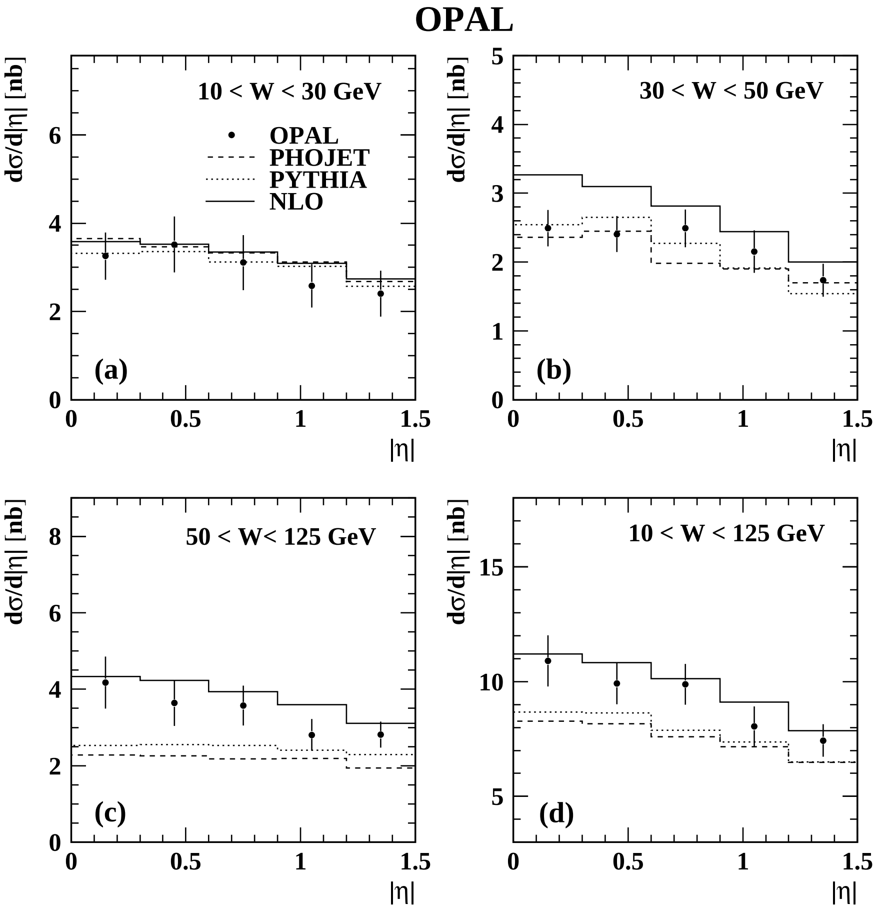

**Figure 8.2.** Differential inclusive charged hadron production cross-sections, $d\sigma/d|\eta|$, for $p_T >$ 3.5 GeV and in the different $W$ ranges.The data are compared to the PHOJET and PYTHIA models. The data are also compared to an NLO calculation. The error bars show the statistical and systematic uncertainties added in quadrature.

are below the data in normalisation for large values of $W$.

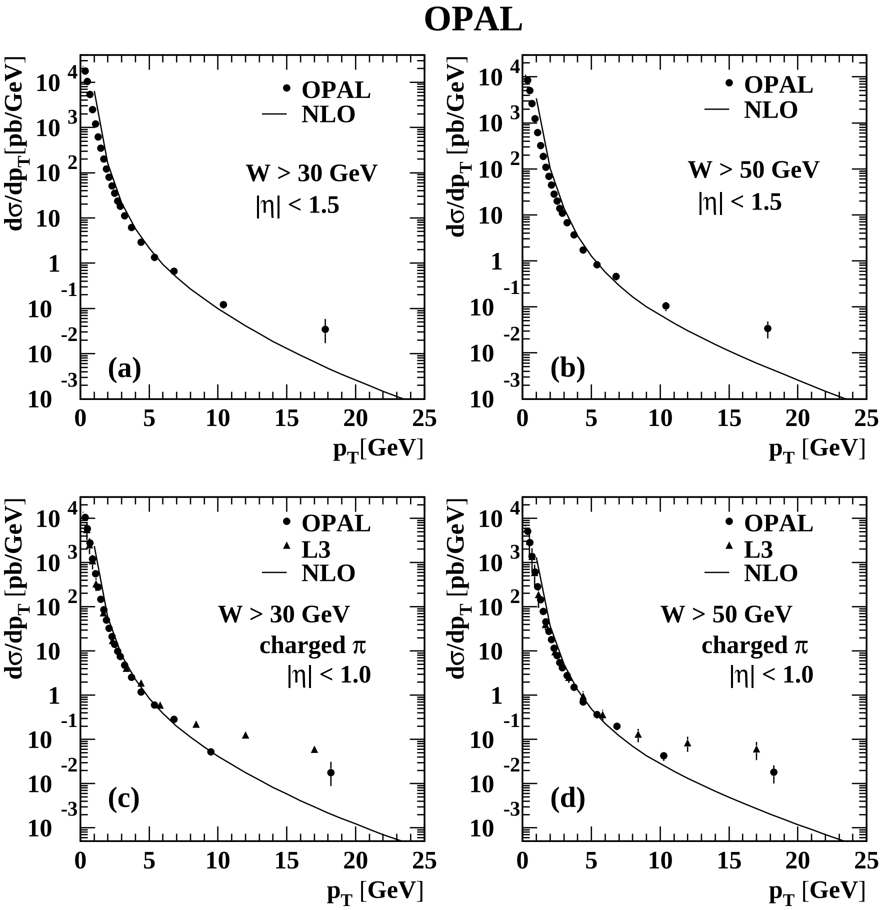

**Figure 8.3.** Differential inclusive charged hadron production cross-sections, $\mathrm{d}\sigma/\mathrm{d}p_{\mathrm{T}}$, for $|\eta| < 1.5$ and in the $W$ ranges (a) $W > 30$ GeV and (b) $W > 50$ GeV. The differential inclusive charged pion production cross-sections $\mathrm{d}\sigma/\mathrm{d}p_{\mathrm{T}}$ for $|\eta| < 1.0$ in the $W$ ranges (c) $W > 30$ GeV and (d) $W > 50$ GeV are inferred from the charged hadron cross-sections using MC information to facilitate the comparison to the L3 measurements [51].

As in the L3 publication the data points are plotted at the mean transverse momentum across the bin. The OPAL data shown in Fig. 8.3 (c) and (d) have been scaled to account for the reduced $|\eta|$ range and for the fraction of charged pions of all charged hadrons using MC simulations. The OPAL data points in Fig. 8.3 are

| | $10 < W < 30$ GeV | |
|---|---|---|
| $p_{\mathrm{T}}$ [GeV] | $\langle p_{\mathrm{T}} \rangle$ [GeV] | $\mathrm{d}\sigma/\mathrm{d}p_{\mathrm{T}}$ [pb/GeV] |
| 0.12–0.28 | 0.20 | $(3.78 \pm 0.01 \pm 0.18) \times 10^{4}$ |
| 0.28–0.44 | 0.35 | $(3.01 \pm 0.01 \pm 0.13) \times 10^{4}$ |
| 0.44–0.60 | 0.51 | $(1.74 \pm 0.00 \pm 0.06) \times 10^{4}$ |
| 0.60–0.80 | 0.69 | $(8.43 \pm 0.03 \pm 0.29) \times 10^{3}$ |
| 0.80–1.00 | 0.89 | $(3.62 \pm 0.02 \pm 0.16) \times 10^{3}$ |
| 1.00–1.20 | 1.09 | $(1.58 \pm 0.01 \pm 0.09) \times 10^{3}$ |
| 1.20–1.40 | 1.29 | $(7.29 \pm 0.08 \pm 0.48) \times 10^{2}$ |
| 1.40–1.60 | 1.49 | $(3.61 \pm 0.06 \pm 0.25) \times 10^{2}$ |
| 1.60–1.80 | 1.69 | $(1.92 \pm 0.04 \pm 0.13) \times 10^{2}$ |
| 1.80–2.00 | 1.89 | $(1.13 \pm 0.03 \pm 0.08) \times 10^{2}$ |
| 2.00–2.20 | 2.09 | $(6.68 \pm 0.23 \pm 0.44) \times 10^{1}$ |
| 2.20–2.40 | 2.29 | $(4.17 \pm 0.19 \pm 0.26) \times 10^{1}$ |
| 2.40–2.60 | 2.50 | $(2.85 \pm 0.16 \pm 0.17) \times 10^{1}$ |
| 2.60–2.80 | 2.70 | $(1.98 \pm 0.13 \pm 0.12) \times 10^{1}$ |
| 2.80–3.00 | 2.90 | $(1.45 \pm 0.12 \pm 0.09) \times 10^{1}$ |
| 3.00–3.50 | 3.21 | $(7.93 \pm 0.56 \pm 0.50) \times 10^{0}$ |
| 3.50–4.00 | 3.71 | $(3.87 \pm 0.42 \pm 0.27) \times 10^{0}$ |
| 4.00–5.00 | 4.40 | $(1.63 \pm 0.22 \pm 0.15) \times 10^{0}$ |
| 5.00–6.00 | 5.40 | $(5.16 \pm 0.78 \pm 0.55) \times 10^{-1}$ |
| 6.00–8.00 | $6.74 \pm 0.01$ | $(1.37 \pm 0.31 \pm 0.22) \times 10^{-1}$ |
| 8.00–15.00 | $9.52 \pm 0.12$ | $(1.90 \pm 0.86 \pm 0.33) \times 10^{-2}$ |

**Table 8.1.** Differential inclusive charged hadron production cross-sections $\mathrm{d}\sigma/\mathrm{d}p_{\mathrm{T}}$ for $|\eta| < 1.5$ and in the $W$ range $10 < W < 30$ GeV. The first uncertainty is the statistical uncertainty and the second uncertainty is the systematic uncertainty. No value is given if the error on $\langle p_{\mathrm{T}} \rangle$ is less than 0.01.

plotted at the mean transverse momentum across the bin, as done in the L3 publication. From this comparison it is evident that the distributions measured by OPAL fall more rapidly towards high transverse momenta than those measured by L3, leading to a disagreement between the two experiments at high transverse momenta and a better description of the OPAL data by NLO QCD than is the case for the L3 data.

| | $30 < W < 50$ GeV | |
|---|---|---|
| $p_{\mathrm{T}}$ [GeV] | $\langle p_{\mathrm{T}} \rangle$ [GeV] | $\mathrm{d}\sigma/\mathrm{d}p_{\mathrm{T}}$ [pb/GeV] |
| 0.12–0.28 | 0.20 | $(1.15 \pm 0.00 \pm 0.03) \times 10^4$ |
| 0.28–0.44 | 0.35 | $(9.01 \pm 0.02 \pm 0.21) \times 10^3$ |
| 0.44–0.60 | 0.51 | $(5.26 \pm 0.02 \pm 0.13) \times 10^3$ |
| 0.60–0.80 | 0.69 | $(2.69 \pm 0.01 \pm 0.07) \times 10^3$ |
| 0.80–1.00 | 0.89 | $(1.22 \pm 0.01 \pm 0.03) \times 10^3$ |
| 1.00–1.20 | 1.09 | $(5.85 \pm 0.05 \pm 0.19) \times 10^2$ |
| 1.20–1.40 | 1.29 | $(2.94 \pm 0.04 \pm 0.11) \times 10^2$ |
| 1.40–1.60 | 1.49 | $(1.59 \pm 0.03 \pm 0.06) \times 10^2$ |
| 1.60–1.80 | 1.69 | $(9.13 \pm 0.21 \pm 0.32) \times 10^1$ |
| 1.80–2.00 | 1.89 | $(5.32 \pm 0.15 \pm 0.19) \times 10^1$ |
| 2.00–2.20 | 2.09 | $(3.34 \pm 0.12 \pm 0.11) \times 10^1$ |
| 2.20–2.40 | 2.29 | $(2.22 \pm 0.10 \pm 0.07) \times 10^1$ |
| 2.40–2.60 | 2.50 | $(1.47 \pm 0.08 \pm 0.04) \times 10^1$ |
| 2.60–2.80 | 2.70 | $(1.00 \pm 0.06 \pm 0.03) \times 10^1$ |
| 2.80–3.00 | 2.90 | $(7.48 \pm 0.54 \pm 0.26) \times 10^0$ |
| 3.00–3.50 | 3.23 | $(4.33 \pm 0.26 \pm 0.15) \times 10^0$ |
| 3.50–4.00 | 3.73 | $(2.32 \pm 0.19 \pm 0.08) \times 10^0$ |
| 4.00–5.00 | 4.42 | $(1.12 \pm 0.09 \pm 0.04) \times 10^0$ |
| 5.00–6.00 | 5.43 | $(5.05 \pm 0.66 \pm 0.19) \times 10^{-1}$ |
| 6.00–8.00 | 6.74 | $(2.10 \pm 0.33 \pm 0.12) \times 10^{-1}$ |
| 8.00–15.00 | $9.62 \pm 0.03$ | $(2.23 \pm 0.60 \pm 0.36) \times 10^{-2}$ |

**Table 8.2.** Differential inclusive charged hadron production cross-sections $\mathrm{d}\sigma/\mathrm{d}p_{\mathrm{T}}$ for $|\eta| < 1.5$ and in the $W$ range $30 < W < 50$ GeV. The first uncertainty is the statistical uncertainty and the second uncertainty is the systematic uncertainty. No value is given if the error on $\langle p_{\mathrm{T}} \rangle$ is less than 0.01.

| | $50 < W < 125$ GeV | |
|---|---|---|
| $p_{\mathrm{T}}$ [GeV] | $\langle p_{\mathrm{T}} \rangle$ [GeV] | $\mathrm{d}\sigma/\mathrm{d}p_{\mathrm{T}}$ [pb/GeV] |
| 0.12–0.28 | 0.20 | $(1.00 \pm 0.00 \pm 0.03) \times 10^{4}$ |
| 0.28–0.44 | 0.35 | $(7.77 \pm 0.02 \pm 0.22) \times 10^{3}$ |
| 0.44–0.60 | 0.51 | $(4.58 \pm 0.01 \pm 0.13) \times 10^{3}$ |
| 0.60–0.80 | 0.69 | $(2.37 \pm 0.01 \pm 0.07) \times 10^{3}$ |
| 0.80–1.00 | 0.89 | $(1.12 \pm 0.01 \pm 0.03) \times 10^{3}$ |
| 1.00–1.20 | 1.09 | $(5.56 \pm 0.04 \pm 0.14) \times 10^{2}$ |
| 1.20–1.40 | 1.29 | $(2.92 \pm 0.03 \pm 0.08) \times 10^{2}$ |
| 1.40–1.60 | 1.49 | $(1.66 \pm 0.02 \pm 0.05) \times 10^{2}$ |
| 1.60–1.80 | 1.69 | $(9.74 \pm 0.15 \pm 0.30) \times 10^{1}$ |
| 1.80–2.00 | 1.89 | $(6.10 \pm 0.11 \pm 0.21) \times 10^{1}$ |
| 2.00–2.20 | 2.09 | $(4.01 \pm 0.09 \pm 0.15) \times 10^{1}$ |
| 2.20–2.40 | 2.29 | $(2.53 \pm 0.07 \pm 0.10) \times 10^{1}$ |
| 2.40–2.60 | 2.50 | $(1.76 \pm 0.06 \pm 0.09) \times 10^{1}$ |
| 2.60–2.80 | 2.70 | $(1.22 \pm 0.05 \pm 0.06) \times 10^{1}$ |
| 2.80–3.00 | 2.90 | $(9.52 \pm 0.44 \pm 0.50) \times 10^{0}$ |
| 3.00–3.50 | 3.23 | $(5.99 \pm 0.22 \pm 0.30) \times 10^{0}$ |
| 3.50–4.00 | 3.73 | $(3.33 \pm 0.16 \pm 0.22) \times 10^{0}$ |
| 4.00–5.00 | 4.40 | $(1.52 \pm 0.08 \pm 0.15) \times 10^{0}$ |
| 5.00–6.00 | 5.43 | $(7.02 \pm 0.83 \pm 0.81) \times 10^{-1}$ |
| 6.00–8.00 | 6.83 | $(3.89 \pm 0.45 \pm 0.49) \times 10^{-1}$ |
| 8.00–15.00 | $10.18 \pm 0.01$ | $(8.40 \pm 1.34 \pm 0.90) \times 10^{-2}$ |
| 15.00–25.00 | $18.26 \pm 0.09$ | $(2.46 \pm 0.96 \pm 0.26) \times 10^{-2}$ |

**Table 8.3.** Differential inclusive charged hadron production cross-sections $\mathrm{d}\sigma/\mathrm{d}p_{\mathrm{T}}$ for $|\eta| < 1.5$ and in the $W$ range $50 < W < 125$ GeV. The first uncertainty is the statistical uncertainty and the second uncertainty is the systematic uncertainty. No value is given if the error on $\langle p_{\mathrm{T}} \rangle$ is less than 0.01.

|  | $10 < W < 125$ GeV |  |
|---|---|---|
| $p_T$ [GeV] | $\langle p_T \rangle$ [GeV] | $d\sigma/dp_T$ [pb/GeV] |
| 0.12–0.28 | 0.20 | $(5.93 \pm 0.00 \pm 0.21) \times 10^4$ |
| 0.28–0.44 | 0.35 | $(4.68 \pm 0.00 \pm 0.18) \times 10^4$ |
| 0.44–0.60 | 0.51 | $(2.71 \pm 0.00 \pm 0.10) \times 10^4$ |
| 0.60–0.80 | 0.69 | $(1.34 \pm 0.00 \pm 0.05) \times 10^4$ |
| 0.80–1.00 | 0.89 | $(5.87 \pm 0.01 \pm 0.25) \times 10^3$ |
| 1.00–1.20 | 1.09 | $(2.68 \pm 0.01 \pm 0.14) \times 10^3$ |
| 1.20–1.40 | 1.29 | $(1.29 \pm 0.01 \pm 0.07) \times 10^3$ |
| 1.40–1.60 | 1.49 | $(6.78 \pm 0.04 \pm 0.38) \times 10^2$ |
| 1.60–1.80 | 1.69 | $(3.78 \pm 0.03 \pm 0.20) \times 10^2$ |
| 1.80–2.00 | 1.89 | $(2.27 \pm 0.02 \pm 0.12) \times 10^2$ |
| 2.00–2.20 | 2.09 | $(1.41 \pm 0.02 \pm 0.07) \times 10^2$ |
| 2.20–2.40 | 2.29 | $(9.03 \pm 0.16 \pm 0.44) \times 10^1$ |
| 2.40–2.60 | 2.50 | $(6.18 \pm 0.13 \pm 0.31) \times 10^1$ |
| 2.60–2.80 | 2.70 | $(4.26 \pm 0.11 \pm 0.22) \times 10^1$ |
| 2.80–3.00 | 2.90 | $(3.25 \pm 0.09 \pm 0.17) \times 10^1$ |
| 3.00–3.50 | 3.23 | $(1.93 \pm 0.05 \pm 0.10) \times 10^1$ |
| 3.50–4.00 | 3.73 | $(1.03 \pm 0.03 \pm 0.06) \times 10^1$ |
| 4.00–5.00 | 4.43 | $(4.66 \pm 0.16 \pm 0.34) \times 10^0$ |
| 5.00–6.00 | 5.43 | $(1.71 \pm 0.11 \pm 0.13) \times 10^0$ |
| 6.00–8.00 | 6.79 | $(7.28 \pm 0.53 \pm 0.62) \times 10^{-1}$ |
| 8.00–15.00 | 10.00 | $(1.14 \pm 0.14 \pm 0.09) \times 10^{-1}$ |
| 15.00–25.00 | $18.27 \pm 0.08$ | $(2.76 \pm 0.99 \pm 0.22) \times 10^{-2}$ |

**Table 8.4.** Differential inclusive charged hadron production cross-sections $d\sigma/dp_T$ for $|\eta| < 1.5$ and in the $W$ range $10 < W < 125$ GeV. The first uncertainty is the statistical uncertainty and the second uncertainty is the systematic uncertainty. No value is given if the error on $\langle p_T \rangle$ is less than 0.01.

| | $10 < W < 30$ GeV | | $30 < W < 50$ GeV | |
|---|---|---|---|---|
| $\lvert\eta\rvert$ | $\langle\lvert\eta\rvert\rangle$ | $\mathrm{d}\sigma/\mathrm{d}\lvert\eta\rvert$ [pb] | $\langle\lvert\eta\rvert\rangle$ | $\mathrm{d}\sigma/\mathrm{d}\lvert\eta\rvert$ [pb] |
| 0.0–0.3 | 0.149 | 3.26±0.45±0.29 | 0.151 | 2.49±0.26±0.07 |
| 0.3–0.6 | 0.445 | 3.52±0.50±0.39 | 0.451 | 2.41±0.25±0.08 |
| 0.6–0.9 | 0.754 | 3.11±0.47±0.41 | 0.759 | 2.48±0.26±0.07 |
| 0.9–1.2 | 1.047 | 2.58±0.43±0.24 | 1.049 | 2.15±0.26±0.17 |
| 1.2–1.5 | 1.348 | 2.40±0.44±0.28 | 1.341 | 1.74±0.23±0.07 |

| | $50 < W < 125$ GeV | | $10 < W < 125$ GeV | |
|---|---|---|---|---|
| $\lvert\eta\rvert$ | $\langle\lvert\eta\rvert\rangle$ | $\mathrm{d}\sigma/\mathrm{d}\lvert\eta\rvert$ [pb] | $\langle\lvert\eta\rvert\rangle$ | $\mathrm{d}\sigma/\mathrm{d}\lvert\eta\rvert$ [pb] |
| 0.0–0.3 | 0.149 | 4.17±0.27±0.63 | 0.149 | 10.90±0.65±0.90 |
| 0.3–0.6 | 0.449 | 3.63±0.25±0.53 | 0.448 | 9.92 ±0.62±0.65 |
| 0.6–0.9 | 0.759 | 3.57±0.25±0.46 | 0.757 | 9.89 ±0.63±0.63 |
| 0.9–1.2 | 1.048 | 2.81±0.23±0.34 | 1.047 | 8.04 ±0.58±0.67 |
| 1.2–1.5 | 1.345 | 2.81±0.22±0.25 | 1.345 | 7.42 ±0.55±0.44 |

**Table 8.5.** Differential inclusive charged hadron production cross-sections $\mathrm{d}\sigma/\mathrm{d}|\eta|$ for $p_T > 3.5$ GeV and in the $W$ ranges $10 < W < 30$ GeV, $30 < W < 50$ GeV, $50 < W < 125$ GeV and $10 < W < 125$ GeV. The first uncertainty is the statistical uncertainty and the second uncertainty is the systematic uncertainty.

## 8.1 Outlook

In 2007 months Thorsten Wengler in the International Europhysics Conference on High Energy Physics [58] summarized the hadronic interactions of two quasi-real photons during the LEP1 and the LEP2 data taking periods. He mentioned thedisagreement between NLO QCD predictions and measurement in two-photon processes had been observed is the region of high transverse momentum in single jet and particle production. It is OPAL had fallen more rapidly towards high $p_T$ than those had measured by L3. In consequence there was a disagreement between the two experiments in this region and a better description of the OPAL data by NLO QCD than is the case for the L3 data. The only OPAL data point significantly higher than the calculation was that at highest $p_T$, NLO QCD was the correct theory to describe this process.

Philip Yock in his paper and presentation [59], [60] assumed, that data were suggestive of models where quarks have unit charges, or larger, and where partons have substructure. Since not only the data exceeded the predictions in all channels, but the excesses in each channel grew with transverse momentum, one might expect quarks with larger charges than the fractional values to explain these discrepancies. The data call for independent testing, preferably at higher energies and higher transverse momenta. Such testing could be carried with either of the linear colliders (ILC or CLIC), but an electron-electron collider based on the plasma wakefield acceleration technique could provide the most affordable option.

Based on these results Bylinkin and Rostovtsev proposed [61] a new parameterization of the spectrum shape of inclusive charged particles produced in high energy collisions. This new parameterization describes the available experimental data significantly better than the broadly used Tsallis-type parameterization. The proposed parameterization was a sum of an exponential (Boltzman-like) and a power law (Tsallis-like) terms. The parameters of these two terms turned out to be strongly correlated.

DELPHI found that the differential inclusive $\mathrm{d}\sigma/\mathrm{d}p_\mathrm{T}$ cross-section is compatible, within errors, with the PYTHIA and NLO QCD predictions up to high $p_\mathrm{T}$ [62]. They measured in the low $W_\mathrm{vis}$ region (5 GeV<$W_\mathrm{vis}$<35 GeV). The DELPHI measurement is incompatible with the L3 data.

# Chapter 9

# Summary and Conclusion

## 9.1 CMS Muon Aligment

The Higgs boson should be detectable via its decay into 2 $Z$ bosons with its four-lepton final states. If the leptons are muons, the best 4-particle mass resolution can be achieved since muons are less affected than electrons by radiative losses in the tracker material. The $H \rightarrow W^+W^- \rightarrow \mu^+\mu^-\nu_\mu\nu_\mu$ is also important but it needs a very accurate missing $E_T$ measurement. In these two channels the good muon identification and momentum resolution over a wide range of momenta and the good dimuon mass resolution are required. The principal part of my work at CMS is the alignment of muon chambers. Bounds have been set on the required accuracy [12] and the influence of the chamber misalignment on the momentum resolution has been studied for both barrel and endcap detectors. The required accuracy, in $r - \Phi$, for the barrel detector is in the range of 150- 350 $\mu$m (for MB1-MB4 respectively), while for the endcap system it is 75-200 $\mu$m (for ME1- ME4).

The stability of the muon chambers at the 100 $\mu$m level is not guaranteed during detector operation. The detector is instrumented with an optical alignment system, which will allow continual measurement of the chambers position.

The full system is segmented in six $\Phi$-planes (active alignment planes) to which the three tracking detectors are connected. Fig. 9.1 shows the muon alignment scheme for two radial opposite planes.

The monitoring system for the barrel part is designed to measure the positions of the barrel chambers with respect to each other. Rigid carbon fibre structures called MABs (Module for Alignment of Barrel) are fixed on the faces of the 5 wheels of the CMS steel yoke, forming 12 planes parallel to the beam. Optogeometrical reference

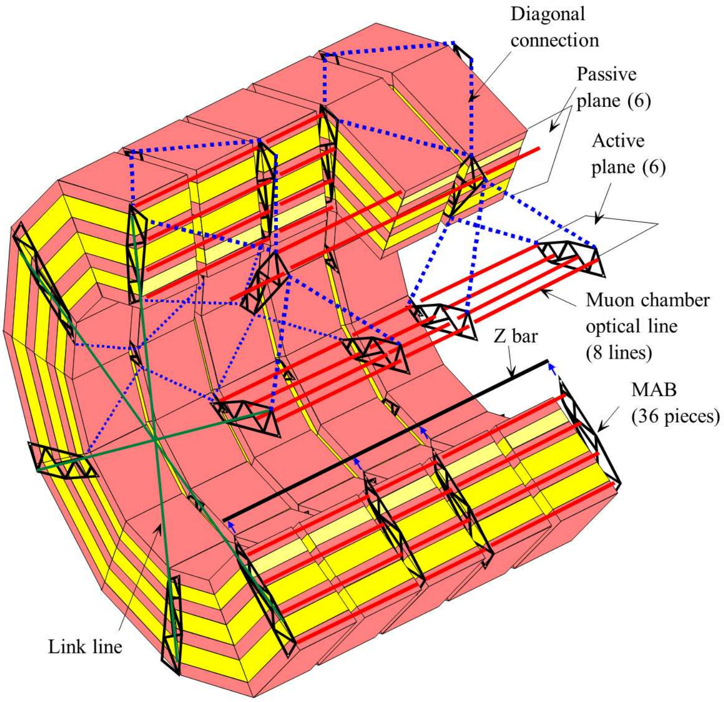

**Figure 9.1.** Lateral view of the CMS detector, showing the Barrel Alignment system. [8]

bodies (LED light sources) are fixed rigidly to the barrel muon chambers and monitored by cameras located on the MABs. Each chamber is simultaneously measured by 4 cameras located on 4 independent MABs, this redundancy ensures the robustness of the measurement. During the operation of our alignment system the centroid of the LEDs' light are detected by the video cameras and the centroid calculated. These centroids together with the calibration data obtained during the assembly and installation of the system serve as input for the reconstruction program called COCOA (CMS Object-oriented Code for Optical Alignment). This is C++ software that is able to reconstruct the positions, orientations of the chambers and MABs. Due to the large number of elements (600 cameras on 36 MABs and $\sim$10000 LEDs on the 250 DTs) there was a need to automate the COCOA input file generation.

I created a script that (based on the DQM - Data Quality Monitoring conditions) collects the relevant centroids, reads the configurations and calibrations from databases and creates the COCOA input file. Running the reconstruction needs large amount of computational resources, hence it is performed in two steps. First the positions of the chambers in the 1st, 2nd and 3rd stations and all the MABs are reconstructed. Then the positions of the DTs in station 4 are calculated with respect to the MAB positions obtained during the first step. Our reconstuctions were validated by track alignment and used in [19] and [20].

In 2010 and 2011 the access to camera measurements of 4 MABs has been lost. Since $z$ position of the chambers is measured by triangulation using the closest light source measurement to the MAB, missing MABs can complicate at first the $z$ measurement. More missing MABs in a plane are expected to have effect on the $r - \Phi$ precision, but the impact on the full reconstructon is a very complex question. There was a need to show the redundancy and robustness of the measurement and the reconstruction. I studied [21] the recostruction with all of the MABs and without the 4 missing ones at a validated run, taken on 07.03. 2010., when all the 36 MABs were still operational. The reconstructed positions of the MABs installed on the central wheel were then fit on those of the non-missing MABs reconstruction.

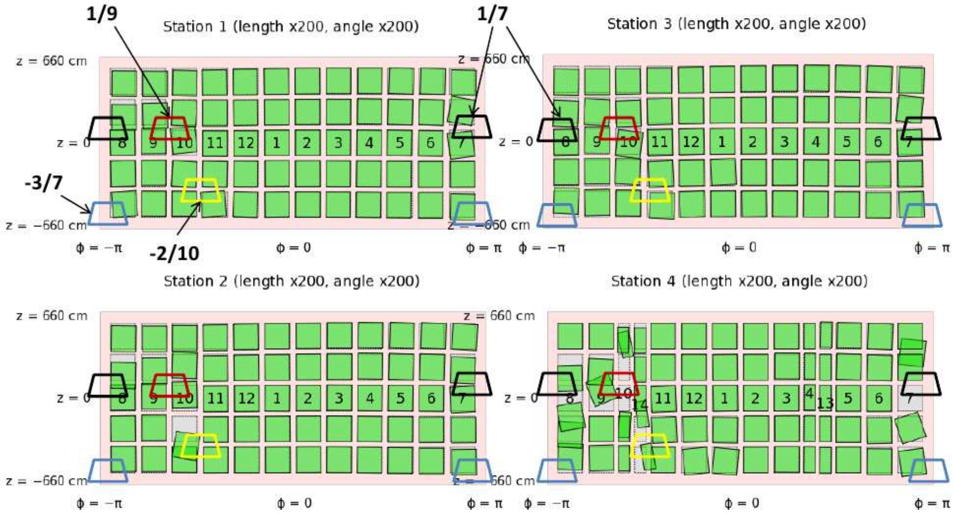

**Figure 9.2.** Unrolled view of the differences between the reconstructions with and without the missing MABs in local $x'$, $y'$ and rotation around local $z'$.

As a result of this fit both reconstructions are expressed in the same coordinate system, and the differences show only the local displacements and rotations. The differences in the local x′ and y′ and the rotation around local z′ between the two reconstructions are shown on Fig. 9.2. On this type of plots the displacements and rotations are multiplied by 200, the unit is the chamber size. By this enlargement the sub-millimeter differences in local x′ and local y′ as well as the small ($< 0.1$ mrad) differences in rotation around local z′ can be made visible. The trapezoids indicate the missing MABs and can be identified by their colors: 1/9 (red), -2/10 (yellow), 1/7 (black) and -3/7 (blue).

The differences are restricted to the sectors 7, 8, 9 and 10(, 14 at station 4 the chambers in sectors 10 and 14 are double chambers on the top and 4,13 on the bottom).

The rotation around local $y'$ (global Z), local x′ and local z′ can be seen on the transverse view (Fig. 9.3).

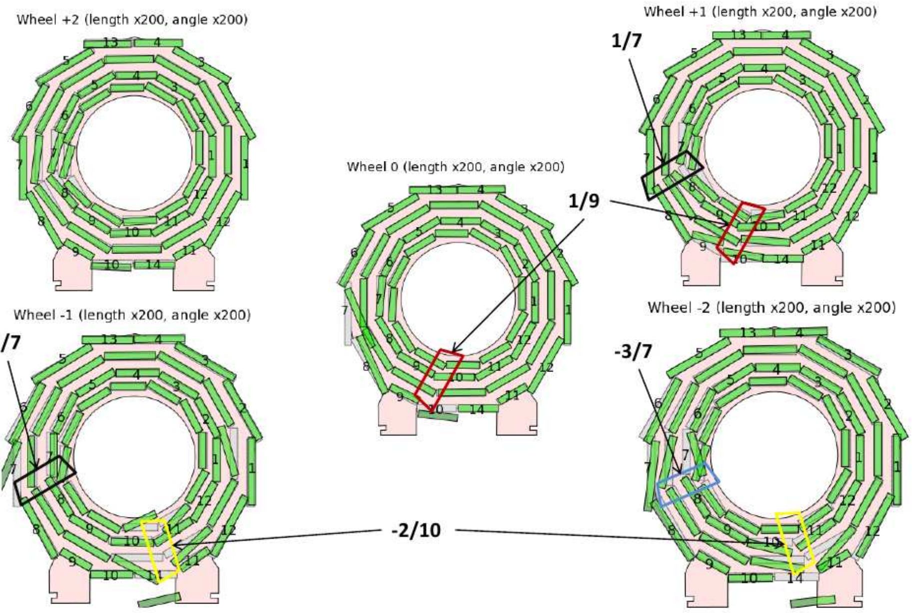

**Figure 9.3.** Transversal view of the differences between the reconstructions with and without the missing MABs in local $x'$, $z'$ and rotation around local $y'$

The differences are restricted to sectors 7, 8, 9, 10 and 14. The rotation error in the area of missing MABs is clearly connected to the fact that some chambers are measured only at one side and the measurement of the other side is weak or missing. Nevertheless, this has only a minor impact on the precision of muon momentum measurement, since it induced only a second order effect on the displacement.

Even with the missing MABs, the momenta of muons can still be reconstructed with the expected precision using our alignment results.

## 9.2 OPAL Inclusive Hadrons in Two-Photon Interactions

The LEP was a good source of photon due to the electron and positron beams. The high energy electron and positron beams radiated photons, and thus produced a beam of high energy photons. The energy spectrum for the produced photon is well described by the equivalent photon approximation. The total hadronic cross-section of the photon-photon interaction increased with the beam energy, thus a huge amount of data was accessible. The photon theory described in Chapter 4 shows our current knowledge about the structure of the photon and its interactions. Photons at high energy can fluctuate into two-fermion pair, with energy comparable to the lightest quark pair, hadronic final states are also available.

In the framework of the QCD-improved parton model the two-photon cross-section is described as a convolution of parton-parton scattering, parton density functions and fragmentation functions. The factorization theorem ensures that the two-photon cross-section depends on the processes that are considered, whereas the latter two are universal and have to be determined by fitting experimental data.

OPAL was a multipurpose apparatus designed to efficiently reconstruct and identify all types of events. The selection was done in two stages, firstly every working group created their own set of files using general preselection, then the final selections were applied. Besides the previously used untagged photon selection criteria I used the cut on impact parameter with which the not well reconstructed tracks were rejected (see 6.4.1).

The data were taken at $e^+e^-$ centre-of-mass energies from 183 to 209 GeV with a total integrated luminosity of 612.831 $pb^{-1}$. The luminosity-weighted average centre-of-mass energy was 195.8 GeV. The differential cross-sections as a function of the transverse momentum and the pseudorapidity of the hadrons were compared to theoretical calculations of up to next-to-leading order in the strong coupling constant $\alpha_s$ (see Fig 9.4). The NLO calculation lies significantly below the data for transverse momenta greater than about 10 GeV, which can be reached in the highest $W$ range only.

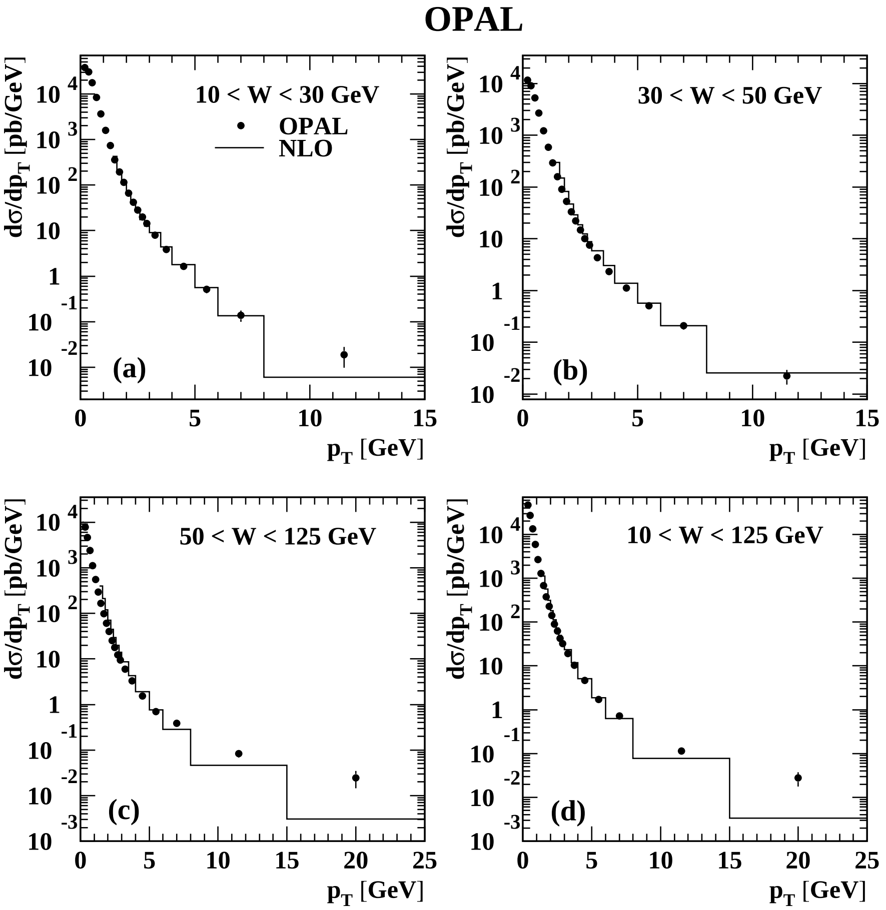

**Figure 9.4.** Differential inclusive charged hadron production cross-sections $\mathrm{d}\sigma/\mathrm{d}p_{\mathrm{T}}$. The data are compared to an NLO calculation.

The predictions of PHOJET and PYTHIA (not shown) at high $p_{\mathrm{T}}$ are similar to the NLO calculation.

Fig. 9.5 (a) and (b) show the differential cross-section $\mathrm{d}\sigma/\mathrm{d}p_{\mathrm{T}}$ for charged hadrons for $W > 30$ GeV and $W > 50$ GeV to facilitate a comparison with the latest measurement by L3 of charged pions in the pseudorapidity range $|\eta| < 1.0$ [51].

From this comparison it is evident that the distributions measured by OPAL fall more rapidly at high transverse momenta than those measured by L3, leading to a disagreement between the two experiments at high transverse momenta and a better description of the OPAL data by NLO QCD than is the case for the L3 data. In the

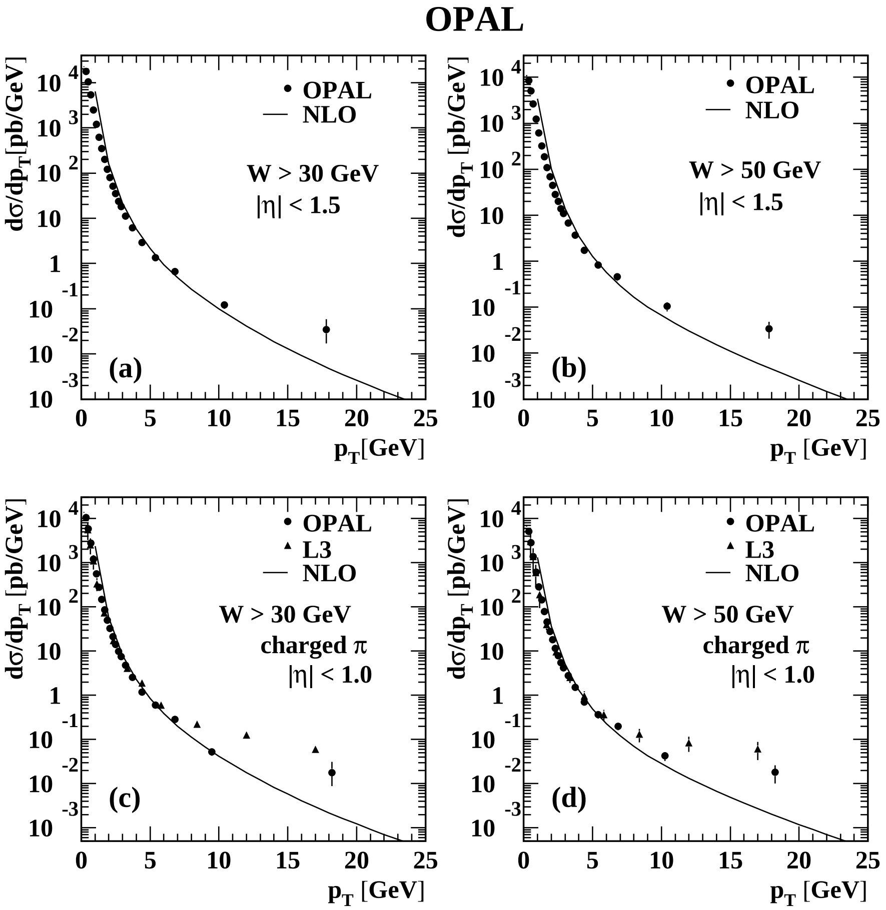

**Figure 9.5.** Differential inclusive charged hadron production cross-sections (a) and (b), $d\sigma/dp_T$. and differential inclusive charged pion production cross-sections compared to the L3 measurements (c) and (d).

inclusive jet differential cross-section the OPAL [53] descibed also better the NLO than L3 [54].

# Chapter 10

# Összefoglalás

## 10.1. CMS Müon Helymeghatározó Rendszere

A CMS egy általános célú detektor az LHC gyorsítónál, célja a nagy energiájú és intenzitású proton-proton ütközések vizsgálata. A $H \rightarrow ZZ \rightarrow l^+l^-l^+l^-$ bomlási csatorna ( 10.1 ábra)

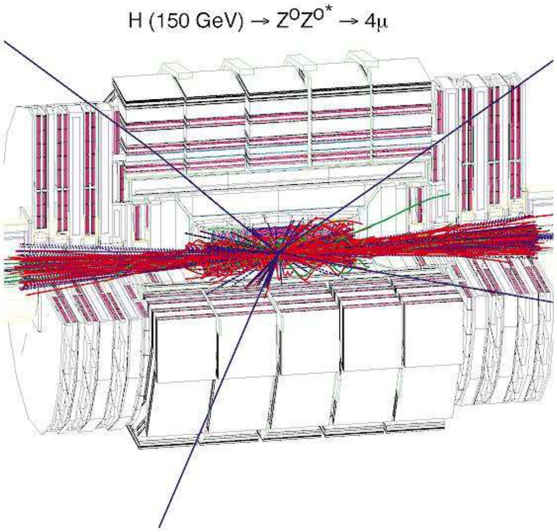

10.1. ábra. A 150 GeV-es Higgs bozon bomlása 4 müonná (négy kék vonal) a más, főleg a hadronos (piros vonalak) végállapothoz képest.

, ha a leptonok müonok, az egyik legtisztábban észlelhető megjelenése a Higgs bozonnak. Ehhez azonban nagyon pontos müon impulzus meghatározás kell ami a müon detektorok érzékenysége mellett megszabja a térbeli elhelyezkedésük pontosságát is. A három müon detektor fajta közül (2.1 fejezet) a sokcellás gáztöltésű drift kamrák helyzetének monitorozásában vettem részt.

Mivel a drift kamrák mozgása a CMS működése során, elsősorban a mágnes ki- és bekapcsolásakor, az elvárt 100-350 $\mu$m-es ($r - \Phi$-ben) pontosságot meghaladja, aktív eszközökre volt szükség a helyzetük nyomon követésére. Ezt a Barrel Müon Helymeghatározó Rendszer valósítja meg (10.2 ábra).

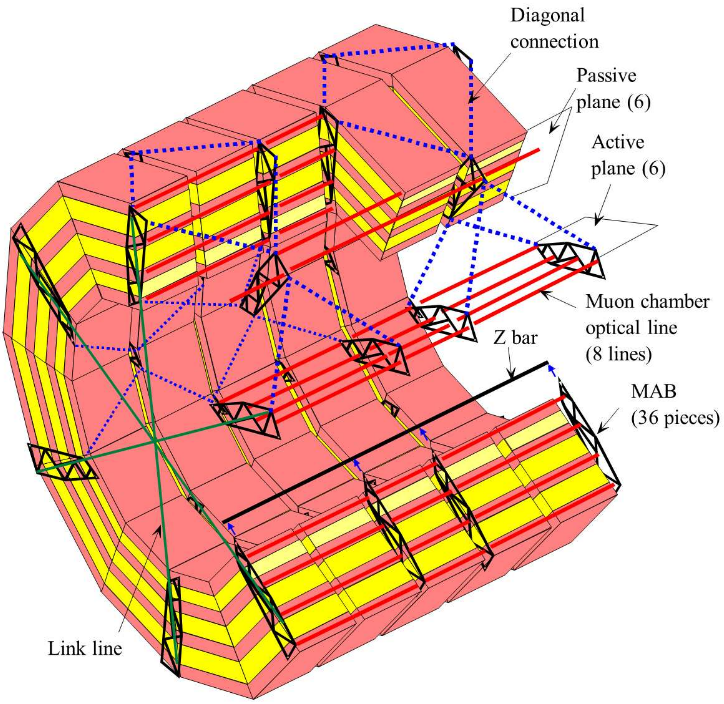

10.2. ábra. Drift kamrák, MAB-ok és az optikai összeköttetések.

A kamrák (az ábrán a sötét rózsaszín téglatestek, sárgával az őket tartó vázszerkezetet jelölöm) 4 réteget és 12 síkot alkotnak. Az aktív síkon 4 MAB (Module for Alignment of Barrel) a passzív síkon 2 MAB helyezkedik el. A MAB-okon lévő kamerák a kamrákra rögzített villák LED-jei középpontját mérik. Minden kamrán 4 villa található, ezeken 4 illetve 6 LED van oldalanként. Egy kamra LED-jeit 4 kamera méri 4 különböző MAB-ról, ami az alapja a redszerünk redundanciájának és robosztusságának. Az egyes síkokat elsősorban a kamrák kalibrációs adatai alapján lehet egy egységes modellben kiértékelni.

A kiértékelést egy COCOA (CMS Object-oriented Code for Optical Alignment) nevű C++ nyelven megírt, a CMS szoftverrendszerébe ágyazott program végzi. Ez a program a mérések és a kalibrációk alapján a legkisebb négyzetek módszerével meghatározza a kamrák és a MAB-ok helyzetét a saját koordináta-rendszerükben, amit egy transzformációval viszünk át a CMS koordináta-rendszerébe. A COCOA számára egy egyedi bemenő fájlt kell elkészíteni, amiben le kell írni a rendszer hierarchikus felépítésést, meg kell adni a kalibrációkat és a méréseket egy kötött formában. Miután lefut egy teljes mérés, azaz minden LED képének a centroidját kiszámolja a MAB-ra helyezett számítógép, az értékek adatbázisba kerülnek. Ebben az adatbázisban valósítottuk meg az adatok minőségét ellenőrző (DQM, Data Quality Monitoring) rutinokat. Mivel 10000 LED, 250 kamra, 36 MAB és 600 kamera a teljes rendszer, a COCOA-hoz szükséges bemenő adatkoat hiba nélkül kézzel fájlba írni még a rendszer egy töredékére is hónapok munkája, a csoporthoz csatlakozásomkor ennek az automatizálását kaptam feladatul.

Egy Root szkriptben valósítottam ezt meg, mivel ez a CERN általános adatfeldolgozó keretrendszere, ráadásul egyszerűen megvalósítható benne a különböző adatabázisokhoz való hozzáférés. A szkript öszegyűjti a rendszer elemeit egy konfigurációs adatbázisból, megvizsgálja, hogy az adott elem (MAB, kamera, kamra, villa, LED) az adott mérés alapján részt vehet-e a kiértékelésben. Ha igen, akkor a kalibrációs adatait egy újabb adatbázisból kiolvassa. Ezután összegyűjti egy újabb adatbázisból a méréseket és ezeket a COCOA által megszabott formátumban egy fájlba írja. Ezt a fájlt futtatjuk a COCOA-val. Ezt a lépést az elemek nagy száma miatt két részre kellett bontanom. Első futáskor az első három réteg (station) kamráit és a MAB-ok helyzetét fittelem meg. Ennek az is az oka, hogy a negyedik réteg kalibrációjának nagyobb a bizonytalansága, így az első futáskor egy fittelés szempontjából homogénebb rendszerem van, a negyedik réteg nagyobb hibája nem hat ki a pontosabban kalibrált első három réteg eredményére. Ezután a második futásnál a negyedik réteg kamráit fittelem meg, de a MAB-ok helyzetét már rögzítettnek véve.

A mi rekonstrukciónkat, a részecskepálya alapján számolt pozícióval ellenőrizve, használta a CMS a kozmikus müonok vizsgálatakor [19] és a 2010, 2011-es évben [20].

Ezekben az években 4 MAB-ot nem tudtunk használni a méréseink során, de ebből 3 már a rekonstruált, majd ellenőrzott eredményeink publikálása után vált elérhetetlenné a vezérlő szoftver számára. Az első egy ismert, keretrendszerünkben lévő hiba miatt esett ki, amit azóta a legtöbb MAB-on lévő számítógépen kijavítottunk (az eléhető pozíciókban), de ehhez a MAB-hoz azóta nem tudtunk hozzáférni.

A másik 3 MAB számítógépe egy áramszünet után hibásodott meg, ezeket is csak a 2013-as nagy leálláskor tudjuk elérni, megjavítani. Jogosan merült fel a kérdés, hogy 4 hiányzó MAB-bal lehetséges-e még az elvárt pontosságú kiértékelés. Egy olyan mérést választotunk ehhez, amiben mind a 36 MAB működött, és egyenként eltávolítva a mérésekből a hiányzó MAB-ok kameráinak mérésit, megvizsgáltuk a fittelés eredményeit [21]. A 10.3 ábrán az eredeti rekonstrukciót és a 4 MAB eltávolítása utáninak a különbségeket láthatjuk felnagyítva.

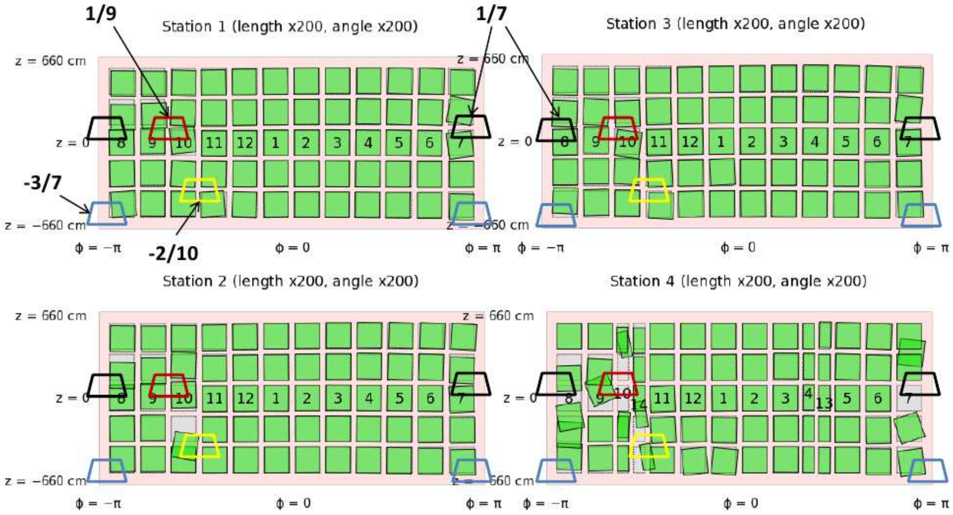

10.3. ábra. A különböző rétegek kamráinak pozíciójának es elfordulásának a küönbsége az eredeti kiértékelésben és a 4 hiányzó MAB esetén

Vízszintesen a kamrák $r - \Phi$, függőlegesen a nyalábvezetékkel párhuzamos z változását, a forgásban pedig a kamra síkjára merőleges forgásokat: $\mathrm{rot}(z')$ mutatom felnagyítva. A színes trapézok a rekonstrukcióból kivett MAB-okat jelentik. Az első ránézésre látható, hogy a két rekonstrukció között a hiányzó MAB-okhoz közel van eltérés, a többi síkban ez elhanyagolható. Az $r - \Phi$, z és $\mathrm{rot}(z')$ szórását a különböző rétegekben a hiányzó MAB-okhoz közel, ezektől távol a 10.1 táblázatban összesítettem.

Az eredmények alapján megállapíthatom, hogy az eredeti elvárásnak a rendszer nagy része megfelel és még a hiányzó MAB-okhoz közeli kamrák esetén is a azóta dominánssá váló részecskenyomok alapján történő helymeghatározás pontosságát elérjük, azt ellenőrizni lehet a rendszerünkkel.

10.1. táblázat. Az egyes rétegekben a hiányzó MAB-ok miatti elmozdulás, forgás szórása síkok két csoportjában

| Sík 7-10 | réteg 1 | réteg 2 | réteg 3 | réteg 4 |
|---|---|---|---|---|
| $r - \Phi$ szórása | 0.2993 mm | 0.2775 mm | 0.3089 mm | 0.5193 mm |
| z szórása | 0.7790 mm | 1.0460 mm | 0.5971 mm | 1.2280 mm |
| rot(z′) szórása | 0.2972 mrad | 0.2078 mrad | 0.2128 mrad | 0.3938 mrad |

| Sík 1-6, 11,12 | réteg 1 | réteg 2 | réteg 3 | réteg 4 |
|---|---|---|---|---|
| $r - \Phi$szórása | 0.2391 mm | 0.2105 mm | 0.3002 mm | 0.2920 mm |
| z szórása | 0.2027 mm | 0.2481 mm | 0.3278 mm | 0.2741 mm |
| rot(z′) szórása | 0.0888 mrad | 0.0582 mrad | 0.0998 mrad | 0.1241 mrad |

## 10.2. Töltött hadronok transzverzális impulzus-eloszlása

A fotonok energiaspektruma jól leírható a EPA közelítéssel (4.3.1 fejezet). A két nyaláb által kibocsátott fotonok ütközésekor kvark párok, ezekből hadronok keletkeznek (4.3.2 fejezet), melyekkel a fotonok parton tartalma és ezeknek a partonoknak a hadronizációja mérhető. A vizsgált folyamat:

$$e_1(p_1)e_2(p_2) \rightarrow e_1(p_1')e_2(p_2')h(p_h)X, \tag{10.1}$$

hatákeresztmetszete növekszik a nyaláb energiájával, a LEP2 energiáin már domináns (bár a csoportunkon kívül mindenki számára háttér) folyamat volt.

A foton megfigyelhető, mint közvetlen foton, amikor oszthatatlan egységként viselkedik , de a nagy energiákon vizsgálható, mint egy fotonnal azonos kvantumszámokkal rendelkező hadron vagy mint egy fermion pár (4.1 fejezet), ekkor szerkezetet mutat. A parton modellben a kétfoton kölcsönhatás a parton szórás, a parton sűrűségfüggvény és a fragmentációs függvény konvolúciójával írható le. Az első tag QCD-ben számolható, a második kettő pedig más kísérletek eredményeiből származtatható.

Az OPAL mérései közül, tömegközépponti energiában megadva, a 183-tól

209 GeV-ig tartó energia intervallumot használtam, ez összesen 612.831 pb$^{-1}$ integrális luminozitást jelent, a luminozitással súlyozott energiaközép 195.8 GeV.

Az adaton és a Monte Carlo szimulćiókon (6.1.2 fejezet) kétszintű vágást használtam, az első szinten a csoport egészére érvényes vágásokkal (6.2 fejezet) csökkentettem a feldolgozandó adatfájlok nagyságát. Második lépésként a saját vágásaimat (6.4 fejezet) alkalmazva végeztem el az analízist, ezek a következők voltak:

- Legalább 6 részecskenyom a részecskeazonosító kamrában;
- A HCAL (5.1.4 fejezet) és ECAL (5.1.3 fejezet) kaloriméterekben leadott energia nem lehet több, mint 50 GeV;
- Az előremeneti FD (5.1.6 fejezet) és SW (5.1.6 fejezet) detektorokban a leadott energia nem lehet több, mint 60 GeV;
- Az elsődleges ütközési pont távolsága a nominális ütközési ponttól sugárirányban nem lehet több, mint 2 cm és a nyalábbal párhuzamosan, mint 3 cm;
- A csak az ECAL-lal mért látható invariáns tömeg nagyobb kell, hogy legyen, mint 3 GeV;
- A csak az ECAL és FD detektorral mért hiányzó tranverzális impulzus kisebb, mint 8 GeV;
- Minden részecskenyom rendelkezik legalább 120 MeV inpulzussal, a geometriailag indokolt beütések felét, de legalább 40-et detektálni kell a CJ-ben (5.1.1 fejezet);
- részecskenyom távolsága az elsődleges ütközési ponttól nem lehet több, mint 0.15 cm.

A legutolsó feltétel nem szerepelt a korábbi analízisekben, ez magyarázatra szorul. Azt vettem észre, hogy ha kirajzolom az adatok és a MC szimulációk (6.1.2 fejezet) kaloriméterkben leadott energiájának az eloszlását azokra az eseményekre, melyekben legalább egy nagy ($8<p_\mathrm{T}<15$ GeV) transzverzális impulzusú töltött részecske van (10.4 ábra), egy csúcs látható 10 GeV környékén. A kaloriméterek szinte a teljes térszöget lefedik és a legmegbízhatóbb elemei a detektornak, az ilyen események nem adhatnak csúcsot 10 GeV környékén. Mivel mind az adatra, mind a jel MC-ra jellemző, ez nem lehet szimulációs hiba sem, az okokat a rekonstrukció szintjén kerestem, amikor a detektor jeléből (függetlenül attól, hogy az mérésből, vagy szimulációból jött) egy algoritus részecskenyomot hoz létre. A háttér MC-k kevésbé voltak érintve, mivel bennük a foton-foton folyamatokhoz képest a nyomokra erősebb minőségi feltételek szerepeltek a szimulációikban.

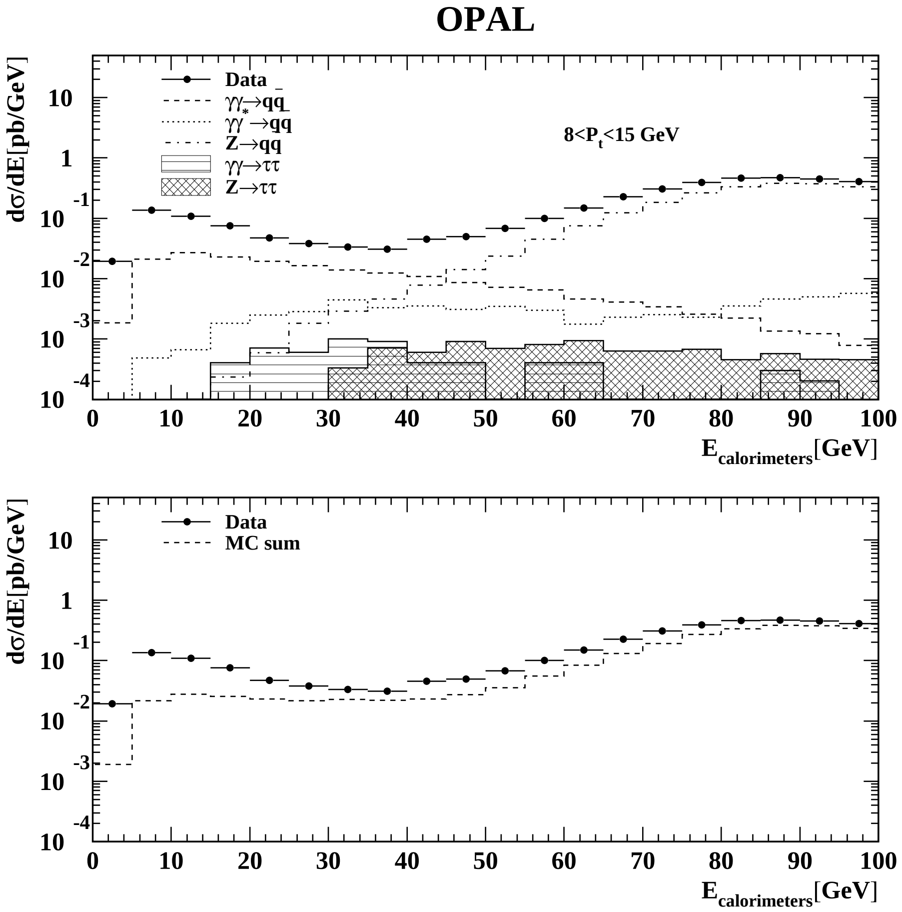

10.4. ábra. Energialealeadás az ECAL és HCAL kaloriméterekben azokra az eseményekre, melyekben a legnagyobb transzverzális impulzus a töltött részecskékre 8 és 15 GeV közt van

A rekonstrukció részletes adatai nem voltak benne a csoport által használt fájlokban, így első lépésként vissza kellett térnem a csoport által elfogadott MC fájlokat gyártó generátorokhoz és azokhoz a szkriptekhez, amik az általunk megkövetelt szerkezetűvé alakították a mérési adatokat. Beállítva a részletes adatok legyártását, újra el kellett készíteni néhány MC és adatfájlt. Ezekben vizsgáltam meg a rekonstrukció folyamatát. A jel MC szimulációban kerestem meg azokat a részecskenyomokat (detektor szint), amihez közel nem találtam részecskét (hadron szint).

Ezek kiszűrésére a $d_0$ (impact parameter, a részecskenyom előjeles távolsága az ütközési ponttól) volt a legmegfelelőbb. A $|d_0|$<0.15 cm vágást alkalmaztam, ezzel a kaloriméterek energiaeloszlása az elvártnak megfelelően vieselkedik (10.5 ábra). Ezzel a vágással a jól rekonstruált részecskék több, mint 90%-át, míg a rosszul rekonstruáltak kevesebb, mint 20%-át tartom meg. Ez azt is jelentette, hogy a kivágott, alaptalanul nagy transzverzális impulzusúnak hitt részecskenyomok miatt a $25<p_T<45$ GeV bin, az adatok alapján először remélt legnagyobb bin kiesett, mert túl kevés valódi részecskenyom maradt ebben a binben.

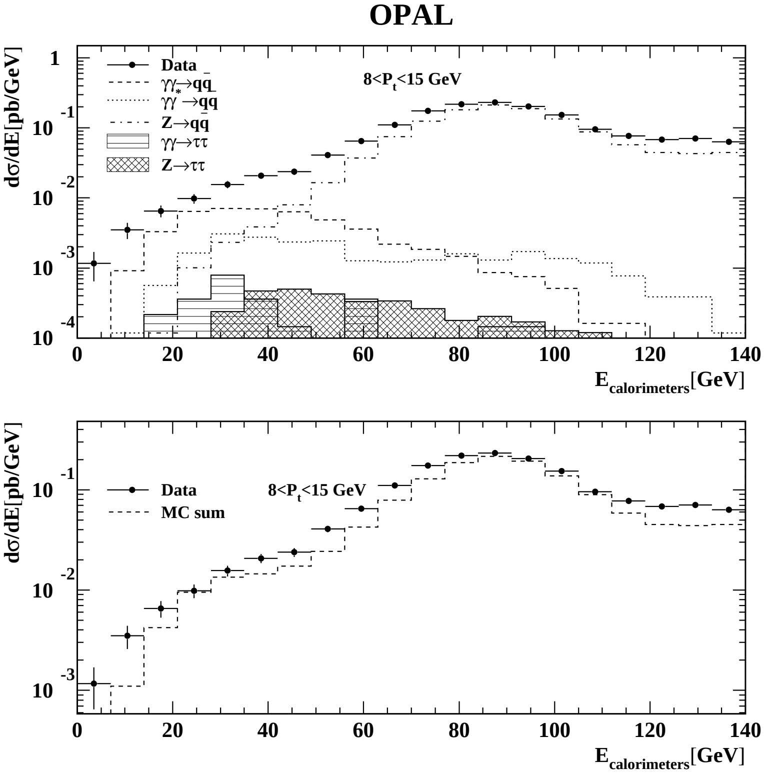

10.5. ábra. Energialealeadás az ECAL és HCAL kaloriméterekben azokra az eseményekre, melyekben a legnagyobb transzverzális impulzus a töltött részecskékre 8 és 15 GeV közt van, használva a $|d_0|$<0.15 cm vágást.

A $d\sigma/dp_T$- és $d\sigma/d|\eta|$-eloszlásokat négy invariáns tömeg intervallumban mértem meg: $10<W<30$ GeV, $30<W<50$ GeV, $50<W<125$ GeV és $10<W<125$ GeV, hasonlóan a megelőző publikációhoz [35].

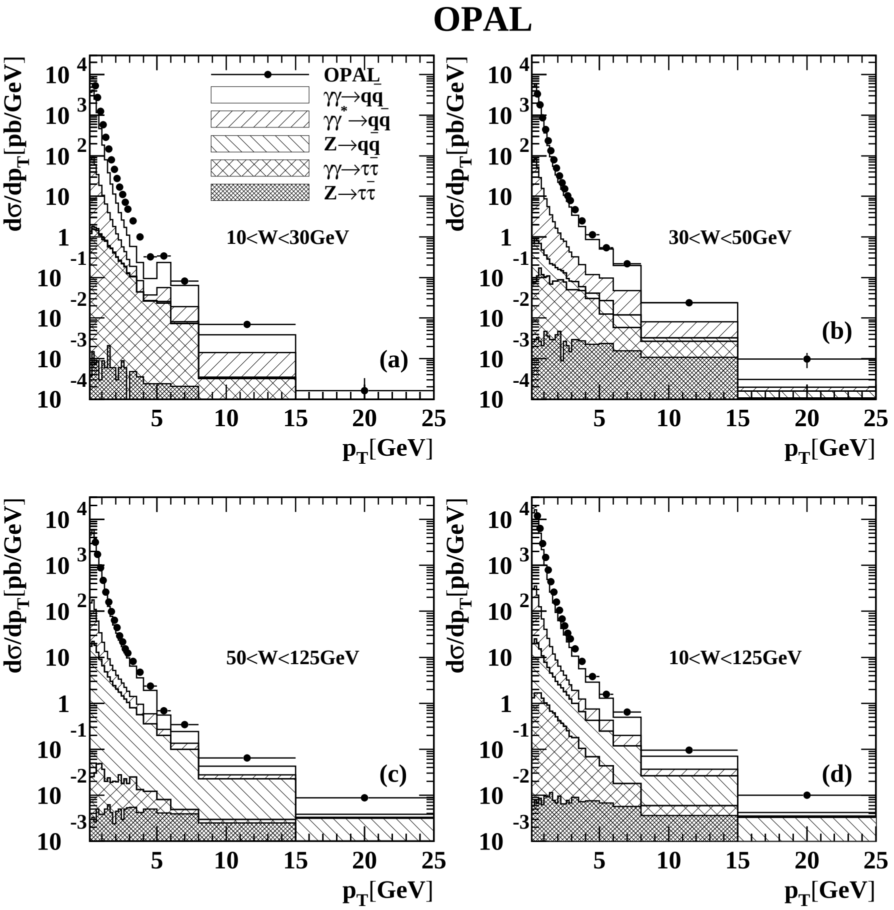

10.6. ábra. Az adat és a MC-k $p_{\mathrm{T}}$ eloszlása

Minden vágás alkalmazása után maradt 1144035 esemény, a fő hátterek pedig a Z hadronikus bomlása, a Z→tau-tau háttér és a mélyen rugalmatlan kétfoton folyamat, amikor az ütközés egyik elektronja detektálásra kerül (ekkor a kvázi-valós foton feltételezés nem igaz, ez nem része a mérésemnek). Az adat és a MC-k $\mathrm{d}\sigma/\mathrm{d}p_{\mathrm{T}}$-eloszlása a 10.6 ábrán látható.

Az értékek, külön feltüntetve a statisztikus és szisztematikus hibákat, a 8.1-8.5 táblázatokban vannak. Az NLO sztintű elméleti számítások eltérnek nagy $p_{\mathrm{T}}$ esetén (10.7 ábra)

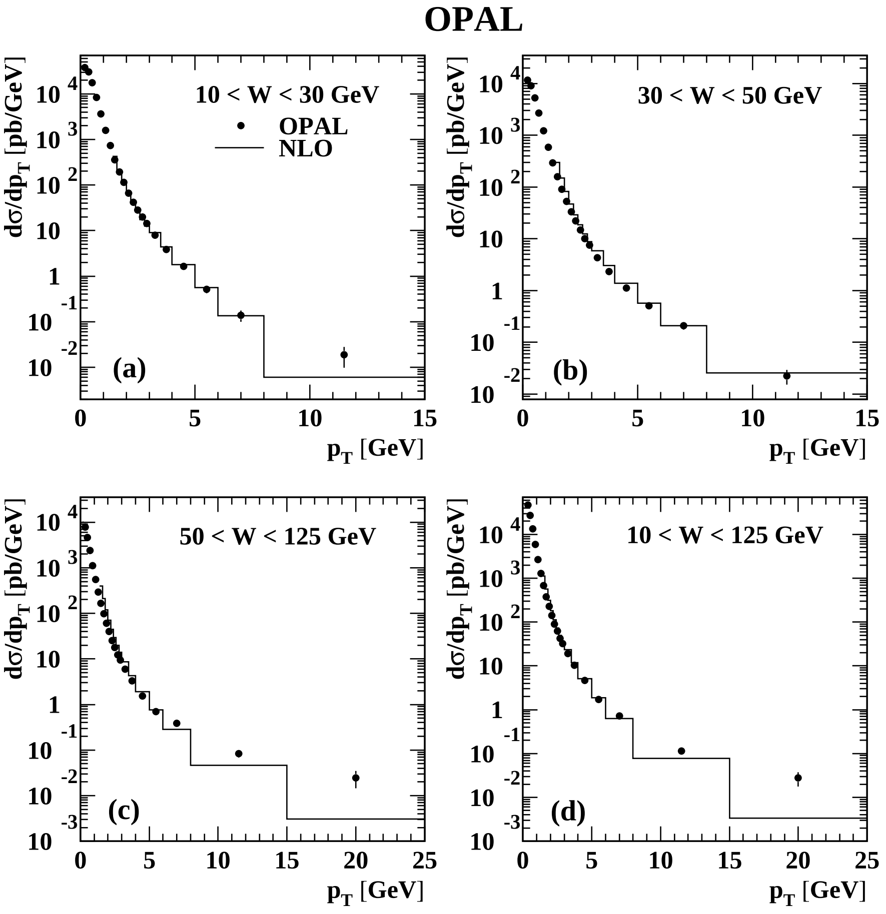

10.7. ábra. A mérés és az NLO számítás összehasonlítása

Az L3 detektor korábban publikált [51] mérése más kinematikai feltételeket használt, ezeket figyelembe véve megmértem a hatáskeresztmetszetet és az elméleti számításokat is ehhez igazítva össze tudtam hasonlítani két detektor és az NLO számítás eredményét (10.8 ábra). A töltött pionok esetén a jel MC-t vettem alapul a pion-hadron arány megállapításakor, mint ahogy az L3 is tette, itt az L3 $|\eta| < 1.0$ feltételét is alkalmaztam.

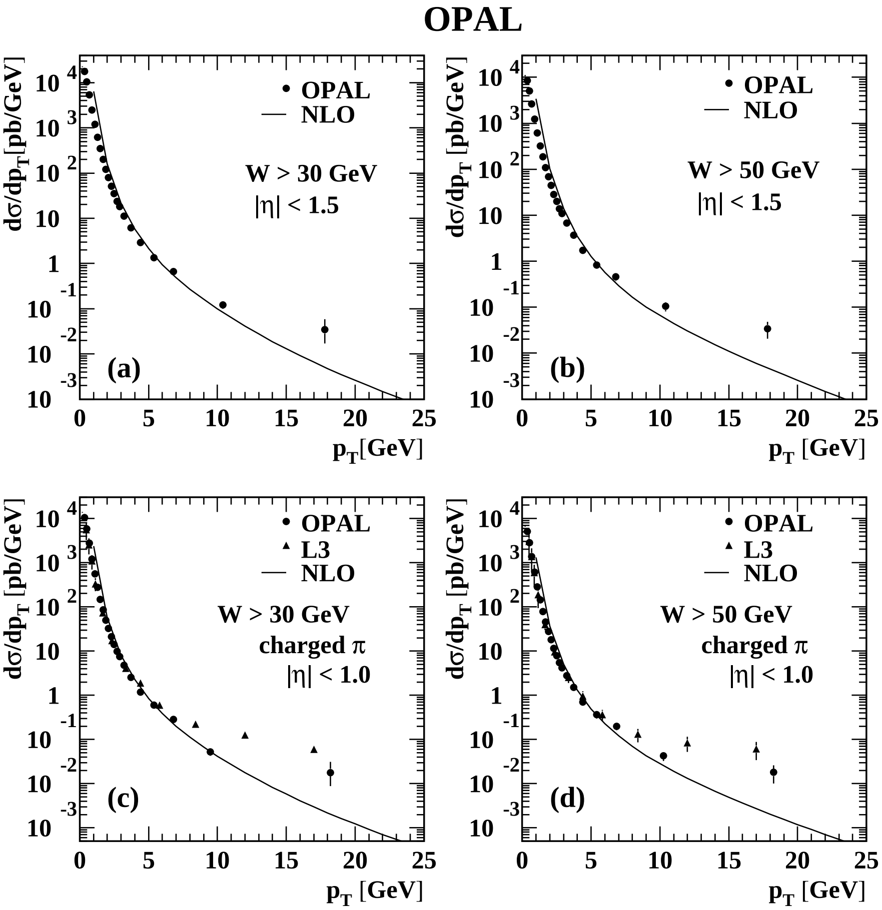

10.8. ábra. Inkluzív töltött hadron hatáskeresztmetszete OPAL-L3 összehasonlítás.

Az eredményeim alapján Thorsten Wengler, aki a csoportunk vezetője is volt, még utánam egyszer beszámolt [58] az OPAL inkluzív és jet méresiről, mely mindkét esetben csak az utolsó binben térnek el az elméleti számításoktól (míg az L3 nagyobb eltérést mutat). Philip Yock az eltérést mindkét detektor esetén szignifikánsnak látta [59], [60] és egy nagyobb töltéssel rendelkező kvarkok lehetőségét veti fel, amit majd csak a jövő gyorsítói tudnak ellenőrizni. Bylinkin és Rostovtsev [61] egy új parametrizációt javasolt.

# Chapter 11

# Acknowledgement

This work made of the patience of Zoltán Trócsányi, Dezső Horváth and József Molnár.
The work is supported by the TÁMOP-4.2.2/B-10/1-2010-0024 project. The project is co-financed by the European Union and the European Social Fund.

*Ceci n'est pas une pipe*
*(René Margritte)*

# Bibliography

[1] Paul Langacker, The Standard Model and Beyond (Series in high energy physics, cosmology, and gravitation), CRC Press, 2010.

[2] J. D. Hobbs, M. S. Neubauer and S. Willenbrock, Tests of the Standard Electroweak Model at the Energy Frontier, arXiv:1003.5733 [hep-ex].

[3] S. L. Glashow,Partial Symmetries of Weak Interactions, Nucl. Phys. **22** (1961) 579.
A. Salam, Renormalizability of gauge theories, Phys. Rev. **127**, 331 (1962).
S. Weinberg,A Model of Leptons, Phys. Rev. Lett. **19**, 1264 (1967).

[4] http://pdg.lbl.gov

[5] G. Altarelli and M. W. Grunewald, Precision electroweak tests of the standard model, Phys. Rept. **403-404** (2004) 189

[6] S. M. Bilenky, CP-violation and unitarity triangle test of the standard model, Phys. Part. Nucl. **39** (2008) 641

[7] CMS Collaboration, Observation of a new boson at a mass of 125 GeV with the CMS experiment at LHC, Physicsy Letters B **716** (2012) 30-

[8] CMS Collaboration, The CMS muon project : Technical Design Report, (1997)

[9] N. E. Adam et al.,Higgs Working Group Summary Report,arXiv:0803.1154 [hep-ph].

[10] CMS Collaboration, CMS physics: Technical design report, (2006)

[11] Szillási Z, Kísérleti eszközök fejlesztése a nagyenergiájú fizika számára. Doktori (PhD) értekezés. Témavezető: Baksay L. és Raics P. Debrecen, Debreceni Egyetem Természettudományi Kar **0** (2007)159-159.

[12] F. Matorras et al. CMS Technical Note TN/94-249 (1994)
F. Matorras et al., CMS Technical Note TN/95-069 (1995)

[13] Samir Guragain, Muon Endcap Alignment for the CMS Experiment and Its Effect on the Search for Z’ Bosons in the Dimuon Channel at LHC, PhD thesis, Melbourne, Florida 2010.

[14] VISION VM5402 Camera Module Dual-standard Monochrome CMOS Image Sensor, Product Datasheet, VLSI VISION LIMITED, 1998.

[15] D. Novak, A. Fenyvesi, J. Molnar, G. Szekely, J. Vegh,N. Beni, A. Kapusi, P. Raics, Zs. Szabo, Z. Szillasi, Gy. L. Bencze, Integration study and first test results of the CMS Muon Barrel Alignment system, Workshop on Electronics for LHC and Future Experiments, Boston, (2004)

[16] G. Szekely, G. Bencze, K. Courtens, J. Molnar, D. Novák, P. Raics, Zs. Szabo, Z. Szillasi, J. Vegh, Muon Barrel Alignment system based on a net of PC/104 board computers,9th Workshop on Electronics for LHC Experiments, CERN-LHCC-2003-055 (2003)

[17] Pedro Arce, Object Oriented Software for Simulation and Reconstruction of big Alignment Systems, Proceedings of the 7th International Workshop on Accelerator Alignment, SPring-8, (2002)

[18] http://root.cern.ch/drupal/

[19] CMS Collaboration, Aligning the CMS Muon Chambers with the Muon Alignment System during an Extended Cosmic Ray Run, JINST 5 (2010) T03019.

[20] CMS Collaboration, Performance of CMS muon reconstruction in pp collision events at sqrt(s) = 7 TeV, , JINST 7 (2012) P10002.

[21] B. Ujvari et al., CMS Collaboration, CMS NOTE-2012/005: CMS Barrel Muon Alignment: Influence of Missing MABs on DT-positioning Accuracy

[22] A. De Roeck, Photon Interactions at High Energies, Surveys in high energy physics, 16:1/2(2001), p. 49-86

[23] M. Przybycień, Habilitation Thesis, Kraków (2003)

[24] R. Nisius, Phys. Rep. **332**, 165 (2000)

[25] H. D. Politzer, Phys. Rev. Lett. **30**, 1346 (1973)

[26] E.Fermi, Z.Physik **29**, (1924) 315.

[27] J. Binnewies, B.A. Kniehl and G. Kramer, Phys. Rev. D **53** (1996) 6110;
B.A. Kniehl, private communications.

[28] S. Albino, B.A. Kniehl, G. Kramer, Nucl. Phys. B **725**, 181 (2005)
S. Albino, B. A. Kniehl, G. Kramer and W. Ochs Phys. Rev. D **73**, 054020 (2006)

[29] P. Aurenche, J.-P. Guillet, M. Fontannaz, Z. Phys. C64 (1994) 621.

[30] R.K. Ellis, W.J. Stirling, B.R. Webber, Nuclear Physics and Cosmology **8**, 2003

[31] OPAL Collaboration, K. Ahmet et al., Nucl. Instrum. Methods A305 (1991) 275;
S. Anderson et al., Nucl. Instrum. Methods A403 (1998) 326;
OPAL Collaboration, G. Abbiendi et al., Eur. Phys. J. C14 (2000) 373.

[32] Jason Ward, A study of Photon Structure with Special Attention to the Low-x Region University College London, England , May 1996, Dissertation

[33] K. Stoll, A SW Energy Correction for Two-Photon Events, OPAL TN474

[34] Jan A. Lauber, Using FD to measure hadronic energy in the forward region, OPAL TN348

[35] The OPAL Collaboration, K. Ackerstaff et al., Eur. Phys. J. C **6** (1999) 253.

[36] J. Allision et al., Nucl. Instr. Meth. A, **317**, 47 (1992)

[37] http://opalinfo.cern.ch/opal/online/runsum/data-summary.html

[38] Physics Analysis Workstation http://paw.web.cern.ch/paw/

[39] CERN Advanced STORage manager http://castor.web.cern.ch/castor/

[40] http://opalinfo.cern.ch/opal/group/twophoton/ggntprod/GGNTUPLE_DOC

[41] CT Processor for ROPE http://opalinfo.cern.ch/opal/manuals/ct/pro/ct.html

[42] MT Users' Guide http://opalinfo.cern.ch/opal/manuals/mt/pro/mt151.html

[43] T. Sjöstrand, Comp. Phys. Commun. **82** (1994) 74.

[44] R. Engel, Z. Phys. C66 (1995) 203;
R. Engel and J. Ranft, Phys. Rev. D **54** (1996) 4244.

[45] G.A. Schuler and T. Sjöstrand, Z. Phys. C **68** (1995) 607.

[46] M. Glück, E. Reya, A. Vogt, Phys. Rev. D **46**, 1973 (1992)

[47] S. Jadach, B.F.L. Ward and Z. Was, Comp. Phys. Commun. **79** (1994) 503.

[48] J.A.M. Vermaseren, Nucl. Phys. B **229** (1983) 347.

[49] G. Marchesini, B.R. Webber, G. Abbiendi, I.G. Knowles, M.H. Seymour and L. Stanco, Comp. Phys. Commun. **67** (1992) 465.

[50] OPAL Collaboration, K. Ackerstaff et al., Eur. Phys. J. C **2** (1998) 213;
OPAL Collaboration, G. Abbiendi et al., Eur. Phys. J. C **12** (2000) 567.

[51] L3 Collaboration, P. Achard et al., Phys. Lett. B **554** (2003) 105.

[52] OPAL Collaboration, G. Abbiendi et al., Eur. Phys. J. C **14** (2000) 199.

[53] OPAL Collaboration, G. Abbiendi et al.,Phys. Lett. B **658**, 185 (2008)

[54] L3 Collaboration, P. Achard et al., Phys. Lett. B **602**, 157 (2004)

[55] P. Aurenche, M. Fontannaz, J.-P. Guillet, Parton distributions in the photon Z. Phys C **64**,621 (1994)

[56] OPAL Collaboration, Inclusive production of charged hadrons in photon-photon collisions. Physics Letters B **651** (2007)92-101.

[57] OPAL Collaboration, Inclusive production of charged hadrons and jets in photon-photon collision at LEP2. Nuclear Physics B Proceedings Supplement **184** (2008)117-121.

[58] T. Wengler, Hadronic photon-photon scattering at LEP,J. Phys. Conf. Ser. **110** (2008) 022056

[59] P. Yock, Anomalous gamma gamma interaction,In the Proceedings of 2007 International Linear Collider Workshop (LCWS07 and ILC07), Hamburg, Germany, 30 May - 3 Jun 2007, pp GG03

[60] P. Yock, The Gamma-Gamma Interaction: A Critical Test of the Standard Model, Int. J. Mod. Phys. A **24** (2009) 3276

[61] A. A. Bylinkin and A. A. Rostovtsev, Systematic studies of hadron production spectra in collider experiments, arXiv:1008.0332 [hep-ph].

[62] DELPHI Collaboration, J. Abdallah et al., Phys. Lett. B **678** (2009) 444